Dear Members of the Faculty Search Committee,

I am writing to apply for the tenure-track position of Assistant Professor in Civil Engineering at Purdue University. I am broadly interested in applying the physics of multiphase flow in porous media and graph neural network to resolve Earth science problems including geological carbon sequestration, hydraulic fracturing, and methane hydrates. I am also interested in the physics of the cryosphere, with a current focus on the hydrology of ice sheets and ice-ocean interactions. I completed my Ph.D. in Civil and Environmental Engineering at the Massachusetts Institute of Technology under the supervision of Dr. Ruben Juanes. I am currently a postdoctoral scholar in Department of Geophysics at Stanford University under the supervision of Dr. Ching-Yao Lai. Prior to graduate school I received an undergraduate degree in Civil and Environmental Engineering from the University of Hong Kong.

My research lies at the intersection of fundamental fluid and solid mechanics, granular physics, geoscience, and more recently machine learning. I strive to bridge pore/grain-scale physics to observations on Earth's surface processes. My PhD research in MIT focused on fluid-induced deformation and fracture of granular media, and uncovering the underpinning grain-scale mechanics via computational (discrete element modeling, DEM), experimental (photoporomechanics), and theoretical (poromechanics) methods. During my PhD I published papers in *Physical Review Research, Physical Review Applied*, and *Soft Matter*. After the completion of my PhD, I decided to use my expertise in mechanics to address key questions in climate change. I have been a postdoctoral scholar with Dr. Ching-Yao Lai at Princeton University and Stanford University. Motivated by recent observations from remote sensing, I have developed models and parameterizations for englacial hydrology and ice mélange buttressing against calving. I have a first-author paper under review and another one in preparation. I will present our findings in my talk "*Thickness of Pro-glacial Mélange Impacts Calving Dynamics of Greenland Glaciers* " at AGU (December 2023).

My research vision focuses on bridging multiphase flow, granular mechanics, and remote sensing of the cryosphere for a sustainable future. Research in my group will combine experiments, analytical and computational modeling, and deep learning to solve large-scale Earth science problems in the areas of energy and the environment, including geological carbon sequestration, ice hydrofracturing and ice-ocean interactions. I will continue to tackle poorly understood climate processes with engineering expertise, such as seasonal variations in mélange buttressing force and its impacts on calving dynamics of tidewater glaciers. I will also investigate how to integrate deep learning with discrete element modeling to simulate complex physics, which sheds light on understanding floating granular materials on Earth, including logjams, sea ice, and volcanic pumice. The advantage of the graph network simulator over discrete element modeling lies in its differentiable nature, which allows for gradient-based optimization and thus solving inverse problems. Applications range from infrastructure design for flood control to particle size/shape design for efficient sediment transport. Lastly, I will build parameterizations of porous media in glaciology. This advances our understanding of how much and how quickly surface meltwater can be transported through the supraglacial and englacial hydrologic systems and how those systems are evolving with time, which is critical for assessing current and future sea level contributions from the Greenland Ice Sheet.

Your department's vibrant engineering and sciences community makes it a particularly compelling home to achieve my research vision and train the next generation of scientists. The department includes a unique mix of experts working on areas such as hydraulic engineering, environmental sustainability, and data-driven approaches. I would be excited to be part of the diverse environment and collaborate with faculty members.

Thank you for your consideration. I look forward to hearing from you.

Sincerely,

Yue (Olivia) Meng

Postdoctoral Scholar, Department of Geophysics, Stanford University

Yue (Olivia) Meng

397 Panama Mall, Mitchell Building   olivmeng@stanford.edu

Stanford, CA 94305   (609) 255-6542

EDUCATION

2022 **Massachusetts Institute of Technology, Boston, Massachusetts**
Ph.D. Civil and Environmental Engineering
Advisor: Ruben Juanes
Thesis: *Photoporomechanics: A New Technique to Explore Grain-scale Mechanisms for Fluid-driven Fractures in Granular Media*

2020 **Massachusetts Institute of Technology, Boston, Massachusetts**
Master of Science in Civil and Environmental Engineering
Advisor: Ruben Juanes
Thesis: *Jamming Transition and Emergence of Fracturing in Wet Granular Media*

2018 **The University of Hong Kong, Hong Kong**
Bachelor of Engineering, Civil and Environmental Engineering
Minor in Engineering in Computer Science
Advisor: Fiona Kwok
Thesis: *Discrete Element Modeling of the Formation of Arch Network in Granular Media During Shearing Process*

PROFESSIONAL EXPERIENCE

2023 – present **Stanford Icy Physics Group, Department of Geophysics, Stanford University**
Postdoctoral Scholar, Advisor: Dr. Ching-Yao Lai
- Coupling remote sensing with physics-based models to quantify the ice mélange buttressing against calving
- Combining discrete element model with graph neural network to simulate complex physics in ice mélange

2022 – 2023 **The Lai Research Group, Department of Geosciences, Princeton University**
Postdoctoral Research Associate, Advisor: Dr. Ching-Yao Lai
- Poromechanical modeling on the vulnerability of firn to hydrofracture in Greenland

2018 – 2022 **Subsurface Energy and Mechanics Lab, Massachusetts Institute of Technology**
PhD Student, Advisor: Dr. Ruben Juanes
- Experimental study on fracturing in wet granular media using photoporomechanics
- Discrete element modeling on multi-phase flow and granular mechanics: wettability control on hydraulic fracturing patterns

2015 – 2018 **Department of Civil and Environmental Engineering, The University of Hong Kong**
Undergraduate Research Assistant, Advisor: Dr. Fiona Kwok
- Experimental investigations on mechanical properties of sand-rubber mixture
- Discrete element modeling of the formation of arch network in granular media during shearing process

AWARDS

2018   Hui Ying Hin Fellowship, University of Hong Kong
2018   Wing Lung Bank Ltd. Prize in Civil Engineering in Hong Kong
2018   Centenary Scholarships for Civil Engineering Students, University of Hong Kong
2017   Gammon Construction Limited Prize in Civil Engineering

2016   Chan Hon Chuen Scholarship, University of Hong Kong

JOURNAL PUBLICATIONS

In Preparation

Meng, Y., Lai, C. Y., Culberg, R., Shahin, M., Stearns, L., Burton, J., & Nissanka K. Thickness of Pro-glacial Mélange Impacts Calving Dynamics of Greenland Glaciers.

Under Review

Meng, Y., Culberg, R., & Lai, C. Y. Vulnerability of Firn to Hydrofracture: Poromechanics Modeling.
https://eartharxiv.org/repository/view/5149/

Peer Reviewed Articles

Meng, Y., Li, W., & Juanes, R. (2023). Crossover from Viscous Fingering to Fracturing in Cohesive Wet Granular Media: A Photoporomechanics Study. *Soft Matter*, (accepted). 10.1039/D3SM00897E

Guével, A., **Meng, Y.**, Peco, C., Juanes, R., & Dolbow, J. E. (2023). A Darcy-Cahn-Hilliard Model of Multiphase Fluid-driven Fracture. *Journal of the Mechanics and Physics of Solids*, (accepted). 10.1016/j.jmps.2023.105427

Meng, Y., Li, W., & Juanes, R. (2022). Fracturing in Wet Granular Media Illuminated by Photoporomechanics. *Physical Review Applied, 18*(6),064081. * *Editor's Suggestion*. 10.1103/PhysRevApplied.18.064081

Li, W., **Meng, Y.**, Primkulov, B. K., & Juanes, R. (2021). Photoporomechanics: An Experimental Method to Visualize the Effective Stress Field in Fluid-filled Granular Media. *Physical Review Applied*, *16*(2), 024043. 10.1103/PhysRevApplied.16.024043

Meng, Y., Primkulov, B. K., Yang, Z., Kwok, C. Y., & Juanes, R. (2020). Jamming Transition and Emergence of Fracturing in Wet Granular Media. *Physical Review Research*, *2*(2), 022012. 10.1103/PhysRevResearch.2.022012

Juanes, R., **Meng, Y.**, & Primkulov, B. K. (2020). Multiphase Flow and Granular Mechanics. *Physical Review Fluids*, *5*(11), 110516. 10.1103/PhysRevFluids.5.110516

Meng, Y., Zhu, H., Kwok, C. Y., Kuo, M., Jing, L., & Huang, X. (2018). Effect of Coefficient of Friction on Arch Network in Shearing Process under Low Confinement. *Powder technology*, *335*, 1-10. 10.1016/j.powtec.2018.05.002

INVITED TALKS

2023   *"Photoporomechanics: A new technique to explore grain-scale mechanisms for fluid-driven fractures in granular media"*, Department of Civil Engineering, McMaster University, Canada.
2023   *"Photoporomechanics: A new technique to explore grain-scale mechanisms for fluid-driven fractures in granular media"*, American Rock Mechanics Association Future Leader Webinar Series.
2022   *"Fracturing in wet granular media illuminated by photoporomechanics"*, Solid Earth Brown Bag, Department of Geosciences, Princeton University.

2021   *"Jamming transition and emergence of fracturing in wet granular media",* Earth Resources Laboratory Annual Founding Members Meeting, Massachusetts Institute of Technology.

2019   *"DEM modeling of coupled multiphase flow and granular mechanics: Wettability control on fracture patterns",* Society of Petrophysicists and Well Log Analysts Meeting.

2019   *"DEM modeling of coupled multiphase flow and granular mechanics: Wettability control on fracture patterns",* Earth Resources Laboratory Annual Founding Members Meeting, Massachusetts Institute of Technology.

MENTORING EXPERIENCE

Fall   2023   Judy Liu (Undergraduate Student in Dr. Ching-Yao Lai Group, Stanford University)
Spring 2023   Hugh Shields (Undergraduate Student in Dr. Ching-Yao Lai Group, Princeton University)
2022 – 2023   David Dai & Feihu Ke (PhD Students in Dr. Fiona Kwok Group, University of Hong Kong)

PROFESSIONAL ACTIVITIES

2018 – present Member, American Physical Society
2018 – present Member, American Geophysical Union

Reviewer: International Journal for Numerical and Analytical Methods in Geomechanics, SPE Journal

CONFERENCE PARTICIPATIONS

Meng, Y., Lai, C. Y., Culberg, R., Shahin, M., Stearns, L., Burton, J., & Nissanka K, Thickness of Proglacial Mélange Impacts Calving Dynamics of Greenland Glaciers, *AGU Fall Meeting*, 2023.

Nissanka, K., Burton, J. C., Amundson, J. M., Robel, A., Lai, C. Y., & **Meng, Y.**, Experimental-informed Ice Mélange Rheology and Buttressing During Quasistatic Flow, *AGU Fall Meeting*, 2023.

Meng, Y., Culberg, R., Shahin, M., Stearns, L., Burton, J., Nissanka K, & Lai, C. Y., Thickness of Proglacial Mélange Impacts Calving Dynamics of Greenland Glaciers, *APS DFD Meeting*, 2023.

Meng, Y., Culberg, R., & Lai, C. Y., Vulnerability of Firn to Hydrofracture, Part I: Poromechanical Modeling, *EGU General Assembly*, 2023.

Culberg, R., **Meng, Y.**, & Lai, C. Y., Vulnerability of Firn to Hydrofracture, Part II: Greenland's Ice Slab Regions, *EGU General Assembly*, 2023.

Meng, Y., Culberg, R., & Lai, C. Y., Vulnerability of Firn to Hydrofracture, Part I: Poromechanical Modeling, *Future of Greenland Ice Sheet Science Workshop*, 2023.

Culberg, R., **Meng, Y.**, & Lai, C. Y., Vulnerability of Firn to Hydrofracture, Part II: Greenland's Ice Slab Regions, *Future of Greenland Ice Sheet Science Workshop*, 2023.

Meng, Y., Li, W., & Juanes, R., Photo-poroelastic Imaging of Fracturing in Wet Granular Media, *AGU Fall Meeting*, 2021.

Li, W., **Meng, Y.**, Primkulov, B. K., & Juanes, R., Photo-poromechanics: Visualizing the Evolving Effective Stress in Fluid-filled Granular Media, *AGU Fall Meeting*, 2021.

Meng, Y., Primkulov, B. K., Yang, Z., Kwok, C. Y., & Juanes, R., DEM Modeling of Coupled Multiphase

Flow and Granular Mechanics: Wettability Control on Fracture Patterns, *Engineering Mechanics Institute Conference*, 2019.

Meng, Y., Primkulov, B. K., Yang, Z., Kwok, C. Y., & Juanes, R., DEM Modeling of Coupled Multiphase Flow and Granular Mechanics: Wettability Control on Fracture Patterns, *AGU Fall Meeting*, 2019.

Meng, Y., Primkulov, B. K., Yang, Z., Kwok, C. Y., & Juanes, R., DEM Modeling of Coupled Multiphase Flow and Granular Mechanics: Wettability Control on Fracture Patterns, *APS DFD Meeting*, 2019.

Meng, Y., Primkulov, B. K., Yang, Z., Kwok, C. Y., & Juanes, R., DEM Modeling of Coupled Multiphase Flow and Granular Mechanics: Wettability Control on Fracture Patterns, *Transport in Disordered Environments Seminars*, Princeton Center for Theoretical Science, 2019.

Meng, Y., Primkulov, B. K., Yang, Z., Kwok, C. Y., & Juanes, R., DEM Modeling of Coupled Multiphase Flow and Granular Mechanics: Wettability Control on Fracture Patterns, *AGU Fall Meeting*, 2018.

I am broadly interested in applying the physics of multiphase flow in porous media to resolve Earth science problems including geological carbon sequestration, hydraulic fracturing, and methane hydrates. I am also interested in the physics of the cryosphere, with a current focus on the hydrology of ice sheets and ice-ocean interactions. Through interdisciplinary lens of porous media flows, granular mechanics, deep learning, and geoscience, I strive to bridge pore/grain-scale physics to observations on Earth's surface processes.
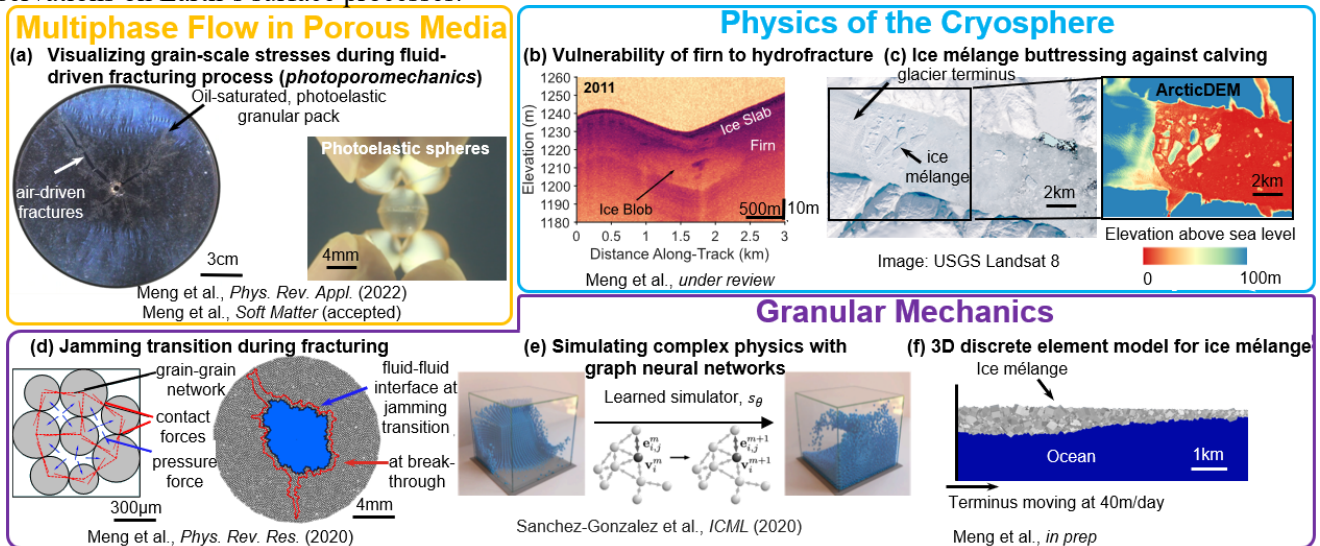

Figure 1: My vision for bridging multiphase flow, granular mechanics, and remote sensing of the cryosphere for a sustainable future. Research in my group will combine experiments, analytical and computational modeling, and deep learning to solve large-scale Earth science problems in the areas of energy and the environment, including geological carbon sequestration, ice hydrofracturing and ice-ocean interactions.

1. Previous Research

1.1 Hydraulic fracturing and gas migration in sediments (experiment/analytical/numerical modeling) Multiphase flow through granular and porous materials exhibits complex behavior, the understanding of which is critical in many industrial and natural processes, including energy recovery, gas venting, and geohazards. While fracturing during gas invasion in fluid-saturated media has been studied extensively, the underlying grain-scale mechanisms behind the morphodynamics and rheologies exhibited by deformable granular media remain poorly understood. My PhD research focused on fluid-induced deformation and fracture of granular media, and uncovering the underpinning grain-scale mechanics. By means of discrete element modeling (DEM), the grain-scale stress analysis unraveled that a jamming transition from fluid-like to solid-like behavior, dictated the morphological transition from cavity expansion to fracturing in wet granular media [1, 2] (Fig.1(d)). To experimentally visualize the evolving intergranular stresses, an innovative experimental technique, photoporomechanics (Fig.1(a)), was developed, which extended photoelasticity to granular-fluid systems [3]. When air was injected into oil-saturated granular pack, there was an effective stress shadow behind the propagating fracture tips, where the intergranular stress was low. In the annular region outside the fractured region, the granular medium went through a jamming transition. The observed distinct rheology was analyzed by poromechanical continuum models for granular media [4, 5], and a phase-field model [6].

1.2 Vulnerability of Greenland's firn layer to hydrofracture (observation/analytical modeling) On the Greenland Ice Sheet, hydrofracture connects the supraglacial and subglacial hydrologic systems, coupling surface runoff dynamics and ice velocity. Over the last two decades, the growth of low-permeability ice slabs in the firn above the equilibrium line has expanded Greenland's runoff zone, but the vulnerability of these regions to hydrofracture is still poorly understood. Observations from Northwest Greenland suggest that when meltwater drains through crevasses in ice slabs, it is stored in the underlying relict firn layer and does not reach the ice sheet bed (Fig.1(b)). However, the mechanism limiting ice slab hydrofracture is not well understood and current fracture mechanics approaches in glaciology are poorly suited to studying this problem, because they assume that ice is an impermeable solid medium. To resolve this gap, I built a two-dimensional poroelastic continuum model to study the vulnerability of firn to hydrofracture [7]. The model was applied to Greenland's ice slab regions, using an ensemble of in situ and remote sensing observations to constrain the physical, mechanical, and hydraulic parameters. The results show that the maximum stress in the firn layer typically remains compressive, because more than 75% of the imposed load is accommodated by a change in pore pressure. Therefore, in Greenland, the relict firn layer can be an important stabilizing factor that suppresses surface-to-bed hydrofracture under ice slabs, despite the abundance of both surface crevassing and meltwater.

2. Current Research Thickness of pro-glacial mélange impacts calving dynamics of Greenland glaciers

(observation/analytical/numerical modeling) Iceberg calving is a major contributor to Greenland's ice mass loss. Proglacial ice mélange is a collection of sea ice and icebergs that is tightly packed in tidewater glacier fjords and can suppress calving by providing resisting stresses called buttressing (Fig.1(c)). Previous observations highlight seasonal change of some Greenland glacier termini, which advance quasi-statically in winter, and retreat by calving in summer. Finite-element models have indicated that the seasonal calving dynamics are related to buttressing from ice mélange. To quantify the mélange buttressing force on the glacier terminus, I developed a continuum theory and a three-dimensional discrete element model that reveals the scaling between the buttressing force and the mélange thickness (Fig.1(f)). The results show that to provide effective buttressing, the average mélange thickness at the terminus must be larger than 145 meters. The thickness threshold has been validated by remote sensing data, including ICESat-2 and a terrestrial laser scanner. After scanning through ArcticDEM data in the past ten years across 40 Greenland glacier termini, it is found that in summer, most mélanges are too thin to suppress calving activities [8].

3. Future Research

3.1 Bridging pore/grain-scale physics to observations on Earth's surface processes Earth's surface is composed of a diversity of particulate-fluid mixtures. Pore or grain-scale physics helps to illuminate geophysical processes like landslides, gas venting from lake sediments, injection-induced seismicity, carbon sequestration and geophysical flows that shape landscapes. However, to model the multi-dynamics of the ground, one key challenge is to link the pore/grain-scale physics to field-scale observations. My expertise in visualizing grain-scale processes, discrete element modeling, poromechanics, and remote sensing can be well combined to tackle the multiscale challenge. For instance, for hydraulic fractures and gas venting processes, it would be important to further advance the understanding of how the force chain evolution observed by photoporomechanics or discrete element model is modulated by the medium rigidity, compressibility and hydraulic diffusivity. With these pore and grain-scale physics insights, my group will advance continuum models to better explain the continental-scale gas migration, trapping and venting dynamics. Another long-term goal is to advance parameterizations of porous media in glaciology. Topics that intrigue me include firn/snow percolation and compaction processes, weathering crust dynamics, ice sliding over till, and temperate ice.

3.2 Advancing physics-based models for ice-ocean interactions to better understanding calving dynamics Dynamics of tidewater glaciers are of high interest because of their potential for drawing down large areas of the Greenland ice sheet through calving. In a warming climate, calving dynamics are sensitive to external forcing, including ice-ocean interactions. My previous work indicates that mélange thickness dictates its buttressing force against calving, but it remains unknown what factors shape the mélange thickness profile. The discrete element model can be coupled with oceanography to further explore how the mélange thickness profile evolves with ice-ocean interactions, including ocean tides, ocean warming, and subglacial plume. My long-term goal is to parameterise seasonal mélange back stress across Greenland glacier termini, which can then be properly incorporated into ice-sheet models.

3.3 Tackling multiscale challenges in granular mechanics with graph neural networks (GNN) Recently, a class of learned physics simulators based on graph neural networks has been proposed, involving fluids, rigid solids, and deformable materials interacting with one another [9]. The graph network represents the state of a physical system with particles, expressed as nodes in a graph, and computes dynamics via learned message-passing (Fig.1(e)). Currently, I am leading a GNN project collaborating with DeepMind to study the physics of ice mélange. The advantage of the graph network simulator over discrete element modeling lies in its differentiable nature, which allows for gradient-based optimization and thus solving inverse problems [10]. Applications range from infrastructure design for flood control to particle size/shape design for efficient sediment transport. With the capability of parallel computing, GNN also serves as a promising tool to tackle multiscale challenges in granular mechanics. In the future, I plan to combine discrete element model and GNN to explore behaviors of granular materials on Earth, such as logjams and volcanic pumice. There are other land surface processes that benefit from grain-scale modeling, such as marine ice-cliff instabilities, geological fault slips, and break-up of sea ice.

4. Potential Funding

References

[1] Meng, Y., Primkulov, B. K., Yang, Z., Kwok, C. Y., & Juanes, R. (2020). Jamming transition and emergence of fracturing in wet granular media. *Physical Review Research*, *2*(2), 022012. 10.1103/PhysRevResearch.2.022012

[2] Juanes, R., Meng, Y., & Primkulov, B. K. (2020). Multiphase flow and granular mechanics. *Physical Review Fluids*, *5*(11), 110516. 10.1103/PhysRevFluids.5.110516

[3] Li, W., Meng, Y., Primkulov, B. K., & Juanes, R. (2021). Photoporomechanics: An experimental method to visualize the effective stress field in fluid-filled granular media. *Physical Review Applied*, *16*(2), 024043. 10.1103/PhysRevApplied.16.024043

[4] Meng, Y., Li, W., & Juanes, R. (2022). Fracturing in wet granular media illuminated by photoporomechanics. *Physical Review Applied, 18*(6),064081. *Editor's Suggestion.* 10.1103/PhysRevApplied.18.064081

[5] Meng, Y., Li, W., & Juanes, R. (2023). Crossover from viscous fingering to fracturing in cohesive wet granular media: A photoporomechanics study. *Soft Matter,* (accepted). 10.1039/D3SM00897E

[6] Guével, A., Meng, Y., Peco, C., Juanes, R., & Dolbow, J. E. (2023). A Darcy-Cahn-Hilliard model of multiphase fluid-driven fracture. *Journal of the Mechanics and Physics of Solids,* (accepted). https://arxiv.org/pdf/2306.16930.pdf

[7] Meng, Y., Culberg, R., & Lai, C. Y. Vulnerability of firn to hydrofracture: poromechanics modeling. https://eartharxiv.org/repository/view/5149/

[8] Meng, Y., Lai, C. Y., Culberg, R., Shahin, M., Stearns, L., Burton, J., & Nissanka K. Thickness of pro-glacial mélange impacts calving dynamics of Greenland glaciers, *In prep*.

[9] Sanchez-Gonzalez, A., Godwin, J., Pfaff, T., Ying, R., Leskovec, J., & Battaglia, P. (2020, November). Learning to simulate complex physics with graph networks. In *International conference on machine learning* (pp. 8459-8468). PMLR. http://proceedings.mlr.press/v119/sanchez-gonzalez20a/sanchez-gonzalez20a.pdf

[10] Allen, K. R., Lopez-Guevara, T., Stachenfeld, K., Sanchez-Gonzalez, A., Battaglia, P., Hamrick, J., & Pfaff, T. (2022). Physical design using differentiable learned simulators. https://arxiv.org/abs/2202.00728

Professional References for Yue (Olivia) Meng

Dr. Ruben Juanes

Professor, Department of Civil and Environmental Engineering, Massachusetts Institute of Technology

Email: juanes@mit.edu

Phone: (617) 253-7191

Mailing Address: 77 Massachusetts Avenue, Building 1-363, Cambridge, MA, 02139, USA

Dr. Ching-Yao Lai

Assistant Professor, Department of Geophysics, Stanford University

Email: cyaolai@stanford.edu

Phone: (609) 937-6329

Mailing Address: 397 Panama Mall, Stanford University, Stanford, CA, 94305, USA

Dr. Riley Culberg

Assistant Professor, Department of Earth and Atmospheric Sciences, Cornell University

Email: rtculberg@cornell.edu

Phone: (253) 254-4857

Mailing Address: 4142 Snee Hall, Cornell University, Ithaca, NY, 14850, USA

Dr. Justin Burton

Associate Professor, Department of Physics, Emory University

Email: justin.c.burton@emory.edu

Phone: (404) 727-4297

Mailing Address: N201 Math & Science Center, 400 Dowman Drive, Atlanta, GA, 30322

Dr. Leigh A Stearns

Professor, Department of Geology, University of Kansas

Email: stearns@ku.edu

Phone: (785) 864-4202

Mailing Address: Ritchie Hall, University of Kansas, Lawrence, KS, 66045

Fracturing in Wet Granular Media Illuminated by Photoporomechanics

Yue Meng⬤, Wei Li⬤, and Ruben Juanes⬤*

Massachusetts Institute of Technology, 77 Massachusetts Avenue, Cambridge, Massachusetts 02139, USA

We study fluid-induced deformation and fracture of granular media and apply photoporomechanics to uncover the underpinning grain-scale mechanics. We fabricate spherical photoelastic particles of 2-mm diameter to form a monolayer granular pack in a circular Hele-Shaw cell that is initially filled with a viscous fluid. The key distinct feature of our system is that, with spherical particles, the granular pack has a connected pore space, thus allowing for pore-pressure diffusion and the study of effective stress in coupled poromechanical processes. We inject air into the fluid-filled photoelastic granular pack, varying the initial packing density and confining weight. With our recently developed experimental technique, photoporomechanics, we find two different modes of fluid invasion: fracturing in fluid-filled elastic media (with strong photoelastic response) and viscous fingering in frictional fluids (with weak or negligible photoelastic response). We directly visualize the evolving effective stress field and discover an effective stress shadow behind the propagating fracture tips, where the granular pack exhibits undrained behavior. We conceptualize the behavior of the system by means of a mechanistic model for a wedge of the granular pack bounded by two growing fractures. The model captures the pore-pressure build-up inside the stress shadow region and the grain compaction in the annular region outside. Our model reveals that a jamming transition determines the distinct rheological behavior of the wet granular pack, from a friction-dominated to an elasticity-dominated response.

I. INTRODUCTION

Multiphase flow through granular and porous materials exhibits complex behavior, the understanding of which is critical in many natural and industrial processes. Examples include infiltration of water into the vadose zone [1], growth and deformation of cells and tissues [2], and geological carbon dioxide storage [3]. While fluid-fluid displacement in rigid porous media has been studied in depth, the understanding of the interplay between multiphase flow and granular mechanics remains an ongoing challenge [4]. In many granular-fluid systems, the powerful coupling among viscous, capillary, and frictional forces leads to a wide range of patterns, including desiccation cracks [5,6], fractures [7–13], labyrinth structures [14], granular fingers [15–17], corals, and stick-slip bubbles [18]. An in-depth study of poromechanics behind these coupled solid-fluid processes is crucial to understanding a wide range of phenomena, including methane migration in lake sediments [19], shale-gas production [20], and hillslope infiltration and erosion after forest fires [21].

While fracturing during gas invasion in fluid-saturated media has been studied extensively in experiments [7,8, 10–13,16,22] and simulations [9,17,23–29], the underlying grain-scale mechanisms behind the morphodynamics and rheologies exhibited by deformable granular media remain poorly understood. To investigate the interplay between fluid and solid mechanics of granular media, we adopt a recently developed experimental technique, *photoporomechanics* [30], to directly visualize the evolving effective stress field in a fluid-filled granular medium during the fracturing process. The key idea behind our photoporomechanics technique is the manufacturing of residual-stress-free photoelastic particles (such as spheres or icosahedra) that allow for connectivity of the pore space, so that pore pressure can diffuse and one fluid can displace another even without grain motion. In an earlier study of root growth in photoelastic granular media, Barés *et al.* [31] have manufactured cylindrical photoelastic particles with a groove on the edge to allow for roots to grow between adjacent grains and propagate deep inside the granular medium. This disk-with-groove geometry, however, would likely experience strong adhesion or friction with the walls of the Hele-Shaw cell and it is a less realistic representation of granular materials than spherical particles. Given the importance of frictional forces on the morphological regimes of the granular pack [18,22], here we focus on the impact of confining weight on the fracture patterns. We also adopt packing density as a control variable, which proves to be key to rheological and morphological transitions in granular-fluid systems [18,28].

In this study, we uncover two modes of air invasion under different initial packing densities and confining weights: fracturing in fluid-filled elastic media and viscous fingering in frictional fluids. We discover an effective stress shadow behind the propagating fracture tips, where the intergranular stress is low and the granular pack exhibits undrained behavior. In the annular region outside the fractured region, the mechanical response of the granular medium transitions from friction dominated to elasticity dominated. To explain the observed distinct rheological behavior, we propose a mechanistic model for a wedge between two fractures. Finally, we rationalize the emergence of fracturing across our experiments as a jamming transition.

II. MATERIALS AND METHODS

Following the fabrication process in Ref. [30], we produce photoelastic spherical particles with a diameter $d = 2$ mm (with 3.5% standard deviation) and a volumetric modulus $K_p = 1.6$ MPa. We inject air into a monolayer of photoelastic particles saturated with silicone oil ($\eta = 9.71$ Pa s) in a circular Hele-Shaw cell [Fig. 1]. When particles are immersed in silicone oil, the friction coefficient between particles is $\mu_p = 0.2 \pm 0.06$ and the friction coefficient between the particle and the glass plate is $\mu_w = 0.05 \pm 0.02$. To observe the photoelastic response of the particles, we construct a dark-field circular polariscope by means of a white-light panel together with left and right circular polarizers [32]. Vertical confinement is supplied by a weight, W, adding up the weights from a confining weight, a light panel, a polarizer, and a glass disk that rests on top of the particles. The free top plate with a prescribed confining weight is a natural representation of the conditions that prevail in subsurface processes, where the vertical confining stress is constant and controlled by the depth of the geologic stratum. To allow the fluids (but not the particles) to leave the cell, the disk is made slightly smaller than the interior of the cell (inner diameter $L = 21.2$ cm), resulting in a thin gap around the edge of the cell. A coaxial needle is inserted at the center of the granular pack for saturation, fluid injection, and pore-pressure measurement. We conduct experiments in which we fix the air injection rate ($q = 100$ ml/min) and the syringe reservoir volume ($V_0 = 15$ ml). We use three linear variable differential transformers (LVDTs) to monitor the vertical displacement of the top plate. We adopt a dual-camera system to record bright-field (camera A) and dark-field (camera B) videos. For the sample preparation, the initial packing density (ϕ_0) of the granular pack is controlled by the total mass of particles (M_s) and is calculated in two dimensions through image analysis. Before the air injection, we take a bright-field photo of the granular pack and create a binary mask with an intensity threshold. We then calculate the initial two-dimensional (2D) packing density

(ϕ_0) by dividing the number of particle pixels by the total number of pixels in the circular Hele-Shaw cell. To study the impact of packing density and frictional force, we vary ϕ_0 from 0.78 to 0.84 ($M_s = 37$ to 40 g) and the confining weight W from 25 N to 85 N. The influence of the confining weight (W) on ϕ_0 is negligible ($< 0.2\%$).

To gain additional insight into the rheological behavior of the granular pack, we record the spatiotemporal evolution of the packing density and effective stress fields from the experiments. To construct the 2D packing density field, we create a binary mask, then detect particle positions by centroid finding in MATLAB and compute the packing density at each particle position within a sampling radius $3d$ [33] by dividing the number of particle pixels by the total number of pixels within the sampling circle. We then construct the packing density field for all the particles in the granular pack. To construct the effective stress field, we retrieve the light intensity of the blue channel from dark-field images and convert it into the effective stress value. To obtain the conversion factor between light intensity and effective stress, we conduct a single-bead calibration that directly relates light intensity to interparticle force F [30]. By computing the Cauchy stress tensor for the calibrated particle under the diametrical loading condition, we obtain the expression that relates the interparticle force to the effective stress, $\sigma' = 6F/\pi d^2$ [34]. After this conversion, we visualize the time evolution of the effective stress field from the dark-field images.

III. RESULTS AND DISCUSSION

In Fig. 2, we show the invasion patterns resulting from air injection for experimental conditions with the same confining weight ($W = 25$ N) and two different initial packing fractions ($\phi_0 = 0.84, 0.78$). The invasion patterns at breakthrough—when the invading fluid first reaches the outer boundary—indicate two invasion regimes: (I) fracturing in fluid-filled elastic media, with strong photoelastic response [Fig. 2(a)], and (II) viscous fingering in frictional fluids, with weak or negligible photoelastic response [Fig. 2(b)]. A light intensity $I = 0.65$ in the blue channel of the dark-field images is adopted here as the threshold to differentiate between the two regimes. We analyze the time evolution of the air-oil interface morphology from bright-field images and the rheological behavior of the granular pack from dark-field images (see the videos in the Supplemental Material [35], corresponding to the conditions in Fig. 2 and see Appendix A for the complete visual phase diagram for a range of values of ϕ_0 and W). We compute the ratio between the viscous and capillary forces in the experiments as the modified capillary number $\text{Ca}^* = \eta q R/(\gamma h d^2)$ [22], where the oil viscosity $\eta = 9.71$ Pa s, the injection rate $q = 100$ ml/min, the cell radius $R = 10.6$ cm, the interfacial tension $\gamma = 0.034$ N/m, the cell height $h = 2$ mm, and the particle diameter $d = 2$ mm,
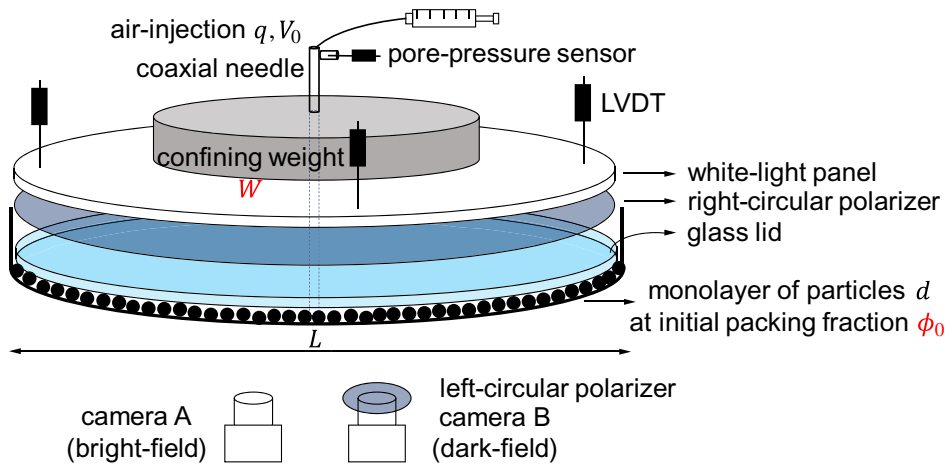
FIG. 1. The experimental setup: a monolayer of photoelastic particles (diameter d, initial packing density ϕ_0) saturated by silicone oil is confined in a circular Hele-Shaw cell (internal diameter L). Vertical confinement is supplied by a weight, W, adding up the weights from a confining weight, a light panel, a polarizer, and a glass disk that rest on top of the particles. The disk is slightly smaller than the cell to allow the fluids (but not particles) to leave the cell. Air is injected at a fixed flow rate q at the center of the cell with a coaxial needle, with the injection pressure monitored by a pore-pressure sensor. Three LVDTs are attached to the top of the light panel, capturing the vertical displacement of the top plate during the fracturing process. A white-light panel and right- and left-circular polarizers form a dark-field circular polariscope. Bright-field and dark-field videos are captured by cameras placed underneath the cell.

resulting in $Ca^* = 6.3 \times 10^3$. Therefore, the effect of capillarity is negligible and viscous effects are dominant in our experiments.

Regime I: Fracturing in fluid-filled elastic media. When particles have been densely packed initially, air initially invades into the granular pack by expanding a small cavity at the injection port, with the injection pressure P_{inj} ramping up during this period [Figs. 3(a) and 3(d) for $\phi_0 = 0.84$]. The onset of fracturing in our cohesionless granular packs is determined by the viscous force from injection overcoming the frictional resistance between particles in the granular pack. Before fracturing, the injection pressure increases and this pressure increase leads to an increased viscous force and, simultaneously, a decreased interparticle frictional force from the lifting of the top plate—a combination that results in the emergence and growth of fractures. A higher W results in a higher peak pressure [Fig. 3(a)] and thus the fracture network becomes more vigorous, with well-developed branches (see Appendix A). In this regime, the effective stress field exhibits a surprising phenomenon: behind the propagating fracture tips, an *effective stress shadow*, where the intergranular stress is low and the granular pack exhibits undrained behavior, emerges and evolves as fractures propagate [Fig. 2(a), right].

Regime II: Viscous fingering in frictional fluids. For granular packs with lower initial packing density ($\phi_0 = 0.78$), the rheology of the system is akin to a frictional fluid [18,28], as evidenced by the weak or negligible photoelastic response at breakthrough [Fig. 2(b), right]. The high-viscosity defending fluid inhibits the injected air from

infiltrating into pore spaces [16]. The fluid-filled granular medium effectively behaves like a suspension [36], the morphology of which is dominated by the Saffman-Taylor instability [18,37,38].

The temporal evolution of the injection pressure and the vertical displacement of the top plate encode the information to help understand the interplay between particle movement and fluid-fluid displacement. At a high injection rate, the dynamics are dominated by the viscous response to the flow in the cell [22]. For all the confining weights, the injection pressure exhibits a peak followed by a decay and a sharp drop corresponding to breakthrough of air at the cell boundary [Fig. 3(a)]. There are three ways to accommodate the injected air volume: compressing particles, driving defending fluid out of the cell, and lifting the confining weight to create extra vertical room. This last mechanism is favored under our experimental conditions, with injection pressure values of approximately 30 kPa. As shown in Fig. 3(b), where we plot the temporal evolution of the vertical displacement δh of the top plate (normalized by the grain size d), the top plate is indeed lifted noticeably during fracturing: $\delta h/d = 5\%$, 6%, and 8% under $W = 25$ N, 65 N, and 85 N, respectively. For the fracturing experiments at $\phi_0 = 0.84$, the initial cell height (h_0) is $0.98d$, $0.96d$, and $0.95d$ under $W = 25$ N, 65 N, and 85 N, respectively (for detailed calculations, see Appendix B). As W increases, a higher injection pressure is reached before the top plate is lifted [Fig. 3(a)], which stores a larger amount of air for fracturing. The invasion morphology at breakthrough [Fig. 7 in Appendix A] shows that, for larger W, a larger volume of air is injected into the cell by either
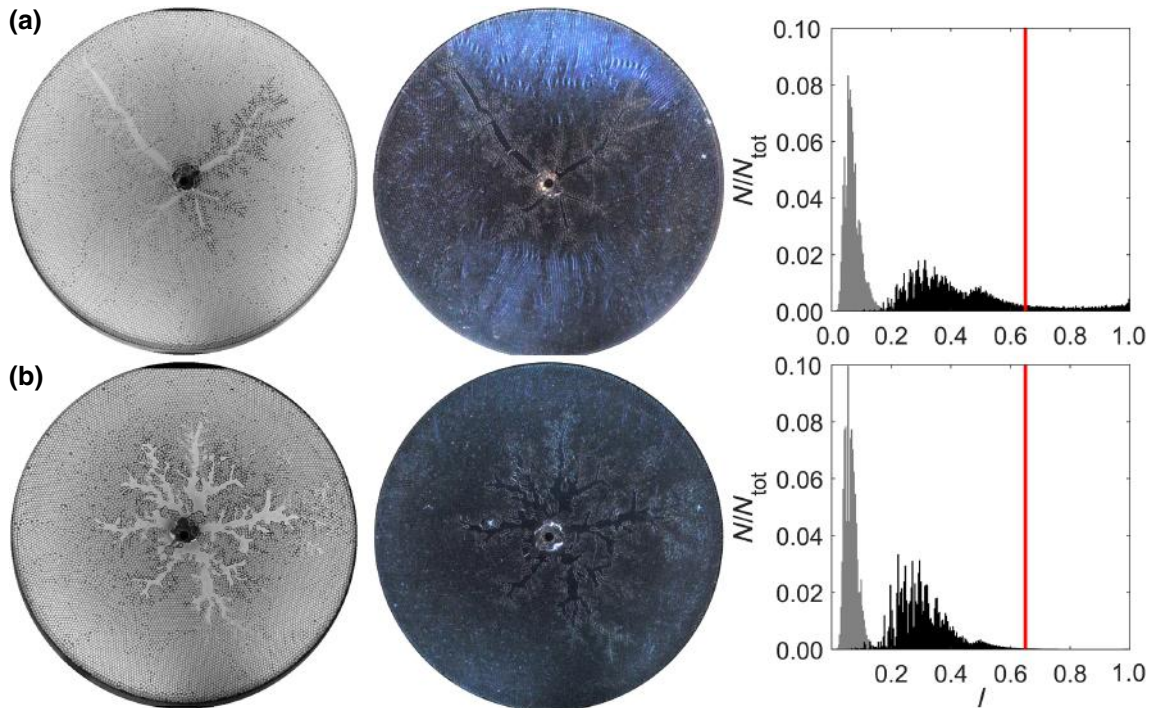
FIG. 2. Bright-field (left) and dark-field (middle) images of the invading fluid morphology at breakthrough and a histogram (right) of the light intensity of the blue channel of the dark-field image before air injection (in gray) and at breakthrough (in black), corresponding to two different initial packing densities ϕ_0, with confining weight $W = 25$ N. From the dark-field images that visualize the effective stress field, the invading morphology and rheology of the granular packs are classified as (a) fracturing in fluid-filled elastic media, with a strong photoelastic response ($I > 0.65$), $\phi_0 = 0.84$, or (b) viscous fingering in frictional fluids, with a weak or negligible photoelastic response ($I < 0.65$), $\phi_0 = 0.78$. Behind the propagating fracture tips, the effective stress field exhibits an evolving "effective stress shadow," where the intergranular stress is low and the granular pack exhibits undrained behavior. For the evolution of the morphology in each regime, see the videos in the Supplemental Material [35].

fracture branches or pore invasion, both of which contribute to lifting the top plate. During air injection, while all the particles are in contact with both the top and bottom plates ($h(t) < d$), the confining weight is balanced by contact forces between particles and plates and the integrated pore-pressure force across the Hele-Shaw cell. When the top plate is lifted to $h(t) > d$, the vertical component of the interparticle force is negligible and the confining weight is balanced by the integrated pore-pressure force only.

We determine the spatiotemporal evolution of the packing density and effective stress fields as described in Sec. II [Figs. 3(e) and 3(f)]. As fractures propagate, the pack is compacted ahead of the fracture tips but exhibits a lower packing density around the fractures, reflecting the moving-average procedure that we use to determine it. In the fracturing experiments [Fig. 7 in Appendix A], we observe an asymmetric fracturing morphology with four to six fracture branches in total and with one or two of them propagating faster and soon reaching the boundary. In an effort to characterize the rheological heterogeneity of the granular pack robustly and consistently across all the fracturing experiments, we define the fracture radius

(r_{frac}) as the average distance from three representative fracture tips to the injection port, including both the long fractures that first reach the boundary and one or two shorter fractures near the injection port. As fractures propagate, the fracture radius increases and the effective stress field exhibits marked rheological heterogeneity [Fig. 3(f)]. Behind the fracture tips ($r < r_{\mathrm{frac}}(t)$), we discover an *effective stress shadow*, where the intergranular stress is low and the granular pack exhibits undrained behavior. Ahead of the fracture tips ($r > r_{\mathrm{frac}}(t)$), particles in the annular region are compacted and behave elastically. For the annular region, this distinct rheological behavior from a frictional to an elastic response can be understood as a *jamming transition* [39,40]. This is further evidenced by the temporal evolution of the averaged packing density and effective stress in the annular region outside fractures, ϕ_{out} and σ'_{out} [Fig. 3(c)], both of which rise above a background value at the critical point of mechanical stability (ϕ_c, σ'_c) [28,39–41]. To show that fracturing is indeed the result of the transition to a solidlike rheological behavior, we analyze the evolution of the packing fraction as a function of the radial distance, $\phi(r)$, at different times, alongside the position of the fracture tip, for one of the fracturing
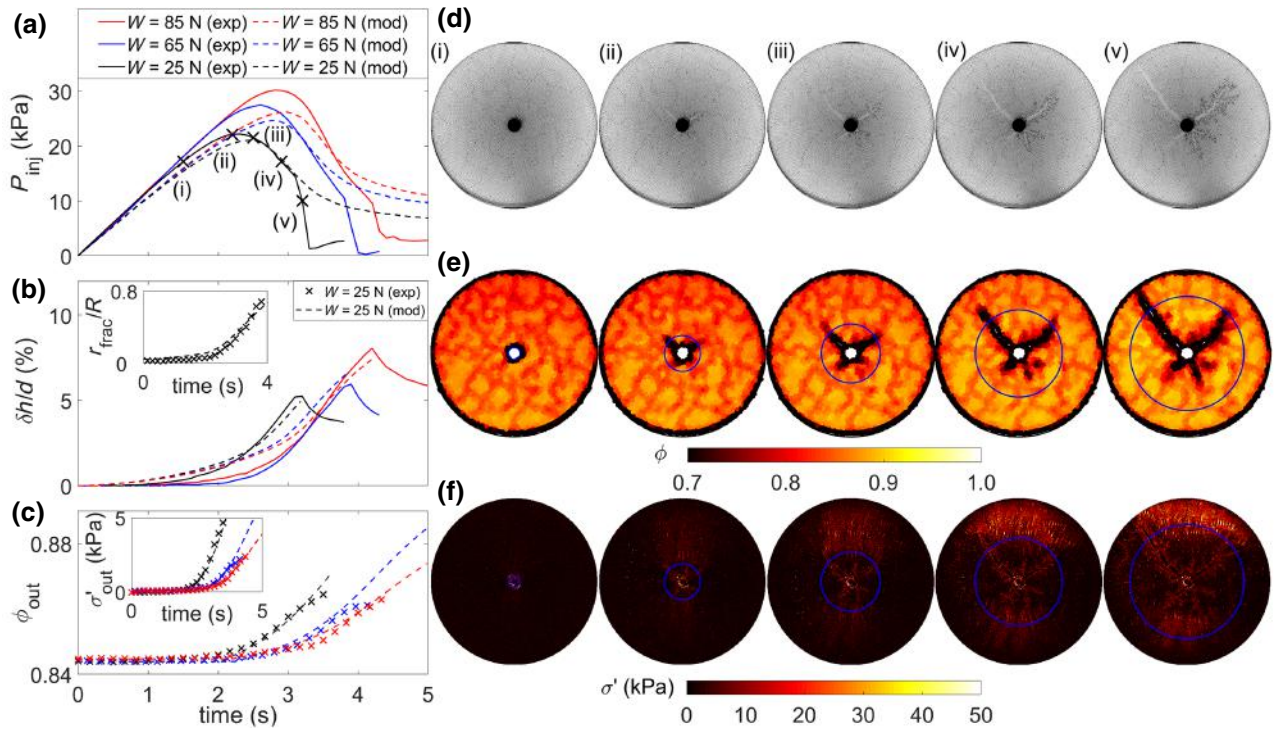
FIG. 3.   (a)–(c) The time evolution of (a) the injection pressure P_{inj}, (b) the normalized vertical displacement of the top plate $\delta h/d$, and (c) the averaged packing density ϕ_{out} in the annular region outside fractures for experiments with initial packing density $\phi_0 = 0.84$ and $W = 25$ N, 65 N, and 85 N. The insets of (b) and (c) show the time evolution of the normalized fracture radius r_{frac}/R and the averaged effective stress σ'_{out} in the annular region outside fractures. The modeling results are plotted in dashed lines. (d)–(f) For the experiment with $\phi_0 = 0.84$ and $W = 25$ N, a sequence of snapshots shows the time evolution of (d) the interface morphology, (e) the packing-density field, and (f) the effective stress field, where the radius of the blue circle represents the fracture radius (r_{frac}) averaged from three representative fracture tips.

experiments ($\phi_0 = 0.84$, $W = 25$ N; Fig. 4). The initial packing fraction is sufficiently close to the critical packing fraction ϕ_c that a relatively minor compaction elicits the formation and initial propagation of a fracture. The granular pack jams at some time between t_{ii} and t_{iii}, after which the fracture tip travels across the outer annular region, which is all above ϕ_c.

Where does the effective stress shadow come from? And how does the rheology of a granular medium evolve during the fracturing process? To answer these questions, we hypothesize that the evolving effective stress shadow—the exhibited undrained behavior—stems from the build-up of pore pressure within the wedges of granular media between propagating fractures. The hypothesis emphasizes the strong coupling between the fluid flow and solid mechanics underpinning the fracturing process.

To analyze the spatiotemporal evolution of the pore pressure, we develop a mechanistic model for a representative fracture wedge with an angle θ—a sector of the fluid-filled granular medium delineated by two fractures originating from the cell center [Fig. 5(a)]. We assume Hertz–Mindlin contacts [42] between particles and the

plates and calculate the initial vertical compression of the granular pack under the confining weight ($h_0 < d$). We model the fracturing process until breakthrough. The proposed model for a representative fracture wedge with an angle θ solves the time evolution of four unknowns: (1) the injection pressure $P_{inj}(t)$; (2) the height of the granular pack $h(t)$; (3) the length of the fracture $r_{frac}(t)$; and (4) the azimuthally dependent pore-pressure field $p(r, \theta, t)$. The set of governing equations, along with their derivation and working modeling assumptions, is included in Appendix B.

The modeling results of P_{inj}, h and r_{frac} for different confining weights show good agreement with the experimental data [Figs. 3(a) and 3(b)]. The time evolution of the pore-pressure field during fracturing provides important clues to decipher the behavior of the system [Fig. 5(c)]. The flow-velocity field demonstrates a highly inhomogeneous distribution of the pore-pressure gradient, which concentrates near the fracture tips [Fig. 5(b)]. The model captures the pressure build-up inside the fracture radius, resulting in the aforementioned "effective stress shadow," a region in which the granular pack is under near-undrained conditions. These fluidized particles in the stress shadow
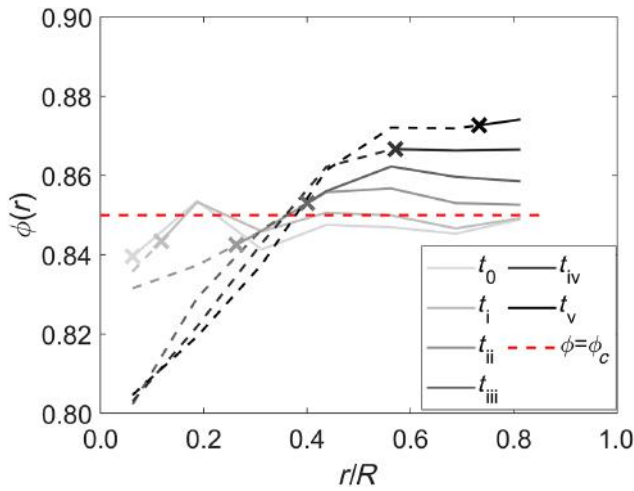
FIG. 4. The radial distribution of the packing fraction ($\phi(r)$) for the fracturing experiment with $\phi_0 = 0.84$ and $W = 25$ N. The temporal evolution of $\phi(r)$ is plotted at six time instances, t_0 at $t = 0$ and $t_i \sim t_v$ in Fig. 3. The location of the fracture tip is indicated with the cross marker. The packing-fraction distribution behind the fracture tip is plotted in dashed lines and ahead of the fracture tip in solid lines. The red dashed line shows the packing fraction at the jamming transition, $\phi = \phi_c = 0.85$.

lead to grain compaction in the annular region outside, which helps explain the distinct rheological behavior from a frictional to an elastic response [Fig. 5(a)].

With the insights from the pore-pressure model, we expect a different fluid-flow behavior in the loose and

dense regions of the granular pack: a granular-fluid mixture behind the fracture tips and an elastic medium ahead of the fracture tips. The homogeneous-granular-pack assumption in the pressure model (Appendix B) does not reflect the disparate rheology. For the rheology model, we take an effective permeability k' [43] and viscosity η' [36] for the granular-fluid mixture within the fracture radius and approximate the number of particles $N_{\delta t}$ entering the annular region within a time step as $N_{\delta t} = (v_p \delta t/d)[r_{\text{frac}}(t)\theta/d]$, with $v_p = -(k'/\eta')(\partial p/\partial r)|_{r=r_{\text{frac}}(t)}$, where v_p is the particle flow velocity at the fracture radius. We update the 2D packing density in the annular region as

$$\phi(t + \delta t) = \phi(t) + \frac{N_{\delta t}\frac{\pi d^2}{4}}{\frac{1}{2}(R^2 - (r_{\text{frac}}(t))^2)\theta}. \quad (1)$$

To infer the effective stress from the packing density, we adopt the power-law constitutive relationship $\sigma' - \sigma'_c = K\langle(\phi - \phi_c)/\phi_c\rangle^{\psi}$ [39,40,44–46]. The modeling results of $(\phi(t), \sigma'(t))$ in the annular region agree well with the experiments [Fig. 3(c)], capturing both the pore-pressure evolution and rheology of the granular medium. A detailed account of the modeling parameters is included in Appendix B.

To explore the rheological properties of the granular medium in the annulus, we conduct the jamming transition analysis for the fracturing experiments. We determine the jamming transition ϕ_c from the time evolution of the effective stress σ' as the intersection of two straight lines: one fitting the response of the background state and the other
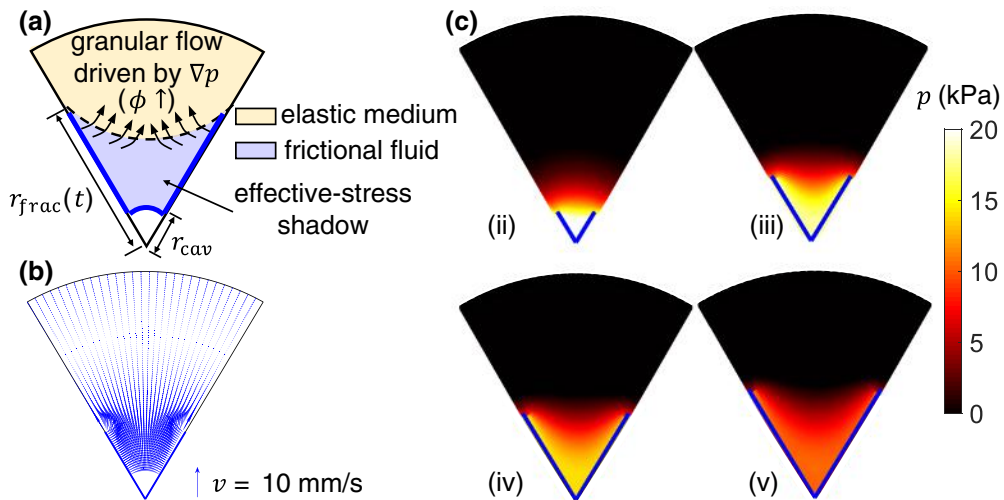

FIG. 5. A mechanistic model on fracturing that explains the effective stress shadow observed in experiments. (a) A schematic of the model setup for a fracture wedge with an angle $\theta = 60°$. The granular flow driven by the concentrated pore-pressure gradient within fracture tips keeps compacting particles in the annular region outside, leading to its increase in packing density and a rheological transition from frictional flow to elastic medium. (b) The modeled flow-velocity field at time instance (iii) in Fig. 3(a). (c) A sequence of snapshots showing the time evolution of the modeling pore-pressure field. Modeling conditions: $\phi_0 = 0.84$, $W = 25$ N, $q = 100$ ml/min, and $V_0 = 15$ ml.
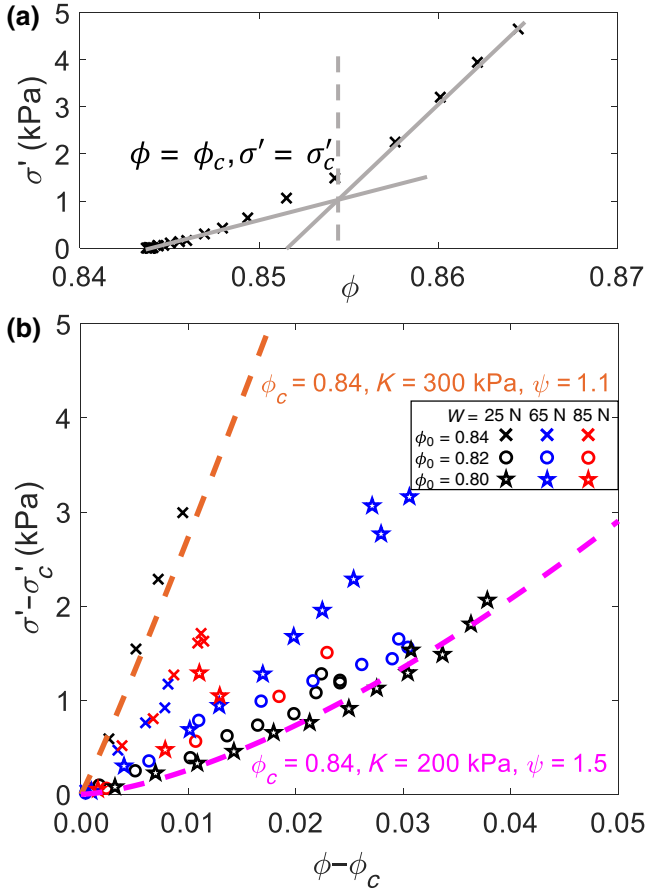
FIG. 6. The jamming-transition analysis for the fracturing experiments ($\phi_0 = 0.84$, 0.82, and 0.80; $W = 25$ N, 65 N, and 85 N). (a) The determination of the critical packing density and effective stress at jamming for the experiment $W = 25$ N, $\phi_0 = 0.84$. (b) $\sigma' - \sigma_c'$ plotted against $\phi - \phi_c$ for the fracturing experiments, which follows the power-law constitutive relationship $\sigma' - \sigma_c' = K \left\langle \frac{\phi - \phi_c}{\phi_c} \right\rangle^\psi$ [39,40,44–46].

fitting the asymptotic behavior in the highly compacted state [28,40,47] [Fig. 6(a)]. We find that ϕ_c lies in the range 0.83–0.85 for the fracturing experiments [Fig. 2(a) and regime I in Appendix A], with a higher ϕ_c corresponding to denser granular packs. The experimental value of ϕ_c is consistent with the theoretical prediction that the system jams at the random-close-packing density $\phi_c \approx \phi_{\rm rcp} \approx$ 0.84 [28,48–50]. We synthesize the elastic response of the system by plotting the effective stress against the packing density, showing that, above ϕ_c, σ' follows a power-law increase, $\sigma' - \sigma_c' \sim (\phi - \phi_c)^\psi$, with the exponent ψ in the range 1.1–1.5 [Fig. 6(b)]. As confirmed in previous studies [28,39,40,44,45], the value of ψ lies between the value for linear ($\psi = 1.0$) and Hertzian contacts ($\psi = 1.5$). In our stress-strain diagram [Fig. 6(b)], the elastic response in the annular region indicates a value of $K \sim 200$–300 kPa,

which is close to the value measured in separate experiments [30]. Ideally, the parameters in the constitutive relation (K, ψ) would be the same for all the experiments, reflecting the elastic behavior of the material after the jamming transition. In the experiments, though, this is not the case, and the coefficients in the power law exhibit some variability in part at least due to the asymmetric fracturing morphology and the inhomogeneous distribution of the packing fraction and effective stress fields ahead of the fracture tips. In an effort to characterize the rheological heterogeneity of the granular pack more robustly, in our mathematical model, we define the fracture radius ($r_{\rm frac}$) as the averaged distance from three representative fracture tips to the injection port.

IV. CONCLUSIONS

In summary, we study the morphology and rheology of injection-induced fracturing in wet granular packs via a recently developed experimental technique, photoporomechanics, which extends photoelasticity to granular systems with a fluid-filled connected pore space [30]. Experiments of air injection into photoelastic granular packs with different initial packing densities and confining weights lead us to uncover two invasion regimes: fracturing in fluid-filled elastic media and viscous fingering in frictional fluids. Visualizing the evolving effective stress field using photoporomechanics, we discover that behind the fracture tips, an *effective stress shadow*—where the intergranular stress is low and the granular pack exhibits undrained behavior—evolves as fractures propagate. With a mechanistic model for a fracture wedge, we capture the fluid pressure build-up inside the shadow region. We develop a rheology model that explains both the effective stress shadow behind the fracture tips and the distinct rheological behavior from a frictional to an elastic response for the granular medium outside the fractures. Finally, we rationalize the emergence of fracturing across our experiments as a jamming transition, initially proposed in the context of coupled pore-network and discrete-element models [28].

Our study hopefully paves the way for understanding the mechanical and fracture properties of porous media that are of interest for many field applications, including plant root growth in granular material [31,51], powder aggregation [52], rock mechanics [53], soil rheology [54], and geoengineering [55]. We demonstrate that photoporomechanics may serve as an effective technique to study coupled fluid-solid processes in granular media [4] and may provide fundamental insights on specific applications, including energy recovery [56], gas venting [57], and geohazards [58].
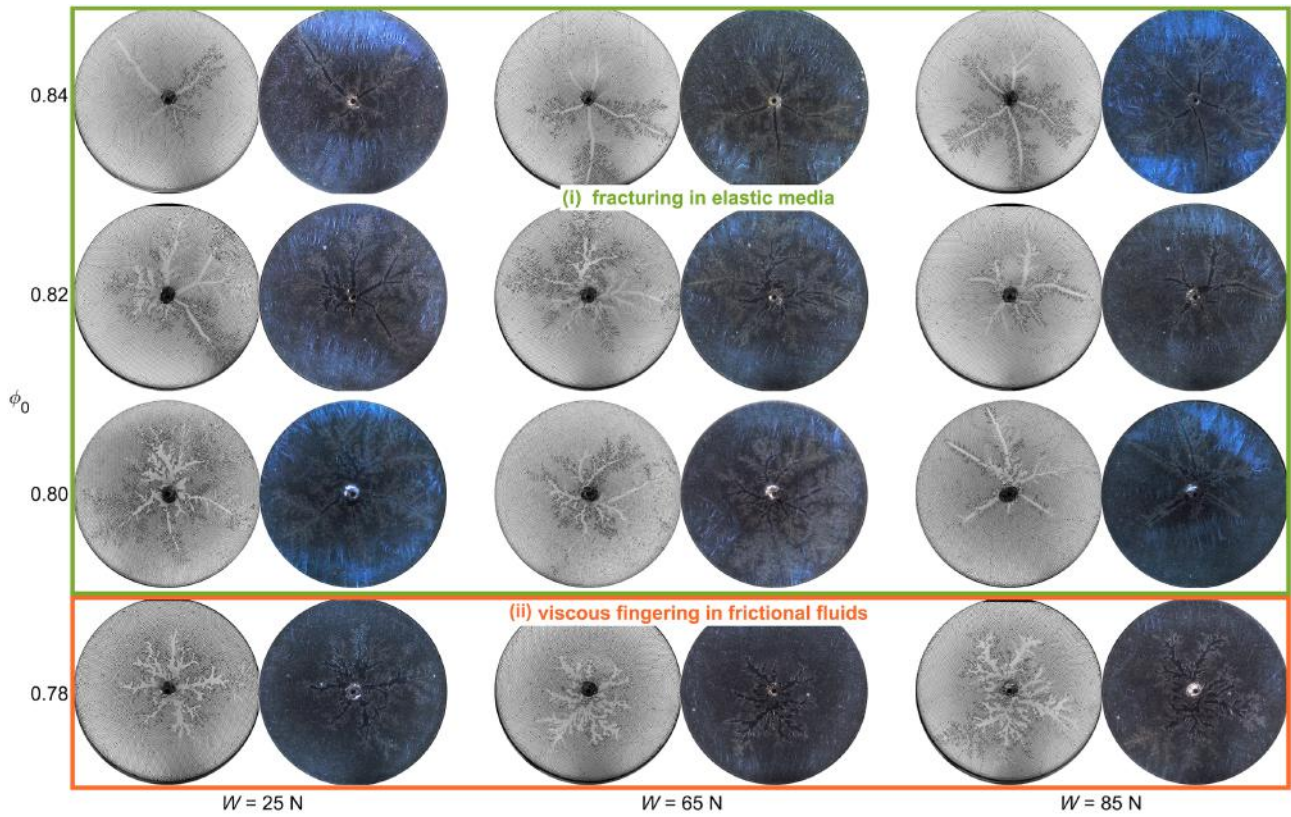
FIG. 7.   A visual phase diagram of the bright-field (left) and dark-field (right) invading fluid morphology at breakthrough corresponding to different confining weights W and initial packing densities ϕ_0. From dark-field images that visualize the effective stress field, the invading morphology and rheology of the granular packs is classified as fracturing in fluid-filled elastic media (with a strong photoelastic response, $\phi_0 = 0.84$, 0.82, and 0.80), or viscous fingering in frictional fluids (with a weak or negligible photoelastic response, $\phi_0 = 0.78$). Behind the propagating fracture tips, the effective stress field exhibits an evolving "effective stress shadow," where the intergranular stress is low and the granular pack exhibits undrained behavior.

APPENDIX A: THE COMPLETE VISUAL PHASE DIAGRAM OF INVADING FLUID MORPHOLOGY AT BREAKTHROUGH

Figure 7 shows the complete visual phase diagram of invading fluid morphology for a range of values of ϕ_0 and W.

APPENDIX B: MATHEMATICAL MODEL OF COUPLED FLUID PRESSURE AND GRANULAR MECHANICS

We develop a mechanistic model for a representative fracture wedge with an angle θ_0. We assume Hertz-Mindlin contacts [42] between particles and the plates and calculate the initial vertical compression of the granular pack under the confining weight ($h_0 < d$). We model the fracturing process until breakthrough of the injected fluid. The model solves the time evolution of four unknowns: (1)

the injection pressure $P_{\text{inj}}(t)$; (2) the height of the granular pack $h(t)$; (3) the length of the fracture $r_{\text{frac}}(t)$; and (4) the azimuthally dependent pore-pressure field during fracturing, $p(r, \theta, t)$.

1. Governing equations

(1) We assume fluid flowing in a homogeneous porous medium of uniform packing density (ϕ_{3D}) and time-dependent uniform thickness ($h(t)$), in an azimuthally
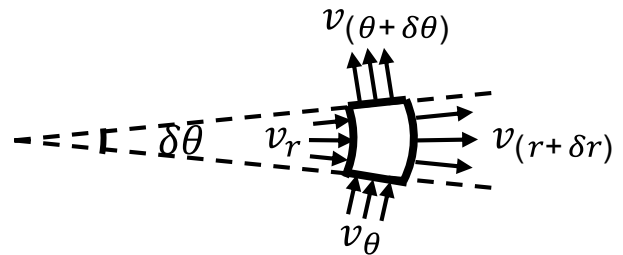

FIG. 8.   An annulus sector used to derive the pressure-diffusion equation in radial coordinates.

TABLE I. The modeling parameters for a mechanistic model of a representative fracture wedge

Symbol	Value	Unit	Variable
r_0	2	mm	Injection port radius
R	10.6	cm	Hele-Shaw cell radius
M_s	40	g	Mass of the photoelastic particles
ρ_s	1	g/cm^3	Density of the photoelastic particles
ϕ_{3D}	0.58, 0.59, 0.60		3D packing density under $W = 25$ N, 65 N, and 85 N
W	25, 65, 85	N	Confining weight acting on the granular pack
d	2	mm	Diameter of the photoelastic particles
K_n	9.4×10^7	N/m$^{(3/2)}$	Hertzian-contact normal stiffness of the granular pack
q	100	ml/min	Air injection rate
V_0	15	ml	Air-reservoir volume
P_0	101	kPa	Atmospheric pressure
θ	$\pi/3$		Angle of a representative fracture wedge
w	$3d$	mm	Fracture width
h_0	$0.98d, 0.96d, 0.95d$	mm	Initial height of the granular pack under $W = 25$ N, 65 N, and 85 N
k	$(0.08d)^2$	mm^2	Permeability of the granular pack
k'	$d^2/12$	mm^2	Effective permeability of the granular-fluid mixture
η	9.71	Pa s	Defending fluid viscosity
η'	9.8η	Pa s	Effective viscosity of the granular-fluid mixture [36]

dependent manner. We perform a mass balance on an annulus sector between r and $r + \delta r$, θ and $\theta + \delta\theta$ (Fig. 8) for the incompressible defending fluid (silicone oil):

$$\rho_f \left(v_r r\delta\theta h - v_{r+\delta r}(r + \delta r)\delta\theta h + v_\theta \delta rh - v_{\theta+\delta\theta}\delta rh \right)$$

$$= \frac{\partial(\rho_f r\delta r\delta\theta h(1 - \phi_{3D}))}{\partial t}, \tag{B1}$$

where ϕ_{3D} is the three-dimensional (3D) packing density of the granular pack, which is computed as the ratio between the volume of particles and the cell volume saturated with the defending silicone oil. Before the air injection, $\phi_{3D} = V_s/V_t = (M_s/\rho_s)/(\pi R^2 h_0)$, where M_s and ρ_s are the mass and density of the photoelastic particles in a granular pack, respectively. The initial cell height, h_0, is calculated from the confining weight by assuming Hertzian contacts between the particles and the glass plate. We estimate the 3D packing density before air injection and also at breakthrough, a calculation that shows a negligible difference between the two values. Therefore, in the model, we take the 3D packing fraction as a constant calculated with the initial cell height, $\phi_{3D,0}$. Dividing the equation by $\rho_f \delta r\delta\theta$ and letting $\delta r \to 0$ and $\delta\theta \to 0$:

$$-\frac{\partial(v_r rh)}{\partial r} - \frac{\partial(v_\theta h)}{\partial\theta} = \frac{\partial(rh(1 - \phi_{3D}))}{\partial t}. \tag{B2}$$

Combining with Darcy's law for the fluid velocity, we obtain

$$\frac{\partial(rh\frac{k}{\eta}\frac{\partial p}{\partial r})}{\partial r} + \frac{\partial(\frac{h}{r}\frac{k}{\eta}\frac{\partial p}{\partial\theta})}{\partial\theta} = \frac{\partial(rh(1 - \phi_{3D}))}{\partial t}, \tag{B3}$$

where k is the permeability of the granular pack and η is the viscosity of the defending fluid. We assume ϕ_{3D}, k, and η to be constant in space and time. We then obtain the pressure diffusion equation for the defending fluid (silicone oil) in cylindrical coordinates as follows:

$$\frac{kh}{\eta}\left(\frac{\partial^2 p}{\partial r^2} + \frac{1}{r}\frac{\partial p}{\partial r} + \frac{1}{r^2}\frac{\partial^2 p}{\partial\theta^2}\right) = (1 - \phi_{3D})\frac{\partial h}{\partial t}. \tag{B4}$$

(2) The conservation of mass for the total air in the system is as follows:

$$P_{inj}(t)(V_0 - qt + V_{air}(t)) = P_0(V_0 + \pi r_0^2 h_0), \tag{B5}$$

$$V_{air}(t) = \pi r_0^2 h(t) + V_{frac}(t) \tag{B6}$$

$$V_{frac}(t) = \frac{2\pi}{\theta_0}(r_{frac}(t) - r_0)wh(t), \tag{B7}$$

where V_0 is the syringe volume before air injection, r_0 is the injection port radius, $V_{air}(t)$ is the air volume in the cell, which consists of the air volume at the injection port and the volume of fractures $V_{frac}(t)$, w is the fracture width, and P_0 is the atmospheric pressure.

(3) Assuming incompressible solid grains, conservation of mass for the solid grains states that

$$\frac{\partial V_s}{\partial t} = 0 \to \frac{\partial[(V_t(t) - V_{air}(t))\phi_{3D}]}{\partial t} = 0, \tag{B8}$$

where $V_t(t)$ is the total cell volume. As ϕ_{3D} is a constant with time, the equation becomes

$$V_{air}(t) = \pi R^2(h(t) - h_0) + \pi r_0^2 h_0, \tag{B9}$$
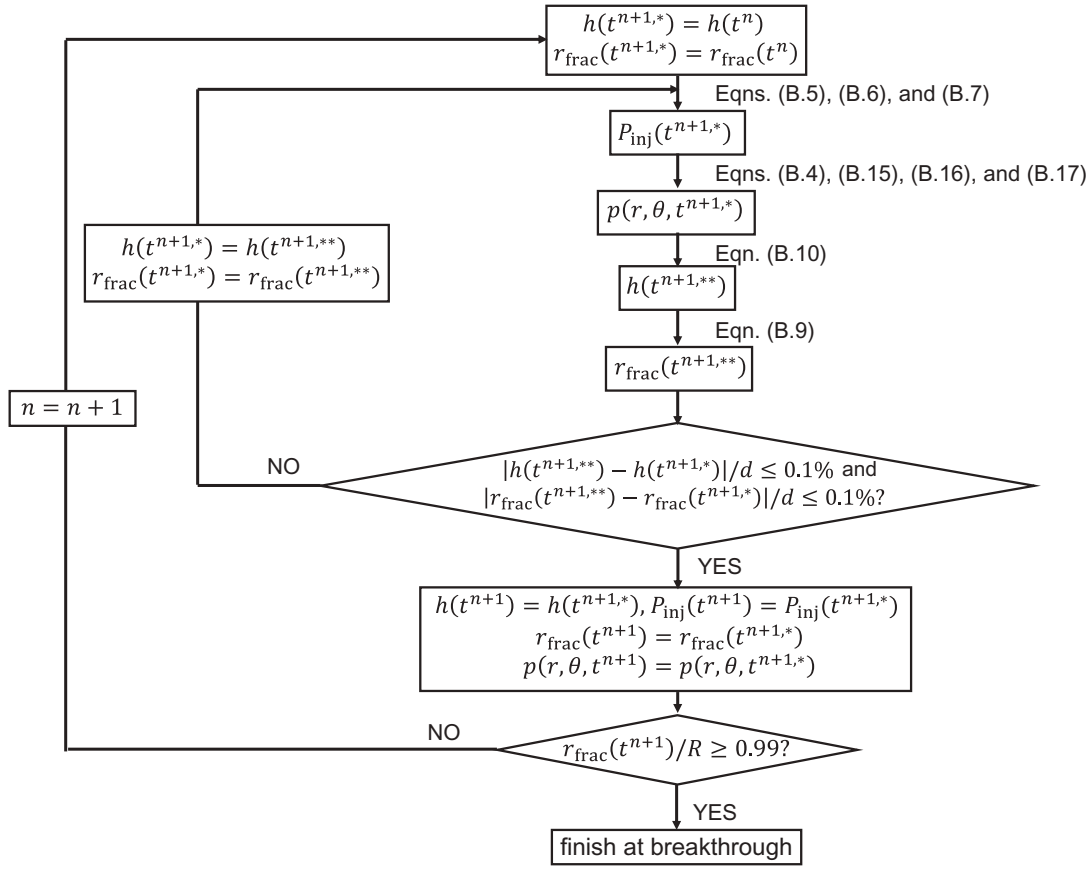
where R is the radius of the cell.

FIG. 9.   The numerical implementation scheme for the mathematical model. The fluid pressure is fully coupled with the granular mechanics by solving the unknown variables, $h(t)$ and $r_{\text{frac}}(t)$, iteratively until convergence at each time step.

(4) We establish the quasistatic force balance for the top plate assuming Hertzian contacts for the granular pack. When all the particles are in contact with both the top and bottom plates ($h(t) < d$), the confining weight is balanced by contact forces between particles and plates and the integrated pore-pressure force. When the top plate is lifted to $h(t) > d$, particles have contacts with either the top or bottom plate and the vertical component (F_v) of the interparticle force (F_p) is negligible from the geometric configuration, $F_v/F_p = (h - d)/d < 0.03$, and thus the confining weight is balanced by the integrated pore-pressure force only:

$$
K_n \Big((d - h(t)) \Big)^{\frac{3}{2}} + P_{\text{inj}}(t)\pi r_0^2
$$

$$
+ \frac{2\pi}{\theta_0} \int_{r_0}^{R} \int_{-\frac{\theta_0}{2}}^{\frac{\theta_0}{2}} p(r,\theta,t)r \, d\theta \, dr = W, \quad \text{(B10)}
$$

where K_n is the contact normal stiffness of the granular pack under the confining weight.

2. Initial and boundary conditions

The initial conditions for the four unknowns ($P_{\text{inj}}(t)$, $h(t)$, $r_{\text{frac}}(t)$, and $p(r,\theta,t)$) are as follows:

$$
P_{\text{inj}}(t = 0) = 0, \quad \text{(B11)}
$$

$$
h(t = 0) = h_0 = d - \left(\frac{W}{K_n}\right)^{2/3}, \quad \text{(B12)}
$$

$$
r_{\text{frac}}(t = 0) = r_0, \quad \text{(B13)}
$$

$$
p\left(r_0 \le r \le R, -\frac{\theta_0}{2} \le \theta \le \frac{\theta_0}{2}, t = 0\right) = 0. \quad \text{(B14)}
$$

The boundary conditions are

$$
p(R, \theta, 0) = 0, \quad \text{(B15)}
$$

$$
p(r_0 \le r \le r_{\text{frac}}(t), \pm\theta_0/2, t) = p(r_0, \theta, t) = P_{\text{inj}}(t), \quad \text{(B16)}
$$

$$
\left.\frac{\partial p}{\partial \theta}\right|_{(r_{\text{frac}}(t) \le r \le R, \pm\theta_0/2, t)} = 0. \quad \text{(B17)}
$$

3. Modeling parameters

A summary of the modeling parameters is shown in Table I. There is no fitting parameter in this model. The

Hertzian-contact normal stiffness, K_n, is measured from a separate experiment where we track the vertical displacement of the top plate as the confining weight increases from 10 N to 110 N. The permeability of the granular pack, k, is measured in consolidation experiments [30]. Other parameters are either calculated from the experimental setup (r_0, R, M_s, ρ_s, ϕ_{3D}, W, d, q, V_0, P_0, h_0, k', η, and η') or directly measured during the fracturing experiments (w and θ_0).

4. Numerical implementation

We use a finite-difference numerical scheme to solve the four coupled governing equations [Eqs. (B4), (B5), (B9), and (B10)]. The numerical implementation scheme for the mathematical model is shown in Fig. 9. The fluid pressure is fully coupled with granular mechanics by solving the unknown variables, $h(t)$ and $r_{\text{frac}}(t)$, iteratively until convergence at each time step.

---

[1] D. E. Hill and J.-Y. Parlange, Wetting front instability in layered soils, Soil Sci. Soc. Am. J. **36**, 697 (1972).

[2] G. T. Charras, J. C. Yarrow, M. A. Horton, L. Mahadevan, and T. J. Mitchison, Non-equilibration of hydrostatic pressure in blebbing cells, Nature **435**, 365 (2005).

[3] M. L. Szulczewski, C. W. MacMinn, H. J. Herzog, and R. Juanes, Lifetime of carbon capture and storage as a climate-change mitigation technology, ' Proc. Natl. Acad. Sci. USA **109**, 5185 (2012).

[4] R. Juanes, Y. Meng, and B. K. Primkulov, Multiphase flow and granular mechanics, Phys. Rev. Fluids **5**, 110516 (2020).

[5] A. Groisman and E. Kaplan, An experimental study of cracking induced by desiccation, Europhys. Lett. **25**, 415 (1994).

[6] H. Shin and J. C. Santamarina, Desiccation cracks in saturated fine-grained soils: Particle-level phenomena and effective-stress analysis, Geotechnique **61**, 961 (2011).

[7] E. R. Dufresne, E. I. Corwin, N. A. Greenblatt, J. Ashmore, D. Y. Wang, A. D. Dinsmore, J. X. Cheng, X. S. Xie, J. W. Hutchinson, and D. A. Weitz, Flow and Fracture in Drying Nanoparticle Suspensions, Phys. Rev. Lett. **91**, 224501 (2003).

[8] D. Vella, P. Aussillous, and L. Mahadevan, Elasticity of an interfacial particle raft, Europhys. Lett. **68**, 212 (2004).

[9] A. K. Jain and R. Juanes, Preferential mode of gas invasion in sediments: Grain-scale mechanistic model of coupled multiphase fluid flow and sediment mechanics, J. Geophys. Res. Solid Earth **114**, B08101 (2009).

[10] H. Shin and J. C. Santamarina, Fluid-driven fractures in uncemented sediments: Underlying particle-level processes, Earth Planet. Sci. Lett. **299**, 180 (2010).

[11] L. Goehring, W. J. Clegg, and A. F. Routh, Plasticity and Fracture in Drying Colloidal Films, Phys. Rev. Lett. **110**, 024301 (2013).

[12] C. Peco, W. Chen, Y. Liu, M. M. Bandi, J. E. Dolbow, and E. Fried, Influence of surface tension in the surfactant-driven fracture of closely-packed particulate monolayers, Soft Matter **13**, 5832 (2017).

[13] Z. Sun and J. C. Santamarina, Grain-displacive gas migration in fine-grained sediments, J. Geophys. Res. Solid Earth **124**, 2274 (2019).

[14] B. Sandnes, H. A. Knudsen, K. J. Måløy, and E. G. Flekkøy, Labyrinth Patterns in Confined Granular-Fluid Systems, Phys. Rev. Lett. **99**, 038001 (2007).

[15] X. Cheng, L. Xu, A. Patterson, H. M. Jaeger, and S. R. Nagel, Towards the zero-surface-tension limit in granular fingering instability, Nat. Phys. **4**, 234 (2008).

[16] H. Huang, F. Zhang, P. Callahan, and J. Ayoub, Granular Fingering in Fluid Injection into Dense Granular Media in a Hele-Shaw Cell, Phys. Rev. Lett. **108**, 258001 (2012).

[17] F. Zhang, B. Damjanac, and H. Huang, Coupled discrete element modeling of fluid injection into dense granular media, J. Geophys. Res. Solid Earth **118**, 2703 (2013).

[18] B. Sandnes, E. G. Flekkøy, H. A. Knudsen, K. J. Måløy, and H. See, Patterns and flow in frictional fluid dynamics, Nat. Commun. **2**, 288 (2011).

[19] B. P. Scandella, L. Pillsbury, T. Weber, C. Ruppel, H. F. Hemond, and R. Juanes, Ephemerality of discrete methane vents in lake sediments, Geophys. Res. Lett. **43**, 4374 (2016).

[20] T. W. Patzek, F. Male, and M. Marder, Gas production in the Barnett shale obeys a simple scaling theory, Proc. Natl. Acad. Sci. USA **110**, 19731 (2013).

[21] J. Mataix-Solera, V. Arcenegui, N. Tessler, R. Zornoza, L. Wittenberg, C. Martínez, P. Caselles, A. Pérez-Bejarano, D. Malkinson, and M. M. Jordán, Soil properties as key factors controlling water repellency in fire-affected areas: Evidences from burned sites in Spain and Israel, Catena **108**, 6 (2013).

[22] R. Holtzman, M. L. Szulczewski, and R. Juanes, Capillary Fracturing in Granular Media, Phys. Rev. Lett. **108**, 264504 (2012).

[23] R. Holtzman and R. Juanes, Crossover from fingering to fracturing in deformable disordered media, Phys. Rev. E **82**, 046305 (2010).

[24] B. Carrier and S. Granet, Numerical modeling of hydraulic fracture problem in permeable medium using cohesive zone model, Eng. Fract. Mech. **79**, 312 (2012).

[25] B. Lecampion and J. Desroches, Simultaneous initiation and growth of multiple radial hydraulic fractures from a horizontal wellbore, J. Mech. Phys. Solids **82**, 235 (2015).

[26] A. Mikelic, M. F. Wheeler, and T. Wick, A phase-field method for propagating fluid-filled fractures coupled to a surrounding porous medium, Multiscale Model. Simul. **13**, 367 (2015).

[27] D. Santillán, R. Juanes, and L. Cueto-Felgueroso, Phase field model of hydraulic fracturing in poroelastic media: Fracture propagation, arrest, and branching under fluid injection and extraction, J. Geophys. Res.: Solid Earth **123**, 2127 (2018).

[28] Y. Meng, B. K. Primkulov, Z. Yang, C. Y. Kwok, and R. Juanes, Jamming transition and emergence of fracturing in wet granular media, Phys. Rev. Res. **2**, 022012 (2020).

[29] F. J. Carrillo and I. C. Bourg, Capillary and viscous fracturing during drainage in porous media, Phys. Rev. E **103**, 063106 (2021).

[30] W. Li, Y. Meng, B. K. Primkulov, and R. Juanes, Photo-Poromechanics: An Experimental Method to Visualize the

Effective Stress Field in Fluid-Filled Granular Media, Phys. Rev. Appl. **16,** 024043 (2021).

[31] J. Barés, S. Mora, J.-Y. Delenne, and T. Fourcaud, in *EPJ Web of Conferences*, Vol. 140 (EDP Sciences, Les Ulis, France, 2017), p. 14008.

[32] K. E. Daniels, J. E. Kollmer, and J. G. Puckett, Photoelastic force measurements in granular materials, Rev. Sci. Instrum. **88,** 051808 (2017).

[33] M. L. Falk and J. S. Langer, Dynamics of viscoplastic deformation in amorphous solids, Phys. Rev. E **57,** 7192 (1998).

[34] L. Rothenburg and A. P. S. Selvadurai, in *Mechanics of Structural Media, Proc. of the Int. Symp. on the Mechanical Behaviour of Structured Media, Ottawa, Canada, 18–21 May* (Elsevier, Amsterdam, Netherlands, 1981), p. 469.

[35] See the Supplemental Material at http://link.aps.org/supplemental/10.1103/PhysRevApplied.18.064081 for videos corresponding to the conditions in Fig. 2.

[36] D. Quemada, Rheology of concentrated disperse systems and minimum energy dissipation principle, Rheol. Acta **16,** 82 (1977).

[37] P. G. Saffman and G. I. Taylor, The penetration of a fluid into a porous medium or Hele-Shaw cell containing a more viscous liquid, Proc. R. Soc. A—Math. Phys. Eng. Sci. **245,** 312 (1958).

[38] C. Chevalier, A. Lindner, M. Leroux, and E. Clément, Morphodynamics during air injection into a confined granular suspension, J. Non-Newton. Fluid Mech. **158,** 63 (2009).

[39] C. S. O'Hern, L. E. Silbert, A. J. Liu, and S. R. Nagel, Jamming at zero temperature and zero applied stress: The epitome of disorder, Phys. Rev. E **68,** 011306 (2003).

[40] T. S. Majmudar, M. Sperl, S. Luding, and R. P. Behringer, Jamming Transition in Granular Systems, Phys. Rev. Lett. **98,** 058001 (2007).

[41] H. A. Makse, N. Gland, D. L. Johnson, and L. Schwartz, Granular packings: Nonlinear elasticity, sound propagation, and collective relaxation dynamics, Phys. Rev. E **70,** 061302 (2004).

[42] K. L. Johnson, *Contact Mechanics* (Cambridge University Press, Cambridge, UK, 1987).

[43] P. K. Kundu, I. M. Cohen, and D. Dowling, *Fluid Mechanics* (Elsevier, Amsterdam, Netherlands, 2008).

[44] C. S. O'Hern, S. A. Langer, A. J. Liu, and S. R. Nagel, Random Packings of Frictionless Particles, Phys. Rev. Lett. **88,** 075507 (2002).

[45] L. E. Silbert, D. Ertaş, G. S. Grest, T. C. Halsey, and D. Levine, Geometry of frictionless and frictional sphere packings, Phys. Rev. E **65,** 031304 (2002).

[46] C. W. MacMinn, E. R. Dufresne, and J. S. Wettlaufer, Fluid-Driven Deformation of a Soft Granular Material, Phys. Rev. X **5,** 011020 (2015).

[47] C. Heussinger and J.-L. Barrat, Jamming Transition as Probed by Quasistatic Shear Flow, Phys. Rev. Lett. **102,** 218303 (2009).

[48] J. G. Berryman, Random close packing of hard spheres and disks, Phys. Rev. A **27,** 1053 (1983).

[49] M. P. Ciamarra, R. Pastore, M. Nicodemi, and A. Coniglio, Jamming phase diagram for frictional particles, Phys. Rev. E **84,** 041308 (2011).

[50] N. Xu, J. Blawzdziewicz, and C. S. O'Hern, Random close packing revisited: Ways to pack frictionless disks, Phys. Rev. E **71,** 061306 (2005).

[51] D. M. Wendell, K. Luginbuhl, J. Guerrero, and A. E. Hosoi, Experimental investigation of plant root growth through granular substrates, Exp. Mech. **52,** 945 (2012).

[52] K. Kendall and C. Stainton, Adhesion and aggregation of fine particles, Powder Technol. **121,** 223 (2001).

[53] J. C. Jaeger, N. G. W. Cook, and R. Zimmerman, *Fundamentals of Rock Mechanics* (John Wiley & Sons, Hoboken, New Jersey, U.S., 2009).

[54] J. K. Mitchell and K. Soga, *Fundamentals of Soil Behavior* (John Wiley & Sons, New York, Hoboken, New Jersey, U.S., 2005), Vol. 3.

[55] D. L. Turcotte, E. M. Moores, and J. B. Rundle, Super fracking, Phys. Today **67,** 34 (2014).

[56] E. Ghanbari and H. Dehghanpour, The fate of fracturing water: A field and simulation study, Fuel **163,** 282 (2016).

[57] A. Skarke, C. Ruppel, M. Kodis, D. Brothers, and E. Lobecker, Widespread methane leakage from the sea floor on the northern US Atlantic margin, Nat. Geosci. **7,** 657 (2014).

[58] A. L. Handwerger, A. W. Rempel, R. M. Skarbek, J. J. Roering, and G. E. Hilley, Rate-weakening friction characterizes both slow sliding and catastrophic failure of landslides, Proc. Natl. Acad. Sci. USA **113,** 10281 (2016).

Jamming transition and emergence of fracturing in wet granular media

Yue Meng [●],[1] Bauyrzhan K. Primkulov [●],[1] Zhibing Yang [●],[2] Chung Yee Kwok,[3] and Ruben Juanes [●][1,*]

[1]*Massachusetts Institute of Technology, 77 Massachusetts Avenue, Cambridge, Massachusetts 02139, USA*
[2]*State Key Laboratory of Water Resources and Hydropower Engineering Science, Wuhan University, Wuhan 430072, China*
[3]*The University of Hong Kong, Pokfulam Road, Hong Kong, China*

We study fluid-induced deformation of granular media, and the fundamental role of capillarity and wettability on the emergence of fracture patterns. We develop a hydromechanical computational model, coupling a "moving capacitor" dynamic network model of two-phase flow at the pore scale with a discrete element model of grain mechanics. We simulate the slow injection of a less viscous fluid into a frictional granular pack initially saturated with a more viscous, immiscible fluid. We study the impact of wettability and initial packing density, and find four different regimes of the fluid invasion: cavity expansion and fracturing, frictional fingers, capillary invasion, and capillary compaction. We explain fracture initiation as emerging from a jamming transition, and synthesize the system's behavior in the form of a phase diagram of jamming for wet granular media.

Immiscible fluid-fluid displacement in porous media is important in many natural and industrial processes, including the displacement of air by water during rainfall infiltration [1], storage of carbon dioxide in deep saline aquifers [2], contaminant soil remediation [3], enhanced oil recovery [4], and design of microfluidic devices [5]. While fluid-fluid displacement in rigid porous media has been studied in depth, fundamental gaps remain in our understanding of the interplay between multiphase flow in a granular medium and the displacement of the grain particles [6,7]. This interplay can lead to a wide range of patterns, including fractures [8–14], desiccation cracks [15,16], labyrinth structures [17], and granular and frictional fingers [18–21]. There are several controlling parameters behind the morphodynamics that govern the transition between the different regimes. A modified capillary number Ca* characterizes the crossover from capillary fingering to viscous fingering [22], and a transition from fingering to fracturing can be achieved either by decreasing frictional resistance [22], or setting the outer boundary as free [23]. The balance between frictional, viscous, and capillary forces has been studied in experiments [17,21,22] and simulations [10,24], and has helped understand the underlying mechanisms for a wide range of phenomena, including venting dynamics of an immersed granular layer [25–27], fractures in drying colloidal suspensions [8,12], and methane migration in lake sediments [28–31].

As one of the factors that influences multiphase flow in porous media, wettability (the relative affinity of the substrate to each of the fluids, and measured by the contact angle θ) has

been studied for decades. While much is now known about the role of wettability on multiphase displacements in porous media [32–47], fundamental gaps remain in the context of grain-scale mechanisms and their macroscale consequences. Given the importance of capillarity on the fracture of granular packs [10,14,21,22,24], here we focus on the impact of wetting properties on the emergence of such fracture patterns. We also adopt packing density as a control parameter, since it can lead to a transition from Saffman-Taylor instability to dendritic (or ramified) fingering patterns [48], or from frictional fingering to stick-slip bubbles [21].

In this Rapid Communication, we uncover four fluid-invasion morphological regimes under different initial packing densities and substrate wettabilities: cavity expansion and fracturing, frictional fingers, capillary invasion, and capillary compaction. To rationalize these simulation outputs, we propose to analyze the evolution of the system as one approaching a jamming transition, which provides insights that allow us to map the wealth of behavior map the wealth of behavior onto a phase diagram of jamming for wet granular media.

We adopt a recently developed "moving capacitor" dynamic network model to simulate fluid-fluid displacement at the pore level [44] (see Supplemental Material [49]). The model employs an analog of the pore network geometry, where resistors, batteries, and capacitors are responsible for viscous, out-of-plane, and in-plane Laplace pressure drops, respectively. The fluid-fluid interface is represented as a moving capacitor—when the interface advances, the Laplace pressure increases until it encounters a burst (equivalent to a Haines jump), touch (touches the nearest particle), or overlap event (coalesces with a neighboring interface) [35,36,43]. These events determine how the interface advances, enlisting one or more new particles when a node on the interface reaches its filling capacity and becomes unstable. This model reproduces both the displacement pattern and the injection pressure signal under a wide range of capillary numbers and substrate wettabilities [43,44,50].
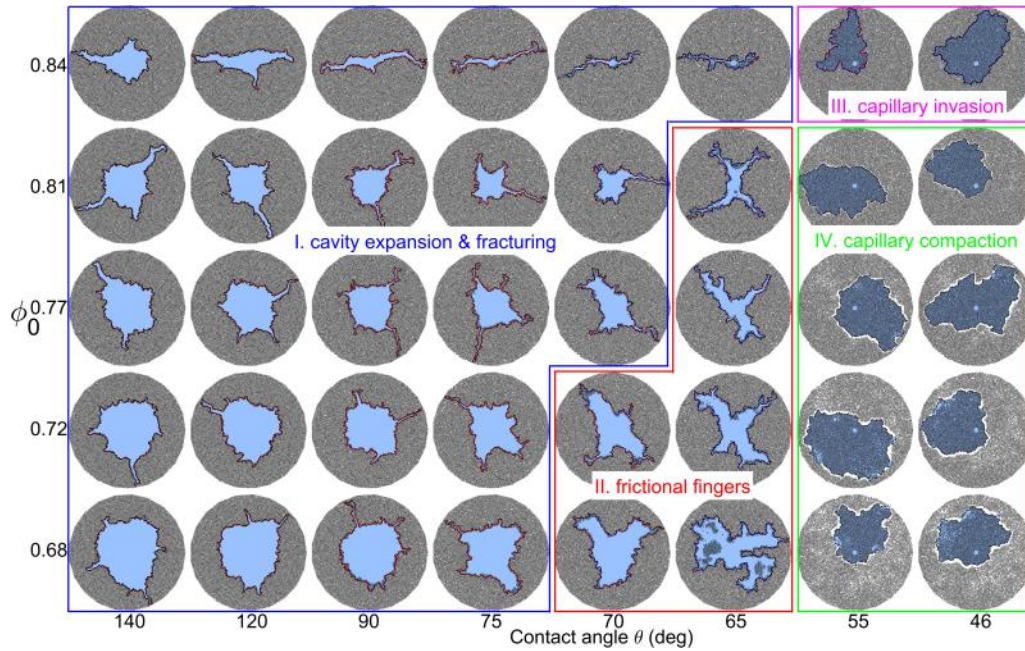
---

*juanes@mit.edu

FIG. 1. Visual phase diagram of the invading fluid morphology at breakthrough corresponding to different substrate wettabilities (contact angle θ) and initial packing densities ϕ_0. We identify four distinct morphological regimes: (I) cavity expansion and fracturing, (II) frictional fingers, (III) capillary invasion, and (IV) capillary compaction. See supplemental videos for the evolution of the morphology in each regime [49].

To capture particle motion, we couple the dynamic flow network model with a discrete element model (DEM), PFC2D® [49,51]. Hydromechanical two-way coupling is achieved from three perspectives: (1) The fluid pressures calculated from the moving-capacitor flow model exert forces on particles, and lead to particle rearrangement and deformation; (2) particle movements change the geometric configuration of the granular pack, which in turn changes the pore network topology and throat conductances and capillary entry pressures; and (3) expansion of the central cavity around the injection port "consumes" injected fluid, which decreases the flow of fluid permeating through the granular pack.

We simulate immiscible fluid-fluid displacement through a granular pack confined in a circular flow cell, by setting a constant injection rate at the center, and constant pressure at the perimeter. The invading and defending fluid viscosities are set to $\eta_{inv} = 8.9 \times 10^{-4}$ Pa s for water, and $\eta_{def} = 0.34$ Pa s for oil, respectively, and the interfacial tension is set to $\gamma = 13 \times 10^{-3}$ N/m. These parameters are chosen to mimic the experiments of Zhao *et al.* [41]. The granular pack has an outer and inner radius of $R_{out} = 13.25$ mm, $R_{in} = 0.5$ mm, and a height $h = 330$ μm. We adopt a simplified Hertz-Mindlin contact model [51] for particles in the granular pack, with the following properties: shear modulus $G = 50$ MPa, Poisson ratio $\nu = 0.5$ (quasi-incompressible, as in Ref. [52]), coefficient of friction $\mu = 0.3$ [22], density $\rho = 1040$ kg/m^3, and mean diameter $d = 300$ μm with 10% standard deviation (the same polydispersity as in Ref. [52]). We choose an injection rate $Q_{inj} = 4.3 \times 10^{-11}$ m^3/s, corresponding to a modified capillary number $Ca^* = \eta_{def}Q_{inj}R_{out}/(\gamma h d^2) = 0.5$ [22], for which viscous pressure gradients have time to relax between front movements, and capillary effects govern the displacement [53]. We conduct simulations in which we fix

these parameters, and we vary the contact angle θ from 140° (drainage) to 46° (imbibition), and the initial packing density ϕ_0 from 0.68 (loose pack) to 0.84 (dense pack).

In Fig. 1, we show the fluid invasion morphologies that result from injection in the form of a visual phase diagram for different values of θ and ϕ_0. The collection of patterns at breakthrough—when the invading fluid first reaches the outer boundary—exhibits four different regimes: (I) cavity expansion and fracturing, (II) frictional fingers, (III) capillary invasion, and (IV) capillary compaction.

To elucidate the conditions that lead to the emergence of each type of invasion pattern, we analyze the time evolution of the interface morphology and injection pressure for representative cases of each regime (see Fig. 3 of Supplemental Material and supplemental videos [49]).

Regime I: Cavity expansion and fracturing. When the injection pressure from fluid injection is sufficient to push particles outwards, the cavity keeps expanding until the energy input becomes insufficient to compact the granular pack further; the point at which fractures emerge [Supplemental Fig. 3(a) in Ref. [49]]. The wide range in P_{cap} at breakthrough ($t_d \to 1$) confirms the vulnerability of fracture tips compared with other throats along the cavity perimeter.

Regime II: Frictional fingers. At only weakly wetting conditions, the injection pressure is positive but smaller than in drainage. In this case, the injected fluid pushes away particles in certain directions, preferably those with loosely packed particles, and develops frictional fingers [Supplemental Fig. 3(b) in Ref. [49]].

Regime III: Capillary invasion. When particles have been densely packed initially, a small injection pressure (either positive or negative) is insufficient to overcome the established chains of contact forces, and thus particles do
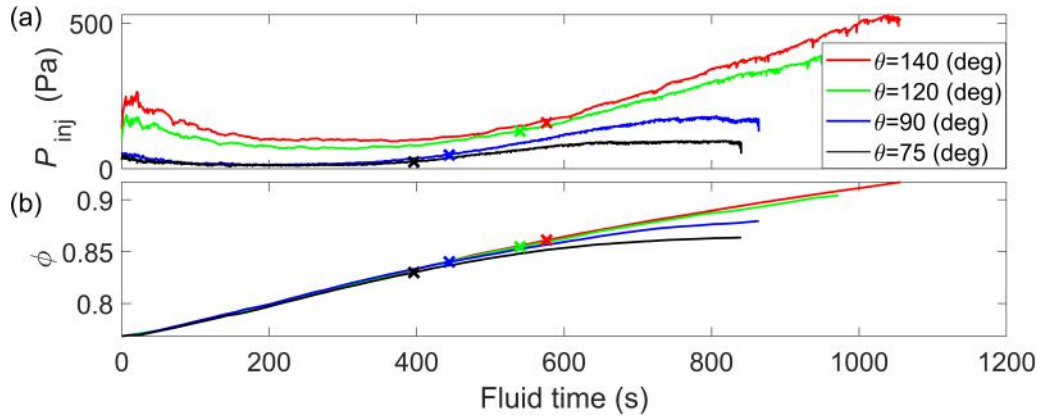
FIG. 2. Time evolution of (a) injection pressure P_{inj} and (b) packing density ϕ for simulations with initial packing density $\phi_0 = 0.77$, and $\theta = 75°, 90°, 120°, 140°$. The crosses denote the jamming transition for each case.

not move. In this case, we observe patterns of capillary fluid invasion in rigid media [Supplemental Fig. 3(c) in Ref. [49]]. The crossover from capillary invasion to capillary fracturing can be triggered, as we demonstrate here, by increasing θ to increase capillary forces.

Regime IV: Capillary compaction. In strong imbibition the injection pressure is negative, and for sufficiently loose granular packs, particles are dragged into the invading fluid under the out-of-plane curvature effect, leading to capillary compaction [Supplemental Fig. 3(d) in Ref. [49]].

The temporal signal of the injection pressure encodes information needed to understand the interplay between particle movement and fluid-fluid displacement. Since we restrict our study to the case when capillary forces dominate and viscous dissipation is negligible, the injection pressure signal is determined by the capillary entry pressure P_{cap}, which is a sum of in-plane and out-of-plane components. As a result, the injection pressure shows fluctuations in a stick-slip manner for all θ and ϕ_0, as has been documented in slow drainage experiments [53–55] and simulations [44]. As θ decreases, indicating that the substrate becomes more wetting to the invading fluid, the fluid-fluid displacement is controlled by cooperative pore-filling events (touch and overlap) with smaller P_{cap} compared with burst events [35,36,43,44]. This explains the general decreasing trend of injection pressure as θ decreases [Fig. 2(a)].

In a drainage displacement, instead of fluctuating around a mean value [44], the injection pressure exhibits a surprising convex shape as a function of time, first decreasing and then increasing with time. This is a signature of the fluid-solid coupling: The particles around the cavity are separated (opening up the throats and decreasing P_{cap}) during the initial stages of expansion, and then brought closer together (narrowing the throats and increasing P_{cap}), as the granular pack is being compacted during the late stages [Fig. 2(a)].

Figure 1 exhibits a surprising and heretofore unrecognized behavior of fluid injection into a granular pack: A decrease in θ—that is, transitioning from drainage to weak imbibition— leads to an earlier onset of fracturing, as evidenced by the smaller size of the fluid cavity at fluid breakthrough. This behavior cannot be explained by the evolving injection pressure level, or the evolving packing fraction outside the cavity, or

the volume of fluid injected alone. Indeed, the transition to fracturing for different wetting conditions occurs at different injection pressures [Fig. 2(a)], different packing fractions [Fig. 2(b)], and different times [Fig. 2(a), 2(b)].

This raises the question of how wettability impacts the onset of fracturing, and whether such dependence is amenable to prediction. To answer this question, we hypothesize that the emergence of fracturing is akin to a phase transition from liquidlike to solidlike behavior, and that therefore it can be understood as a *jamming transition*. Indeed, the jamming transition has proved instrumental in understanding mechanical integrity in a remarkably diverse range of systems [56]. Examples include colloidal suspensions [57], athermal systems such as foam and emulsions [58], and the glass transition in supercooled liquids [59,60]. The jamming transition also occurs in (dry) granular systems at a well-defined packing density ϕ_c when the conditions of mechanical stability are satisfied [61–65]. Here, we explore whether the concept of jamming can be used to quantitatively explain the emergence of fractures in *wet* granular systems and, specifically, whether the onset of fracturing in our system arises from a jamming transition.

The jamming transition in a dry granular system occurs at a threshold packing fraction ϕ_c when mechanical stability is achieved. For $\phi < \phi_c$, the network of contact forces is constantly evolving and changing topology through particle rearrangement. For $\phi > \phi_c$, in contrast, the force network locks in and its strength is enhanced through particle deformation [61,64]. Classic metrics that characterize the transition in frictionless systems are a discontinuous increase in the mean contact number Z, a rise in the mean isotropic stress P of the granular pack above its background value [61], or the emergence of a nonzero shear modulus [63].

We confirm that the behavior of our system responds in a manner consistent with a jamming transition. In particular, we compute at each stage of the granular pack deformation the Cauchy stress tensor for each particle in the system, $\sigma_{ij} = \frac{1}{V} \sum_{n_c} (x_i^c - x_i) F_j^c$, where n_c is the number of contacts for the particle. From the stress tensor we extract its isotropic component $P = \text{tr}(\sigma_{ij})$ and a measure of the shear stress, $\tau_{\max} = (\sigma_{\max} - \sigma_{\min})/2$, where $\sigma_{\max}$ and $\sigma_{\min}$ are the largest and smallest eigenvalues of σ_{ij}, respectively. We observe
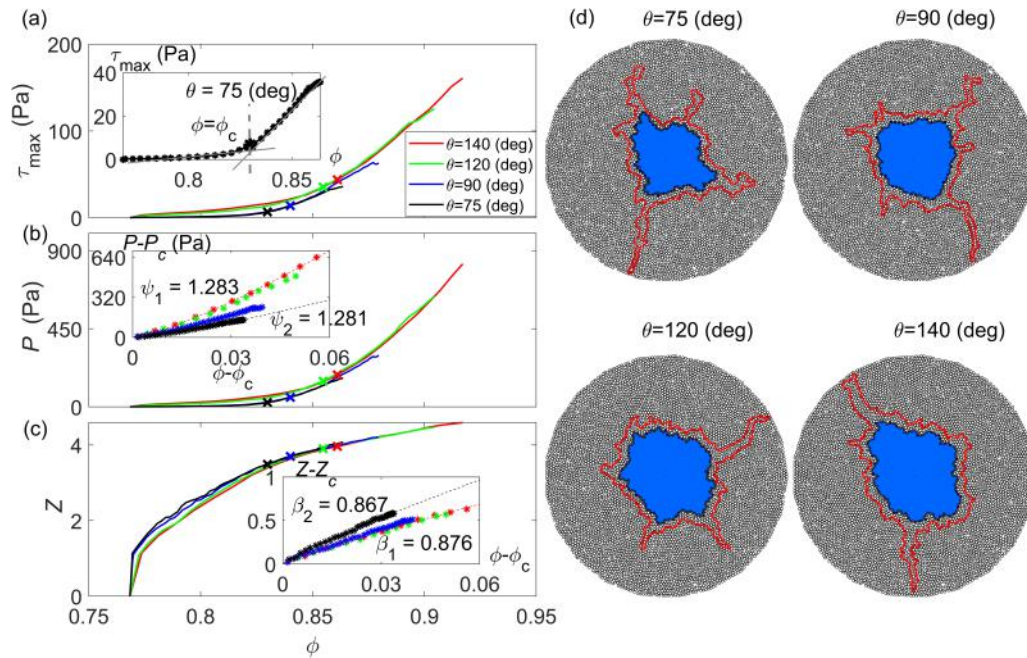
FIG. 3. Jamming transition analysis for $\phi_0 = 0.77$, $\theta = 75°, 90°, 120°, 140°$. (a)–(c) Average maximum shear stress ($\tau_{\max}$), mean particle stress (P), and mean contact number (Z) as a function of packing density ϕ in the compacting granular layer. (a) Inset: Determination of the critical packing fraction at jamming. (b), (c) Insets: $P - P_c$, $Z - Z_c$ as a function of $\phi - \phi_c$, exhibiting power-law trends. (d) Interface morphology at the jamming transition [identified from (a)] for $\theta = 75°, 90°, 120°, 140°$ (black line), compared with that at breakthrough (red line). The comparison confirms that the jamming transition determines the onset of fracturing.

that both quantities rise above a near-zero background as a function of the evolving mean packing fraction ϕ outside the central cavity [Fig. 3(a)].

We determine the jamming transition ϕ_c from the $\tau_{\max}$ profile as the intersection of two straight lines: one fitting the response of the background state, and one fitting a straight line to the asymptotic behavior in the highly compacted state [61,63] [Fig. 3(a), top inset]. For simulations with an initial packing density $\phi_0 = 0.77$, the jamming transition occurs at a critical packing density ϕ_c that takes increasing values (between 0.83 and 0.86) for increasing values of the contact angle (between $\theta = 75°$ and $140°$) [Fig. 3(a)]. This result is consistent with our hypothesis of the emergence of fracturing being controlled by a jamming transition, in which the transition occurs earlier (at a smaller ϕ_c) in imbibition than in drainage. Previous studies of jamming transition in both frictionless [64,66,67] and frictional [61] systems show a power-law increase of the mean stress with packing fraction above jamming, $P - P_c \sim (\phi - \phi_c)^\psi$, with an exponent slightly larger than 1, $\psi \approx 1.1$. Our simulations for a wet granular system also show a power-law increase, with the exponent ψ in the range 1.06–1.39, larger values corresponding to drainage displacements and loose granular packs, and smaller values corresponding to imbibition displacements and dense granular packs [Fig. 3(b), middle inset]. For our granular packings of finite $\mu = 0.3$, Z_c is expected to vary smoothly between $Z_c(\mu = 0) = 4$ and $Z_c(\mu \to \infty) \to 3$ [67,68]. Indeed, we find that Z_c lies in the range of 3.49–3.96, and exhibits a power-law dependence with packing fraction above jamming, $Z - Z_c \sim (\phi - \phi_c)^\beta$, $\beta \sim 0.87$ [Fig. 3(c), bottom inset]. Earlier studies have found exponents at jam-

ming in the vicinity of the jamming packing fraction and have shown that $\beta \sim 0.5$ [61,64,66,67,69]. Here, we study the behavior of granular packs beyond the jamming transition, and therefore we conduct a correction-to-scaling analysis [70,71]: $Z - Z_c = (\phi - \phi_c)^\beta (1 + a(\phi - \phi_c)^\omega + \cdots)$, with the leading correction-to-scaling exponent $\omega = 0.3$ [70], and the prefactor $a = 8.94$ in the order of $O(1)$, which validates the value of β obtained. The fact that fractures grow after the defined jamming transition ϕ_c (as evidenced by a visual comparison of the interface morphology at jamming and at breakthrough [Fig. 3(d)]) confirms our hypothesis that the onset of fractures emerges from a jamming transition.

A fundamental contribution to understanding jamming in (dry) granular systems was made in the form of a phase diagram that delineates the jammed state in the phase space of density, load, and temperature [72]. It shows that jamming can occur only at sufficiently high density, and that an increase in either load or temperature can unjam a system. We extend this description to wet granular systems by identifying quantities that determine the phase transition between jammed and unjammed states. We identify the packing fraction ϕ as the "density," and we posit that injection pressure P_{inj} plays the role of the "load" during injection. Thus, we represent any generic evolution of our system as a *trajectory* in $(P_{\text{inj}}^*, 1/\phi)$ space (Fig. 4), where P_{inj} is nondimensionalized by the characteristic capillary entry pressure in the system, γ/d.

Trajectories for regime I start with the prescribed ϕ_0 and move upwards in phase space as the granular pack is being compacted by the injected fluid. The injection pressure shows an initially decreasing and then increasing trend, as explained in Fig. 2(a). The transition from cavity expansion to fracturing
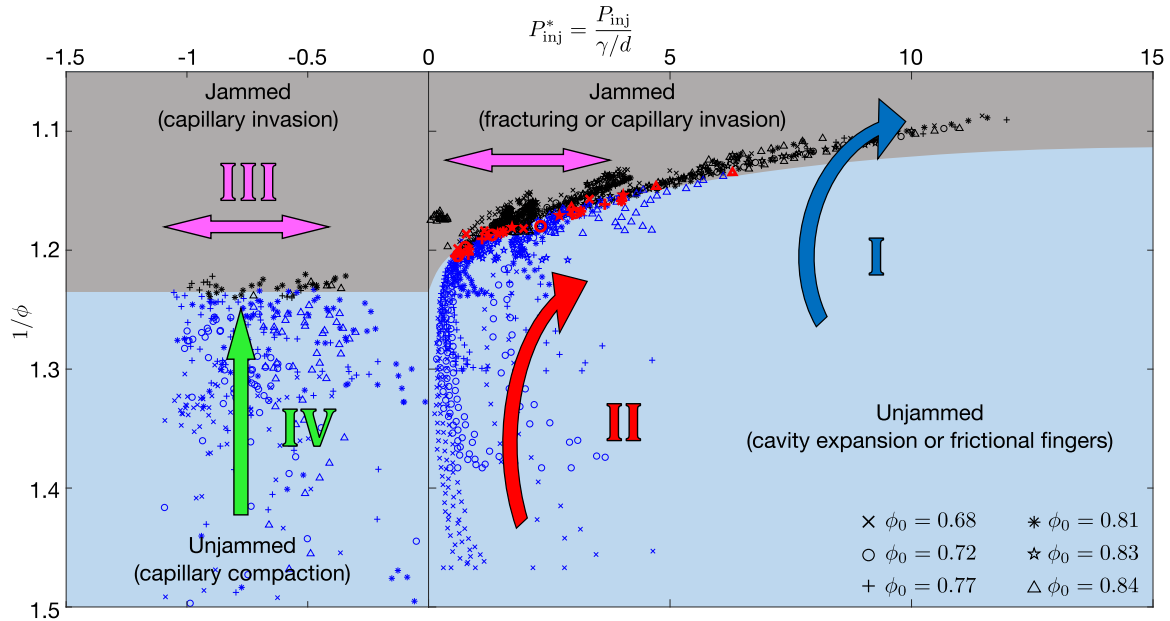
FIG. 4. Phase diagram of jamming for wet granular media when capillary forces dominate. Shown are the trajectories of the system in $(P_{\text{inj}}^*, 1/\phi)$ space for all the simulated cases of Fig. 1, ranging in contact angle θ from 140° (drainage) to 46° (imbibition), and ranging in initial packing density ϕ_0 from 0.68 (loose pack) to 0.84 (dense pack). Note the different scale of the horizontal axis for positive and negative injection pressures. For all four regimes of fluid invasion and grain deformation, the proposed diagram uniquely separates the system's unjammed state (blue) from its jammed state (gray), independently of θ and ϕ_0. In particular, this explains the onset of fracturing in capillary-dominated fluid-driven injection into granular packs (red symbols).

corresponds to a transition from the unjammed state to the jammed state. We collect transition points ϕ_c (shown as red markers in Fig. 4) for every simulation with a specific ϕ_0 and θ. These points collapse on a line in $(P_{\text{inj}}^*, 1/\phi)$ space, showing that under the same loading condition, the system jams at the same ϕ_c, independently of θ or ϕ_0. This transition line in the jamming phase diagram separates fundamentally different behaviors exhibited by our wet granular systems: fluidlike behavior (cavity expansion) in the unjammed state, and solidlike behavior (fracturing) in the jammed state (Fig. 4). This transition also helps explain the onset of fracturing: A larger energy input brought by the injection of a nonwetting fluid (larger value of the contact angle θ) compacts the system to a denser state before jamming occurs, which, in turn, delays the onset of fracturing.

We also show in Fig. 4 the trajectories for regimes II, III, and IV. Frictional fingers (regime II) have a positive injection pressure. The trajectories corresponding to this regime move upwards in ϕ as the system is being compacted, with stick-slip fluctuations in P_{inj}, but remain in the unjammed state for their entire evolution. Capillary invasion (regime III) occurs in an initially dense granular pack. The entire trajectory lies in the jammed state, with almost constant ϕ and stick-slip fluctuations in P_{inj}. Capillary compaction (regime IV) occurs when the out-of-plane capillary pressure dominates and the granular pack is relatively loose initially. We calculate ϕ for the region inside the fluid-fluid interface. Since the negative dragging pressure is comparable for all our simulations in this regime (-50 to -10 Pa), the granular pack is compacted inwards up to approximately the same packing density ($\phi \approx 0.83$) above the jamming transition. At zero external load ($P_{\text{inj}} = 0$), our

system jams at the random close packing fraction $\phi_c \approx \phi_{\text{rcp}} \approx$ 0.84 [73–75].

In summary, we have studied morphological transitions in granular packs as a result of capillary-dominated fluid-fluid displacement via a fully coupled model of two-phase flow and grain mechanics. Simulations of fluid injection into a granular pack with different initial packing densities and substrate wettabilities have led us to uncovering four invasion regimes: cavity expansion and fracturing, frictional fingers, capillary invasion, and capillary compaction. In particular, we have identified the emergence of fracture, and its surprising and unexplored dependence on the system's wettability. We have shown that the onset of fracture can be explained as a jamming transition, as confirmed by the behavior of the classic metrics of jamming such as the mean isotropic stress. We have synthesized the system's response in the form of a phase diagram of jamming for wet granular media, on which the jamming transition for all different trajectories collapse on a single line in $(P_{\text{inj}}^*, 1/\phi)$ space, independently of the initial packing density ϕ_0 and contact angle θ. Due to the irreversible nature of friction during collective particle motion, pumping fluid back after injection-induced deformation will lead to a granular configuration very different from the initial packing, which lies outside the scope of this study.

Our study paves the way for understanding the impact of other key variables of a wet granular system, such as properties of the solid particles (rigidity, friction coefficient, cementation) or the fluid (viscosity contrast, capillary number). By tailoring the range of values of these variables, our analysis may provide fundamental insight on specific applications,

from nanotechnology [76] to energy recovery [77], natural gas seeps [78,79], and geohazards [80,81].

[1] L. Cueto-Felgueroso and R. Juanes, Phys. Rev. Lett. **101**, 244504 (2008).

[2] M. L. Szulczewski, C. W. MacMinn, H. J. Herzog, and R. Juanes, Proc. Natl. Acad. Sci. USA **109**, 5185 (2012).

[3] J. W. Mercer and R. M. Cohen, J. Contam. Hydrol. **6**, 107 (1990).

[4] F. M. Orr and J. Taber, Science **224**, 563 (1984).

[5] R. Dangla, S. Lee, and C. N. Baroud, Phys. Rev. Lett. **107**, 124501 (2011).

[6] E. Brown and H. M. Jaeger, Rep. Prog. Phys. **77**, 046602 (2014).

[7] R. Jewel, A. Panaitescu, and A. Kudrolli, Phys. Rev. Fluids **3**, 084303 (2018).

[8] E. R. Dufresne, E. I. Corwin, N. A. Greenblatt, J. Ashmore, D. Y. Wang, A. D. Dinsmore, J. X. Cheng, X. S. Xie, J. W. Hutchinson, and D. A. Weitz, Phys. Rev. Lett. **91**, 224501 (2003).

[9] D. Vella, P. Aussillous, and L. Mahadevan, Europhys. Lett. **68**, 212 (2004).

[10] A. Jain and R. Juanes, J. Geophys. Res.: Solid Earth **114**, B08101 (2009).

[11] H. Shin and J. C. Santamarina, Earth Planet. Sci. Lett. **299**, 180 (2010).

[12] L. Goehring, W. J. Clegg, and A. F. Routh, Phys. Rev. Lett. **110**, 024301 (2013).

[13] C. Peco, W. Chen, Y. Liu, M. Bandi, J. E. Dolbow, and E. Fried, Soft Matter **13**, 5832 (2017).

[14] Z. Sun and J. C. Santamarina, J. Geophys. Res.: Solid Earth **124**, 2274 (2019).

[15] A. Groisman and E. Kaplan, Europhys. Lett. **25**, 415 (1994).

[16] H. Shin and J. C. Santamarina, Geotechnique **61**, 961 (2011).

[17] B. Sandnes, H. A. Knudsen, K. J. Måløy, and E. G. Flekkøy, Phys. Rev. Lett. **99**, 038001 (2007).

[18] X. Cheng, L. Xu, A. Patterson, H. M. Jaeger, and S. R. Nagel, Nat. Phys. **4**, 234 (2008).

[19] H. Huang, F. Zhang, P. Callahan, and J. Ayoub, Phys. Rev. Lett. **108**, 258001 (2012).

[20] F. Zhang, B. Damjanac, and H. Huang, J. Geophys. Res.: Solid Earth **118**, 2703 (2013).

[21] B. Sandnes, E. Flekkøy, H. Knudsen, K. Måløy, and H. See, Nat. Commun. **2**, 288 (2011).

[22] R. Holtzman, M. L. Szulczewski, and R. Juanes, Phys. Rev. Lett. **108**, 264504 (2012).

[23] F. K. Eriksen, R. Toussaint, K. J. Måløy, and E. G. Flekkøy, Front. Phys. **3**, 81 (2015).

[24] R. Holtzman and R. Juanes, Phys. Rev. E **82**, 046305 (2010).

[25] G. Varas, V. Vidal, and J.-C. Géminard, Phys. Rev. E **83**, 011302 (2011).

[26] G. Varas, V. Vidal, and J.-C. Géminard, Phys. Rev. E **83**, 061302 (2011).

[27] S. Lee, J. Lee, R. L. Mestre, F. Xu, and C. W. MacMinn, arXiv:1808.02921.

[28] B. P. Boudreau, C. Algar, B. D. Johnson, I. Croudace, A. Reed, Y. Furukawa, K. M. Dorgan, P. A. Jumars, A. S. Grader, and B. S. Gardiner, Geology **33**, 517 (2005).

[29] B. P. Scandella, L. Pillsbury, T. Weber, C. Ruppel, H. F. Hemond, and R. Juanes, Geophys. Res. Lett. **43**, 4374 (2016).

[30] B. P. Scandella, C. Varadharajan, H. F. Hemond, C. Ruppel, and R. Juanes, Geophys. Res. Lett. **38**, L06408 (2011).

[31] B. P. Scandella, K. Delwiche, H. F. Hemond, and R. Juanes, J. Geophys. Res.: Biogeosci. **122**, 1298 (2017).

[32] J. C. Melrose, Soc. Pet. Eng. J. **5**, 259 (1965).

[33] I. Fatt, W. A. Klikoff, Jr. *et al.*, J. Pet. Technol. **11**, 71 (1959).

[34] M. J. Blunt and H. Scher, Phys. Rev. E **52**, 6387 (1995).

[35] M. Cieplak and M. O. Robbins, Phys. Rev. Lett. **60**, 2042 (1988).

[36] M. Cieplak and M. O. Robbins, Phys. Rev. B **41**, 11508 (1990).

[37] M. J. Blunt, Curr. Opin. Colloid Interface Sci. **6**, 197 (2001).

[38] P. H. Valvatne and M. J. Blunt, Water Resour. Res. **40**, W07406 (2004).

[39] M. Trojer, M. L. Szulczewski, and R. Juanes, Phys. Rev. Applied **3**, 054008 (2015).

[40] R. Holtzman and E. Segre, Phys. Rev. Lett. **115**, 164501 (2015).

[41] B. Zhao, C. W. MacMinn, and R. Juanes, Proc. Natl. Acad. Sci. USA **113**, 10251 (2016).

[42] M. Jung, M. Brinkmann, R. Seemann, T. Hiller, M. Sanchez de La Lama, and S. Herminghaus, Phys. Rev. Fluids **1**, 074202 (2016).

[43] B. K. Primkulov, S. Talman, K. Khaleghi, A. Rangriz Shokri, R. Chalaturnyk, B. Zhao, C. W. MacMinn, and R. Juanes, Phys. Rev. Fluids **3**, 104001 (2018).

[44] B. K. Primkulov, A. A. Pahlavan, X. Fu, B. Zhao, C. W. MacMinn, and R. Juanes, J. Fluid Mech. **875**, R4 (2019).

[45] A. AlRatrout, M. J. Blunt, and B. Bijeljic, Proc. Natl. Acad. Sci. USA **115**, 8901 (2018).

[46] M. Rücker, W.-B. Bartels, K. Singh, N. Brussee, A. Coorn, H. van der Linde, A. Bonnin, H. Ott, S. Hassanizadeh, M. Blunt *et al.*, Geophys. Res. Lett. **46**, 3225 (2019).

[47] K. Singh, M. Jung, M. Brinkmann, and R. Seemann, Annu. Rev. Fluid Mech. **51**, 429 (2019).

[48] C. Chevalier, A. Lindner, M. Leroux, and E. Clément, J. Non-Newtonian Fluid Mech. **158**, 63 (2009).

[49] See Supplemental Material at http://link.aps.org/supplemental/10.1103/PhysRevResearch.2.022012 for implementation details of the fully-coupled model of two-phase flow and grain mechanics, evolution of interface morphology at each regime, and influence of grain properties on the jamming phase diagram.

[50] B. Zhao, C. W. MacMinn, B. K. Primkulov, Y. Chen, A. J. Valocchi, J. Zhao, Q. Kang, K. Bruning, J. E. McClure, C. T. Miller *et al.*, Proc. Natl. Acad. Sci. USA **116**, 13799 (2019).

[51] ITASCA, *PFC2D, v3.1 – Theory and Background* (Itasca Consulting Group, Inc., Minneapolis, MN, 2004).

[52] C. W. MacMinn, E. R. Dufresne, and J. S. Wettlaufer, Phys. Rev. X **5**, 011020 (2015).

[53] L. Furuberg, K. J. Måløy, and J. Feder, Phys. Rev. E **53**, 966 (1996).

[54] K. J. Måløy, L. Furuberg, J. Feder, and T. Jøssang, Phys. Rev. Lett. **68**, 2161 (1992).

[55] F. Moebius and D. Or, J. Colloid Interface Sci. **377**, 406 (2012).

[56] A. J. Liu and S. R. Nagel, *Jamming and Rheology: Constrained Dynamics on Microscopic and Macroscopic Scales* (CRC Press, Boca Raton, FL, 2001).

[57] M. E. Cates, J. P. Wittmer, J.-P. Bouchaud, and P. Claudin, Phys. Rev. Lett. **81**, 1841 (1998).

[58] I. K. Ono, C. S. O'Hern, D. J. Durian, S. A. Langer, A. J. Liu, and S. R. Nagel, Phys. Rev. Lett. **89**, 095703 (2002).

[59] D. L. Anderson, Science **267**, 1618 (1995).

[60] C. S. O'Hern, S. A. Langer, A. J. Liu, and S. R. Nagel, Phys. Rev. Lett. **86**, 111 (2001).

[61] T. S. Majmudar, M. Sperl, S. Luding, and R. P. Behringer, Phys. Rev. Lett. **98**, 058001 (2007).

[62] S. Henkes and B. Chakraborty, Phys. Rev. Lett. **95**, 198002 (2005).

[63] C. Heussinger and J.-L. Barrat, Phys. Rev. Lett. **102**, 218303 (2009).

[64] C. S. O'Hern, L. E. Silbert, A. J. Liu, and S. R. Nagel, Phys. Rev. E **68**, 011306 (2003).

[65] P. Chaudhuri, L. Berthier, and S. Sastry, Phys. Rev. Lett. **104**, 165701 (2010).

[66] C. S. O'Hern, S. A. Langer, A. J. Liu, and S. R. Nagel, Phys. Rev. Lett. **88**, 075507 (2002).

[67] L. E. Silbert, D. Ertaş, G. S. Grest, T. C. Halsey, and D. Levine, Phys. Rev. E **65**, 031304 (2002).

[68] C. Song, P. Wang, and H. A. Makse, Nature (London) **453**, 629 (2008).

[69] A. Donev, S. Torquato, and F. H. Stillinger, Phys. Rev. E **71**, 011105 (2005).

[70] S. H. E. Rahbari, J. Vollmer, and H. Park, Phys. Rev. E **98**, 052905 (2018).

[71] C. P. Goodrich, A. J. Liu, and J. P. Sethna, Proc. Natl. Acad. Sci. USA **113**, 9745 (2016).

[72] A. J. Liu and S. R. Nagel, Nature (London) **396**, 21 (1998).

[73] J. G. Berryman, Phys. Rev. A **27**, 1053 (1983).

[74] M. P. Ciamarra, R. Pastore, M. Nicodemi, and A. Coniglio, Phys. Rev. E **84**, 041308 (2011).

[75] N. Xu, J. Blawzdziewicz, and C. S. O'Hern, Phys. Rev. E **71**, 061306 (2005).

[76] N. Chakrapani, B. Wei, A. Carrillo, P. M. Ajayan, and R. S. Kane, Proc. Natl. Acad. Sci. USA **101**, 4009 (2004).

[77] E. Ghanbari and H. Dehghanpour, Fuel **163**, 282 (2016).

[78] A. Skarke, C. Ruppel, M. Kodis, D. Brothers, and E. Lobecker, Nat. Geosci. **7**, 657 (2014).

[79] A. Parmigiani, S. Faroughi, C. Huber, O. Bachmann, and Y. Su, Nature (London) **532**, 492 (2016).

[80] A. L. Handwerger, A. W. Rempel, R. M. Skarbek, J. J. Roering, and G. E. Hilley, Proc. Natl. Acad. Sci. USA **113**, 10281 (2016).

[81] J. Palmer, Nature (London) **548**, 384 (2017).

Check for updates

Crossover from viscous fingering to fracturing in cohesive wet granular media: a photoporomechanics study†

Yue Meng, ‡ Wei Li § and Ruben Juanes *

We study fluid-induced deformation and fracture of cohesive granular media, and apply photoporo-mechanics to uncover the underpinning grain-scale mechanics. We fabricate photoelastic spherical particles of diameter d = 2 mm, and make a monolayer granular pack with tunable intergranular cohesion in a circular Hele–Shaw cell that is initially filled with viscous silicone oil. We inject water into the oil-filled photoelastic granular pack, varying the injection flow rate, defending-fluid viscosity, and intergranular cohesion. We find two different modes of fluid invasion: viscous fingering, and fracturing with leak-off of the injection fluid. We directly visualize the evolving effective stress field through the particles' photoelastic response, and discover a hoop effective stress region behind the water invasion front, where we observe tensile force chains in the circumferential direction. Outside the invasion front, we observe compressive force chains aligning in the radial direction. We conceptualize the system's behavior by means of a two-phase poroelastic continuum model. The model captures granular pack dilation and compaction with the boundary delineated by the invasion front, which explains the observed distinct alignments of the force chains. Finally, we rationalize the crossover from viscous fingering to fracturing by comparing the competing forces behind the process: viscous force from fluid injection that drives fractures, and intergranular cohesion and friction that resist fractures.

1. Introduction

Multiphase flow through granular and porous materials exhibits complex behavior, the understanding of which is critical in many natural and industrial processes, and the design of climate-change mitigation strategies. Examples include infiltration of water into the vadose zone,[1] methane migration in lake sediments,[2] hillslope infiltration and erosion after forest fires,[3] growth and deformation of cells and tissues,[4] shale gas production,[5] and geological carbon dioxide storage.[6] This complexity is linked to the interplay between multiphase flow and granular mechanics, which controls the morphological patterns, evolution, and function of a wide range of systems.[7] In many granular-fluid systems, the strong coupling among viscous, capillary, and frictional forces leads to a wide range of patterns, including desiccation cracks,[8,9] labyrinth structures,[10] granular fingers,[11–13] corals, and stick-slip bubbles.[14] In the

context of interfacial flows, fracture patterns have been observed in loose systems—such as particle rafts as a result of surfactant spreading[15,16]—as well as dense systems—such as colloidal suspensions as a result of drying.[17,18]

While fracturing during gas invasion in fluid-saturated media has been studied extensively in experiments[12,15–22] and simulations,[13,23–30] the underlying grain-scale mechanisms behind the morphodynamics and rheologies exhibited by deformable granular media remain poorly understood. To tackle this challenge, Meng *et al.*[31] adopt a recently developed experimental technique, photoporomechanics,[32] to directly visualize the evolving effective stress field in a fluid-filled cohesionless granular medium during fluid-induced fracturing. The effective stress field exhibits a surprising and heretofore unrecognized phenomenon: behind the propagating fracture tips, an effective stress shadow, where the intergranular stress is low and the granular pack exhibits undrained behavior, emerges and evolves as fractures propagate.

Here we aim to extend our previous work[31] to cohesive granular media. The mechanical and fracture properties of cohesive granular media are of interest for many applications, including powder aggregation,[33,34] stimulation of hydrocarbon-bearing rock strata for oil and gas production,[35] preconditioning and cave inducement in mining,[36,37] and remediation of

Massachusetts Institute of Technology, 77 Massachusetts Avenue, Cambridge, MA, USA. E-mail: juanes@mit.edu

‡ Present address: Stanford University, Stanford, CA, USA.
§ Present address: Stony Brook University, Stony Brook, NY, USA.

contaminated soil.[38] Similar hydraulic fractures manifest naturally at the geological scale, such as magma transport through dikes[39–43] and crack propagation at glacier beds.[44,45] Following the early work on cemented aggregates,[46–48] Hemmerle *et al.*[49] created a well-defined cohesive granular medium with tunable elasticity by mixing glass beads with curable polymer. Due to the huge stiffness contrast between polymer bridges (kPa–MPa) and glass beads (GPa), the mechanical response of the material is dominated by the deformation of the bridges rather than the deformation of the beads.[50,51] There is limited experimental study on weakly sintered or cemented materials[52] with bonds that are of comparable stiffness with that of the grains.

In this paper, we study fracturing in cohesive wet granular media and extract the evolving effective stress field *via* photoporomechanics. By mixing photoelastic particles with curable polymer of the same stiffness, we create a well-defined cohesive granular medium with tunable tensile strength. We uncover two modes of water invasion under different injection flow rate, defending fluid viscosity, and tensile strength of the granular pack: viscous fingering, and fracturing with leak-off of the injection fluid. Behind the invasion front, the granular pack is dilated with tensile effective stress in the circumferential direction, while ahead of the invasion front the granular pack is compacted with compressive effective stress in the radial direction. We develop a two-phase poroelastic continuum model to explain the observed distinct force-chain alignments. Finally, we conclude that the competition of intergranular cohesion and friction against viscous force dictates the crossover from viscous fingering to fracturing regime.

2. Materials and methods

Following the fabrication process in ref. 32, we produce photoelastic spherical particles with diameter $d = 1.98$ mm (with 3.5% standard deviation) and bulk modulus $K_s = 1.6$ MPa. The fabrication process is similar to "squeeze casting" for metals, but for polyurethane in our case. The process produces soft polyurethane spheres with an amber color. To test their sliding frictional properties, we build a shear box apparatus as follows. We prepare a thin acrylic plate in the size of 6 cm × 6 cm × 1.6 mm and punch 11 × 11 holes with diameter 2 mm into it. We squeeze particles into the holes, making sure they are integrated into the plate and can not roll against it. The bottom surface for the sliding test is either made of glass or cured from polyurethane. We then put a confining weight on the top of the acrylic plate, which varies from 2 N to 8 N. We immerse particles in the silicone oil, attach the side surface of the acrylic plate to a spring scale, and drag the plate at a constant velocity 1 mm s^{-1}. The spring scale measures the frictional force occurring between the particles and the bottom surface. After dividing it by the confining weight, we obtain the friction coefficient. When particles are immersed in the silicone oil, the friction coefficient between particles is $\mu_p = 0.2 \pm 0.06$, and the friction coefficient between the particle and the glass plate is $\mu_w = 0.05 \pm 0.02$. To prepare a cohesive granular pack, we mix
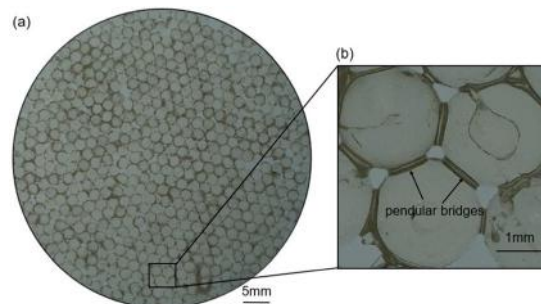

Fig. 1 (a) Cohesive photoelastic granular pack at a polymer content $C = 4.9\%$. (b) Close-up view of three particles connected by polymer bridges in the form of pendular rings.

a total mass M_g of cured photoelastic particles with a mass M_l of uncured, liquid-form polyurethane. We set $M_g = 9.2$ g to generate granular packs at a fixed initial two-dimensional packing density, 0.83, which is close to the random close packing density. We cast the solid–liquid mixture into a monolayer of granular pack inside a circular Hele–Shaw cell. The added polyurethane is imbibed directly into the granular pack and forms polymer bridges between particles that solidify once cured. Before the experiments, we peel the cured monolayer of particles out of the Hele–Shaw cell, eliminating bonds between particles and plates. We define the polymer content C as the mass of added polyurethane divided by the mass of particles, which determines the size of polymer bridges and thus the tensile strength of interparticle bonds. Fig. 1 shows a monolayer of cohesive photoelastic granular pack at a polymer content $C = 4.9\%$, above which pendular bridges begin to merge and form clusters.[49]

We inject water into a monolayer of cohesive photoelastic particles saturated with silicone oil in a circular Hele–Shaw cell (Fig. 2). To observe the photoelastic response of the particles,
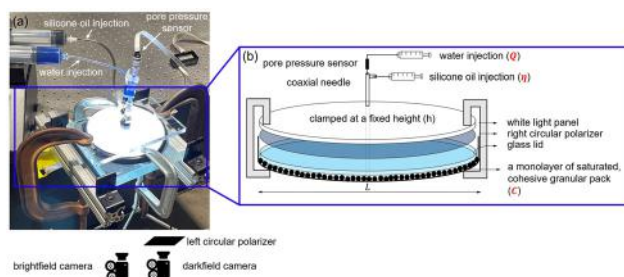

Fig. 2 Experimental setup to study fracturing in cohesive photoelastic granular media. (a) A monolayer of photoelastic particles (diameter d, polymer content C) is confined in a circular Hele−Shaw cell. The cell is uniformly clamped at a fixed height, h. Before the fracturing experiment, silicone oil (viscosity η) is slowly injected at the center of the cell with a coaxial needle to saturate the granular pack. After saturation, water is injected at a fixed flow rate Q with the injection pressure monitored by a pore-pressure sensor. A white-light panel, right and left circular polarizers form a darkfield circular polariscope. Brightfield and darkfield videos are captured by cameras placed underneath the cell. (b) Schematic of the circular Hele−Shaw cell (internal diameter L). A light panel, a polarizer, and a glass disk rest on top of the monolayer of photoelastic particles. The disk is slightly smaller than the cell to allow the fluids (but not particles) to leave the cell.

we construct a darkfield circular polariscope by a white light panel together with left and right circular polarizers.[53] We clamp the Hele–Shaw cell vertically at a fixed height h = 1.92 mm with four internal spacers to achieve plane-strain conditions throughout the experiments. As the height of internal spacers is smaller than the particle diameter, the top plate applies vertical confinement on the top of the particles. To allow the fluids (but not the particles) to leave the cell, the disk is made slightly smaller than the interior of the cell (inner diameter L = 10.6 cm), resulting in a thin gap around the edge of the cell. A coaxial needle is inserted at the center of the granular pack for saturation, fluid injection and pore pressure measurement. We adopt a dual-camera system to record brightfield (camera A) and darkfield (camera B) videos. As water is injected into the cohesive granular pack, viscous forces from fluid injection promote the development of fractures, while intergranular cohesion within the granular pack resists it. To study these competing forces during the fluid invasion process, we vary the injection flow rate Q from 5 mL min^{-1} to 220 mL min^{-1}, the silicone oil viscosity η from 30 kcSt, 100 kcSt, to 300 kcSt, and the polymer content C from 0% to 4.6% to stay in the pendular regime.

3. Representative experiments

In this section, we present two representative experiments with Q = 100 mL min^{-1}, η = 300 kcSt, C = 4.4% for viscous fingering, and C = 1.2% for fracturing with leak-off. For the dye color of the injected water, we need one that both visualizes the water invasion front in brightfield images and does not interfere with the photoelastic response in darkfield images. As a result, we dye the defending oil in black, and the invading water in light blue. By tracking the region in light blue color, we could easily identify the invading phase from brightfield images. To

confirm this, we refer to the ESI† videos on the fluid morphology and the effective stress evolution for the two experiments.[54]

We differentiate between viscous fingering and fracturing with leak-off regimes from the brightfield images. When water invades into the granular pack in viscous fingering patterns without noticeable relative motion between particles, the experiment is classified as viscous fingering (Fig. 3). When the injected water creates open channels with ensuing invasion into the pores, then the experiment is classified as fracturing with leak-off (Fig. 4). The darkfield images in Fig. 4 also confirm the formation of fractures where intergranular bonds exhibit strong photoelastic response and are torn apart under tension.

3.1 Viscous fingering

In Fig. 3, we show a sequence of snapshots for the viscous fingering experiment. We analyze the time evolution of the water–oil interface morphology from brightfield images, and the interparticle stresses of the granular pack from darkfield images. When particles have been strongly cemented initially, the injection pressure is insufficient to overcome the tensile strength of the intergranular bonds. In this regime, we observe patterns of viscous fingers without any significant relative motion between particles (Fig. 3(a)), and the intergranular bonds at finger tips endure tension without breakage (Fig. 3(b)).

3.2 Fracturing with leak-off

In Fig. 4, we show a sequence of snapshots for the fracturing experiment. The time evolution of the injection pressure P_{inj} is plotted in Fig. 5(a), which also indicates the times of the snapshots in Fig. 4. When particles have been densely packed initially, water firstly invades into the cohesive granular pack by expanding a small cavity around the injection port, with P_{inj} ramping up during this period. The pressure keeps building up
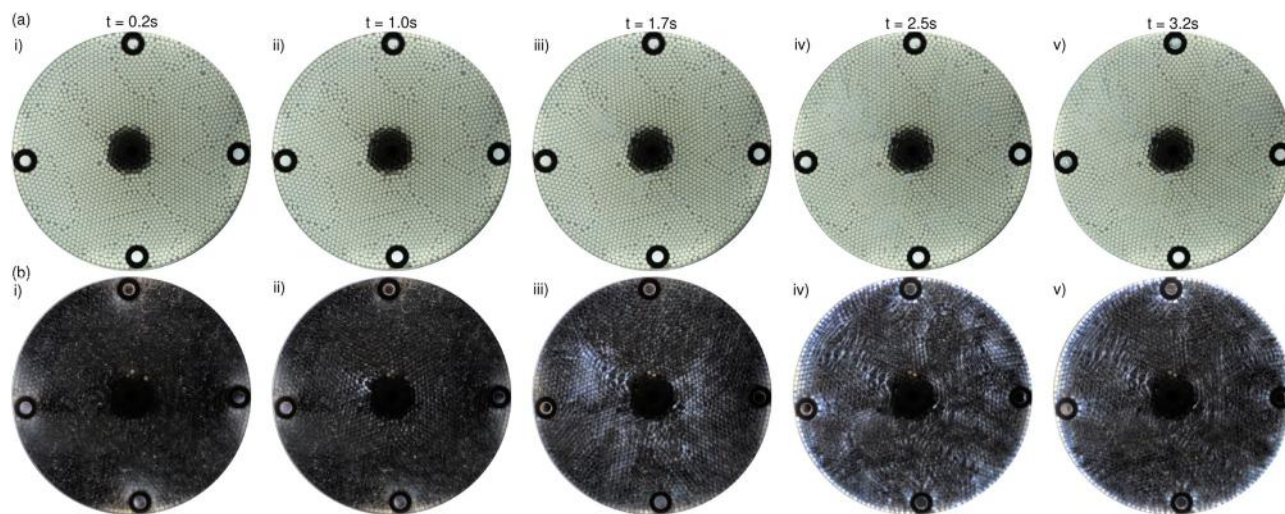

Fig. 3 For the viscous fingering experiment with Q = 100 mL min^{-1}, η = 300 kcSt and C = 4.4%, a sequence of snapshots shows the time evolution of (a) interface morphology from brightfield images, and (b) effective stress field from darkfield images. See ESI,† Video S1 for the evolution of the morphology and effective stress field in this regime.

Fig. 4 For the fracturing experiment with Q = 100 mL min^{-1}, η = 300 kcSt and C = 1.2%, a sequence of snapshots shows the time evolution of (a) interface morphology from brightfield images, and (b) effective stress field from darkfield images. See ESI,† Video S2 for the evolution of the morphology and effective stress field in this regime.
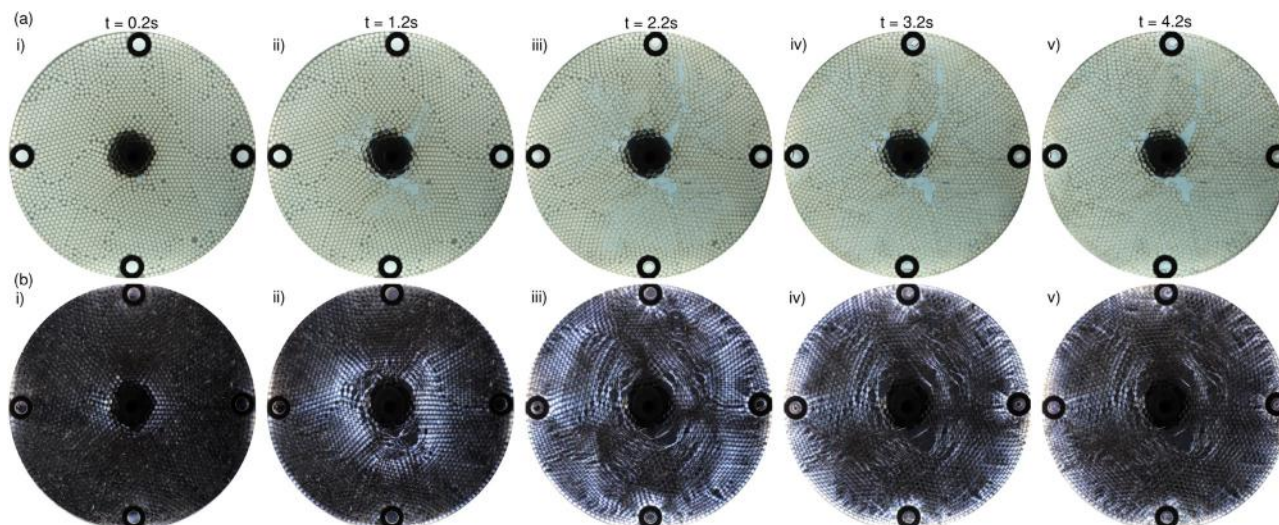
until it becomes sufficient to overcome the tensile strength of the interparticle bonds; the point at which fractures emerge (in between Fig. 4(i)–(ii)). As injection continues, much of the injected water leaks off into the permeable granular media as the fractures propagate (Fig. 4(ii)–(v)). In this period of fracturing with leak-off, P_{inj} slightly drops from its peak value and reaches a plateau afterwards (Fig. 5(a)). In this regime, the effective stress field exhibits a surprising phenomenon: behind the water invasion front, a hoop effective stress region, where we observe tensile force chains in the circumferential direction, emerges and evolves as invasion front propagates. Ahead of the invasion front, we observe compressive effective stress in the radial direction (Fig. 4(b)). The phenomena regarding the effective stress (*e.g.* tensile hoop stress near the injection port) has been predicted by continuum theories, such as cavity expansion models for single-phase flow,[55,56] and tip asymptotics in fracture mechanics (Sections 2 and 3 in ref. 57). However, there is a lack of understanding of the effective stress

evolution in a two-phase immiscible flow system, and our experiments visualize it for the first time.

4. Two-phase poroelastic continuum model

We model the immiscible injection of water into a cohesive granular pack saturated with silicone oil. To rationalize the experimental findings in Section 3, we develop a two-phase poroelastic continuum model focusing on the fracturing with leak-off regime. The wetting phase is the defending oil, and the nonwetting phase is the invading water. Under the experimental conditions explored, the modified capillary number[20] Ca* $= \eta QL/(\gamma hd^2) \sim 10^6$, which indicates that viscous forces outweigh capillary forces so we can safely neglect capillary effects. In the following, we present the extension of Biot's theory[58] to two-phase flow.[59,60] In our model, we assume radial symmetry and small deformations.
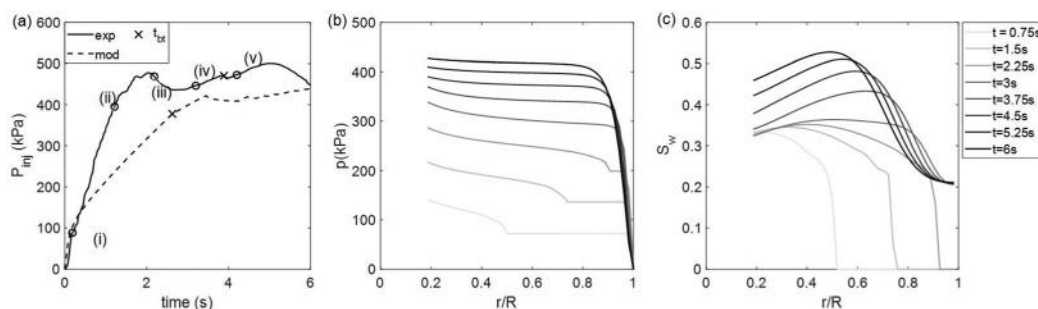

Fig. 5 Modeling results for the fracturing experiment with Q = 100 mL min^{-1}, η = 300 kcSt and C = 1.2%. (a) Time evolution of the injection pressure P_{inj}. The solid curve represents the experimental measurement, and the dashed curve represents the model prediction. The cross markers indicate water breakthrough through the cell edge. The circular markers indicate times for the snapshots shown in Fig. 4–8: t = 0.2 s, 1.2 s, 2.2 s, 3.2 s, 4.2 s in sequence. Modeling results of the time evolution of (b) pore pressure $p(r, t)$, and (c) water saturation $S_w(r, t)$. We show the solution at 8 times, linearly spaced from t = 0.75 s (light gray) to t = 6 s (black).

4.1 Fluid flow equations

For the two-phase immiscible flow system, the conservation of fluid mass can be written as follows:

$$\frac{\partial(\phi\rho_\alpha S_\alpha)}{\partial t} + \nabla \cdot (\rho_\alpha\phi S_\alpha v_a) = 0, \tag{1}$$

where ϕ is the porosity and ρ_α and S_α are the density and saturation of the fluid phase α (water w or oil o), respectively. The phase velocity v_a is related to the Darcy flux $\mathbf{q}_\alpha$ in a deforming medium by the following relation:

$$\mathbf{q}_\alpha = \phi S_\alpha(\mathbf{v}_\alpha - \mathbf{v}_s) = -\frac{k_0}{\eta_\alpha}k_{r\alpha}(\nabla p_\alpha - \rho_\alpha\mathbf{g}) \tag{2}$$

where $\mathbf{v}_s$ is the velocity of the solid skeleton, k_0 is the intrinsic permeability of the granular pack, $\mathbf{g}$ is the gravity vector, and η_α, $k_{r\alpha} = k_{r\alpha}(S_\alpha)$ and p_α are the dynamic viscosity, relative permeability, and fluid pressure for phase α, respectively. Since capillary pressure is negligible here, $p_c = p_w - p_o = 0$, the two phases have the same fluid pressure p. The relative permeability functions are given as Corey-type power law functions:[61]

$$k_{rw} = \left(\frac{S_w - S_{wc}}{1 - S_{wc}}\right)^{a_w}, \quad k_{ro} = \left(1 - \frac{S_w}{1 - S_{ro}}\right)^{a_o}, \tag{3}$$

where the fitting parameters are the critical water saturation for water to flow, $S_{wc} = 0.2$, the residual oil saturation, $S_{ro} = 0.2$, and the exponents $a_w = 2$ and $a_o = 5$.

Considering the mass conservation of the solid phase:

$$\frac{\partial[\rho_s(1-\phi)]}{\partial t} + \nabla \cdot [\rho_s(1-\phi)\mathbf{v_s}] = 0, \tag{4}$$

where ρ_s is the density of the solid constituents of the porous medium. Assuming isothermal conditions and using the equation of state for the solid, the following expression for the change in porosity is obtained:[62]

$$\frac{d\phi}{dt} = (b - \phi)\left(c_s\frac{dp}{dt} + \nabla \cdot \mathbf{v}_s\right) \tag{5}$$

where b is the Biot coefficient of the saturated porous medium, and c_s is the compressibility of the solid phase. We use eqn (2), (4), and (5) to expand eqn (1) as follows:

$$\phi\frac{\partial S_\alpha}{\partial t} + S_\alpha\left(b\frac{\partial\varepsilon_{kk}}{\partial t} + \frac{1}{M}\frac{\partial p}{\partial t}\right) + \nabla \cdot \mathbf{q}_\alpha = 0, \tag{6}$$

where ε_{kk} is the volumetric strain of the solid phase. The Biot modulus of the saturated granular pack, M, is related to fluid and rock properties as $\frac{1}{M} = \phi c_f + (b - \phi)c_s$.[63] Adding eqn (6) for water and oil phases, and imposing that $S_o + S_w \equiv 1$ for the saturated granular pack, we obtain the pressure diffusion equation:

$$b\frac{\partial\varepsilon_{kk}}{\partial t} + \frac{1}{M}\frac{\partial p}{\partial t} + \nabla \cdot \mathbf{q}_t = 0, \tag{7}$$

where $\mathbf{q}_t$ is the total Darcy flux for water and oil phases, $\mathbf{q}_t = \mathbf{q}_w + \mathbf{q}_o$.

4.2 Geomechanical equations

Under quasi-static conditions, the balance of linear momentum of the solid-fluid system states that:

$$\nabla\cdot\sigma + \rho_b\mathbf{g} = 0, \tag{8}$$

where σ is the Cauchy total stress tensor, and $\rho_b = (1 - \phi)\rho_s + \phi\sum_\alpha\rho_\alpha S_\alpha$, is the bulk density for the solid–fluid system. For axisymmetric deformation in plane-strain condition, the force balance equation becomes:

$$\frac{\partial\sigma_{rr}}{\partial r} + \frac{\sigma_{rr} - \sigma_{\theta\theta}}{r} = 0. \tag{9}$$

Following,[63] the poroelasticity equation states that

$$\sigma = \sigma' - bp\mathbb{I}, \tag{10}$$

where $\mathbb{I}$ represents the identity matrix. Terzaghi's effective stress tensor σ' is the portion of the stress supported through deformation of the solid skeleton, and where we adopt the convention of tension being positive. We adopt isotropic linear elastic theory for the granular pack; the constitutive equation for stress–strain is:

$$\sigma' = \frac{3K\nu}{1 + \nu}\varepsilon_{kk}\mathbb{I} + \frac{3K(1 - 2\nu)}{1 + \nu}\varepsilon, \tag{11}$$

where K, ν are the drained bulk modulus, and the drained Poisson ratio of the granular pack, respectively. The strain tensor is defined as $\varepsilon = \frac{1}{2}[\nabla\mathbf{u} + (\nabla\mathbf{u})^T]$, where $\mathbf{u}$ is the displacement vector. For the axisymmetric deformation in plane-strain condition, the strains are written as:

$$\varepsilon_{rr} = \frac{\partial u_r}{\partial r}, \quad \varepsilon_{\theta\theta} = \frac{u_r}{r}, \quad \varepsilon_{zz} = 0. \tag{12}$$

Using eqn (10), (11) and (12), the force balance eqn (9) can be expressed as a function of radial displacement $u_r(r,t)$ and pore pressure $p(r,t)$.

4.3 Summary of governing equations

The model has three governing equations, two derived from conservation of fluid mass [eqn (7) for the water–oil fluid mixture and eqn (6) for the water phase] and one derived from conservation of linear momentum (eqn (9)). The model solves the time evolution of three unknowns: (1) pore pressure field $p(r,t)$; (2) water saturation field $S_w(r,t)$; and (3) radial displacement field $u_r(r,t)$ of the cohesive granular pack, all of which are assumed to be radially symmetric. The governing equations are summarized and written in radial coordinates as follows:

$$b\frac{\partial\varepsilon_{kk}}{\partial t} + \frac{1}{M}\frac{\partial p}{\partial t} - k_0\frac{\partial}{\partial r}\left(\left(\frac{k_{rw}}{\eta_w} + \frac{k_{ro}}{\eta_o}\right)\frac{\partial p}{\partial r}\right) - \frac{k_0}{r}\left(\frac{k_{rw}}{\eta_w} + \frac{k_{ro}}{\eta_o}\right)\frac{\partial p}{\partial r} = 0, \tag{13}$$

$$\phi\frac{\partial S_w}{\partial t} + S_w\left(b\frac{\partial\varepsilon_{kk}}{\partial t} + \frac{1}{M}\frac{\partial p}{\partial t}\right) - \frac{k_0}{\eta_w}\frac{\partial}{\partial r}\left(k_{rw}\frac{\partial p}{\partial r}\right) - \frac{k_0}{r}\frac{k_{rw}}{\eta_w}\frac{\partial p}{\partial r} = 0, \tag{14}$$

$$\frac{\partial \sigma_{rr}}{\partial r} + \frac{\sigma_{rr} - \sigma_{\theta\theta}}{r} = 0. \qquad (15)$$

For the axisymmetric deformation in plane-strain condition, the stresses and strains are written in radial coordinates as:

$$\sigma_{rr} = \frac{3K\nu}{1+\nu}\varepsilon_{kk} + \frac{3K(1-2\nu)}{1+\nu}\varepsilon_{rr} - bp, \qquad (16)$$

$$\sigma_{\theta\theta} = \frac{3K\nu}{1+\nu}\varepsilon_{kk} + \frac{3K(1-2\nu)}{1+\nu}\varepsilon_{\theta\theta} - bp, \qquad (17)$$

$$\varepsilon_{rr} = \frac{\partial u_r}{\partial r}, \quad \varepsilon_{\theta\theta} = \frac{u_r}{r}, \quad \varepsilon_{zz} = 0, 3 \qquad (18)$$

$$\varepsilon_{kk} = \varepsilon_{rr} + \varepsilon_{\theta\theta} + \varepsilon_{zz}. \qquad (19)$$

We initialize the model by specifying $u_r(r, 0) = p(r, 0) = S_w(r, 0) = 0$. As for the boundary conditions, the inner boundary is free to move, subject to injection pressure as the total stress:

$$\sigma_{rr}(r_0, t) = -p(r_0, t) = -P_{inj}(t), \qquad (20)$$

where $r = r_0$ is the radius of the injection port, and $P_{inj}(t)$ is the injection pressure at time t. At the injection port, the total Darcy flux is the same as the Darcy flux of water. Since the injection system is composed of plastic syringe and tubing, we take the system compressibility into account for the inner flow boundary condition:

$$q_t(r_0, t) = q_w(r_0, t) = \frac{Q - c_{sys}V_{sys}\dfrac{\partial P_{inj}(t)}{\partial t}}{2\pi r_0 h}, \qquad (21)$$

where Q is the injection flow rate, and c_{sys} and V_{sys} are the compressibility and volume of the injection system, respectively. At the outer boundary $r = R$, the pressure is atmospheric, and particles have zero radial displacement:

$$p(R, t) = u_r(R, t) = 0. \qquad (22)$$

We now summarize the model in dimensionless form, denoting dimensionless quantities with a tilde. We adopt characteristic scales for length, time, stress/pressure, viscosity and permeability, non-dimensionalizing the governing equations via the scaling

$$\tilde{r} = \frac{r}{R}, \ \tilde{u}_r = \frac{u_r}{R}, \ \tilde{t} = \frac{t}{T_{pe}}, \ \tilde{p} = \frac{p}{M}, \ \tilde{\eta}_\alpha = \frac{\eta_\alpha}{\eta_o}, \ \tilde{k}_\alpha = \frac{k_0 k_{r\alpha}}{k_0},$$

$$\tilde{\sigma}_{rr} = \frac{\sigma_{rr}}{K}, \ \tilde{\sigma}_{\theta\theta} = \frac{\sigma_{\theta\theta}}{K}, \ \tilde{\sigma}'_{rr} = \frac{\sigma'_{rr}}{K}, \ \tilde{\sigma}'_{\theta\theta} = \frac{\sigma'_{\theta\theta}}{K} \qquad (23)$$

where $T_{pe} = \dfrac{\eta_o R^2}{k_0 M}$ is the characteristic poroelastic timescale. We can then rewrite eqn (13)–(15) in dimensionless form,

$$b\frac{\partial \varepsilon_{kk}}{\partial \tilde{t}} + \frac{\partial \tilde{p}}{\partial \tilde{t}} - \frac{\partial}{\partial \tilde{r}}\left(\left(\frac{k_{rw}}{\tilde{\eta}_w} + \frac{k_{ro}}{\tilde{\eta}_o}\right)\frac{\partial \tilde{p}}{\partial \tilde{r}}\right) - \frac{1}{\tilde{r}}\left(\frac{k_{rw}}{\tilde{\eta}_w} + \frac{k_{ro}}{\tilde{\eta}_o}\right)\frac{\partial \tilde{p}}{\partial \tilde{r}}$$
$$= 0, \qquad (24)$$

$$\phi\frac{\partial S_w}{\partial \tilde{t}} + S_w\left(b\frac{\partial \varepsilon_{kk}}{\partial \tilde{t}} + \frac{\partial \tilde{p}}{\partial \tilde{t}}\right) - \frac{1}{\tilde{\eta}_w}\frac{\partial}{\partial \tilde{r}}\left(k_{rw}\frac{\partial \tilde{p}}{\partial \tilde{r}}\right) - \frac{1}{\tilde{r}}\frac{k_{rw}}{\tilde{\eta}_w}\frac{\partial \tilde{p}}{\partial \tilde{r}}$$
$$= 0, \qquad (25)$$

$$\frac{\partial \tilde{\sigma}_{rr}}{\partial \tilde{r}} + \frac{\tilde{\sigma}_{rr} - \tilde{\sigma}_{\theta\theta}}{\tilde{r}} = 0. \qquad (26)$$

where the dimensionless stresses are written in radial coordinates as:

$$\tilde{\sigma}_{rr} = \frac{3\nu}{1+\nu}\varepsilon_{kk} + \frac{3(1-2\nu)}{1+\nu}\varepsilon_{rr} - \frac{bM}{K}\tilde{p}, \qquad (27)$$

$$\tilde{\sigma}_{\theta\theta} = \frac{3\nu}{1+\nu}\varepsilon_{kk} + \frac{3(1-2\nu)}{1+\nu}\varepsilon_{\theta\theta} - \frac{bM}{K}\tilde{p}. \qquad (28)$$

We initialize the model by specifying $\tilde{u}_r(\tilde{r}, 0) = \tilde{p}(\tilde{r}, 0) = S_w(\tilde{r}, 0) = 0$. The boundary conditions are as follows:

$$\tilde{\sigma}_{rr}(\tilde{r}_0, \tilde{t}) = -\frac{\tilde{P}_{inj}(\tilde{t})M}{K},$$

$$\tilde{q}_t(\tilde{r}_0, \tilde{t}) = \tilde{q}_w(\tilde{r}_0, \tilde{t}) = \frac{\tilde{Q}R}{\tilde{r}_0 h} - \frac{c_{sys}V_{sys}M}{2\pi r_0 kh}, \qquad (29)$$

$$\tilde{p}(1, \tilde{t}) = \tilde{u}_r(1, \tilde{t}) = 0$$

where $\tilde{P}_{inj}(t) = \dfrac{P_{inj}(t)}{M}$, $\tilde{Q} = \dfrac{\eta_o Q}{2\pi k_0 M R}$. Both of these quantities compare the viscous pressure due to injection with the Biot modulus of the granular pack.

4.4 Model parameters

The four poroelastic constants in the model are the drained bulk modulus K, the drained Poisson ratio ν, the Biot coefficient b, and the Biot modulus M of the granular pack. We obtained the drained and undrained bulk modulus K, K_u from a separate consolidation experiment.[32] We calculate the Biot coefficient from the relationship $b = 1 - \dfrac{K}{K_s}$,[63] and then obtain the Biot modulus via $M = \dfrac{K_u - K}{b^2}$.[64] To obtain the drained Poisson ratio of the granular pack, we build a discrete element model and conduct a biaxial test.[65] The permeability of the granular pack, k, is measured experimentally during the initial oil saturation process. A summary of the modeling parameters is given in Table 1.

Table 1 Modeling parameters for the two-phase poroelastic continuum model

Symbol	Value	Unit	Variable
r_0	4	mm	Injection port radius
R	5.3	cm	Hele–Shaw cell radius
d	2	mm	Diameter of the photoelastic particles
h	1.92	mm	Height of the Hele–Shaw cell
Q	100	mL min^{-1}	Water injection flow rate
c_{sys}	6×10^{-8}	Pa^{-1}	Injection system compressibility
V_{sys}	30	mL	Injection system volume
K	200	kPa	Drained bulk modulus of the pack
K_u	1.35	MPa	Undrained bulk modulus of the pack
ν	0.4		Drained Poisson ratio of the pack
b	0.88		Biot coefficient of the pack
M	1.49	MPa	Biot modulus of the pack
η_w	0.001	Pa s	Injecting water viscosity
η_o	291.3	Pa s	Defending silicone oil viscosity
ϕ	0.4		Porosity of the pack
k_0	10^{-10}	m^2	Intrinsic permeability of the pack

4.5 Numerical implementation

We use a finite volume numerical scheme to solve the three coupled governing equations (eqn (13)–(15)). We place the pressure and saturation unknowns $(p(r, t), S_w(r, t))$ at volume centers, and displacement unknowns $(u_r(r, t))$ at nodes. We partition the coupled problem and solve two sub-problems sequentially: the coupled flow and mechanics, and the transport of water saturation. We first fix the water saturation, and solve the coupled flow and mechanics equations (eqn (13) and (15)) simultaneously using implicit time discretization. Then we solve the water transport equation (eqn (14)) with prescribed pressure and displacement fields.

5. Results and discussion

5.1 Pore pressure and water saturation

We compare the experimental and modeling results of the time evolution of the injection pressure P_{inj} for the case with $Q = 100$ mL min^{-1}, $\eta = 300$ kcSt and $C = 1.2\%$ (Fig. 5(a)). By taking the injection system compressibility into account, the model captures the initial P_{inj} ramp-up measured in the experiment ($t = 0$–0.3 s). Before $t = 3.5$ s, P_{inj} keeps increasing, with the diffusion of pore pressure (Fig. 5(b)) and propagation of water invasion front (Fig. 5(c)). The transient pressure response comes from the compressibility of the granular pack, the timescale of which is $T \sim \dfrac{\eta' R^2}{k' M}$, where η' and k' are the effective viscosity and permeability of the pore fluid: a water-oil mixture. As the pore pressure diffuses to the cell boundary, P_{inj} approaches its steady state value, $P_{inj}^{ss} \sim \dfrac{\eta' Q R}{2\pi k' r_0 h}$.

The cross markers in Fig. 5(a) represent the moment when water reaches the cell boundary for the experiment and the model. The breakthrough predicted by the model is faster than that of the experiment by around 1.2 s. The observation that the water invasion front propagates faster in the model hints at an overestimation of the Biot modulus M; in other words, the model underestimates the granular pack compressibility/storativity. It reveals two underlying model limitations: (1) the storativity in the model, $S = \dfrac{1}{M}$, is assumed to be a constant without spatiotemporal variations, which in the experiment increases with porosity in the region where the granular pack dilates; and (2) by assuming linear elastic granular packs with small deformations, the model cannot capture the significant increase in storativity arising from the opening of fracture, where the porosity of the granular pack locally increases to 1.

Solving the water transport equation (eqn (14)), we obtain the time evolution of the water saturation field (Fig. 5(c)). The water invasion front propagates with the injection until its breakthrough at $t = 2.6$ s. After breakthrough, the radial profile of water saturation is nonmonotonic, exhibiting an increase of S_w with r and then a decrease. The position of the local maximum of the saturation profile moves towards the center of the cell as time evolves, and the value of the maximum saturation increases with time. This unusual behavior of water saturation contrasts that of fluid–fluid displacement in a rigid porous medium[66,67] and highlights the strong coupling between fluid flow and medium deformation in our system.

5.2 Displacement and volumetric strain

To probe into the granular mechanics behind the fracturing experiment in Fig. 4, we first measure the internal deformation of the pack *via* particle tracking, which provides a direct measure of the displacement field. We define a rectangular coordinate system centered at the injection port, where (x_i, y_i) is the position of particle i at time t and (X_i, Y_i) is its initial position. The displacement of particle i is then $\mathbf{u_i} = (x_i - X_i, y_i - Y_i)$, with magnitude $u_i(t) = \sqrt{(x_i - X_i)^2 + (y_i - Y_i)^2}$ and radial component $u_{r,i}(t) = \sqrt{x_i^2 + y_i^2} - \sqrt{X_i^2 + Y_i^2}$. The deformation is primarily radial because of the axisymmetric boundary conditions, so we focus on u_r.

Fig. 6 shows a sequence of snapshots of the experimental radial displacement field, corresponding to $t = 0.2$ s, 1.2 s, 2.2 s, 3.2 s, 4.2 s sequentially. We find that the radial displacement is large near the injection port and fades to zero at the rigid outer edge, with a petal-like mesoscale structure as reported by MacMinn et al.[68] and Zhang and Huang[69] (Fig. 6(a)). The radial displacements of particles are plotted as black dots in Fig. 6(b), and the red dashed line is the prediction from the continuum model. As P_{inj} increases from snapshots (i) to (iii), particles move radially outwards. From snapshots (iii) to (v), P_{inj} reaches a plateau, and particles relax and recover part of the deformation. The model captures the general trends in particle displacement behavior, with the notable exception of the compaction front near $r \sim 0.5R$ between times (iii) and (iv). Between this time period, the experimental data shows that particles with $r < 0.5R$ are compacted to a similar extent, as evidenced by their similar u_r values, which we refer to as a compaction front. The model underestimates the displacements there due to our assumption of linear elastic behavior: it cannot capture the plasticity-induced compaction front brought by bond breakage and particle rearrangements. As a result, the model fails to capture the compaction front exhibited in the experiment, which we define as the plasticity-induced compaction front.

We use the particle positions to calculate a best-fit local strain field. At time t during the water injection, we compute the closest possible approximation to a local strain tensor ε in the neighborhood of any particle with a sampling radius $r_s = 3d$.[68,70] The local strain for the particle is determined by minimizing the mean-square difference D^2 between the actual displacements of the neighboring particles relative to the central one and the relative displacements that they would have if they were in a region of uniform strain ε_{ij}. That is, we define

$$
\begin{aligned}
D^2(t) = &\sum_n \left(x_n - x_0 - (1 + \varepsilon_{11})(X_n - X_0) - \varepsilon_{12}(Y_n - Y_0) \right)^2 \\
&+ \left(y_n - y_0 - (1 + \varepsilon_{22})(Y_n - Y_0) - \varepsilon_{21}(X_n - X_0) \right)^2.
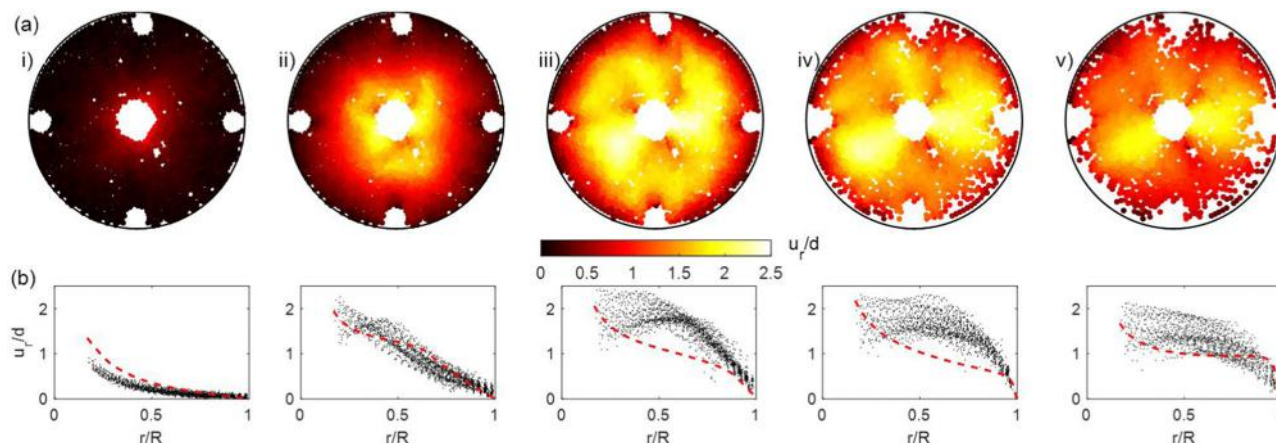\end{aligned}
$$

(30)

Fig. 6 For the fracturing experiment with Q = 100 mL min^{-1}, η = 300 kcSt and C = 1.2%, we analyze the sequence of snapshots shown in Fig. 4(i)–(v) corresponding to t = 0.2 s, 1.2 s, 2.2 s, 3.2 s, 4.2 s, respectively. The sequence of snapshots shows the time evolution of (a) experimental radial displacement field, and (b) radial displacement of the particles (black dots) compared with the continuum model prediction (dashed line).

where the index n runs over the particles within the sampling radius and n = 0 for the reference particle. We then compute ε for the reference particle at time t that minimizes $D^2(t)$. With this method, we obtain the local strain tensors for all particles in the granular pack.

We present a sequence of snapshots of the volumetric strain field in Fig. 7. The granular pack dilates (positive ε_{kk}) in the water-invaded region, and compacts (negative ε_{kk}) in the oil-saturated region (Fig. 7(a)). Such injection-induced dilation has also been reported for cohesionless granular packs and cohesive poroelastic cylinders.[55,68,71] Fig. 7(b) shows that the model captures the granular dilation and compaction, but cannot account for the plastic dilation near fractures brought by bond breakage and particle rearrangements.

The injection-induced deformation also feeds back to the fluid flow, as evidenced by the observed nonmonotonic water saturation curves (Fig. 5(c)). The granular pack dilation near the injection port increases the local porosity, and results in a

smaller value of S_w. As encoded in eqn (14), the coupling between fluid flow and medium deformation becomes strong when the deformation term is comparable to the flow term,

$$S_w b \frac{\partial \varepsilon_{kk}}{\partial t} \sim \nabla \cdot \mathbf{q}_w.$$

5.3 Effective stress

The photoelastic response offers a unique opportunity to gain additional understanding of the coupled pore-scale flow and particle mechanics during fluid-induced fracturing of the cohesive granular pack. To interpret the photoelastic response, we rely on the results of calibration experiments,[32] which have shown that, for the range of interparticle forces expected in our fracturing experiments, the relation between light intensity and force is monotonically increasing and approximately linear. From two-dimensional photoelasticity theory,[72] the stress-optic law states that in this "first-order" region, the photoelastic response is approximated to be linearly proportional to the
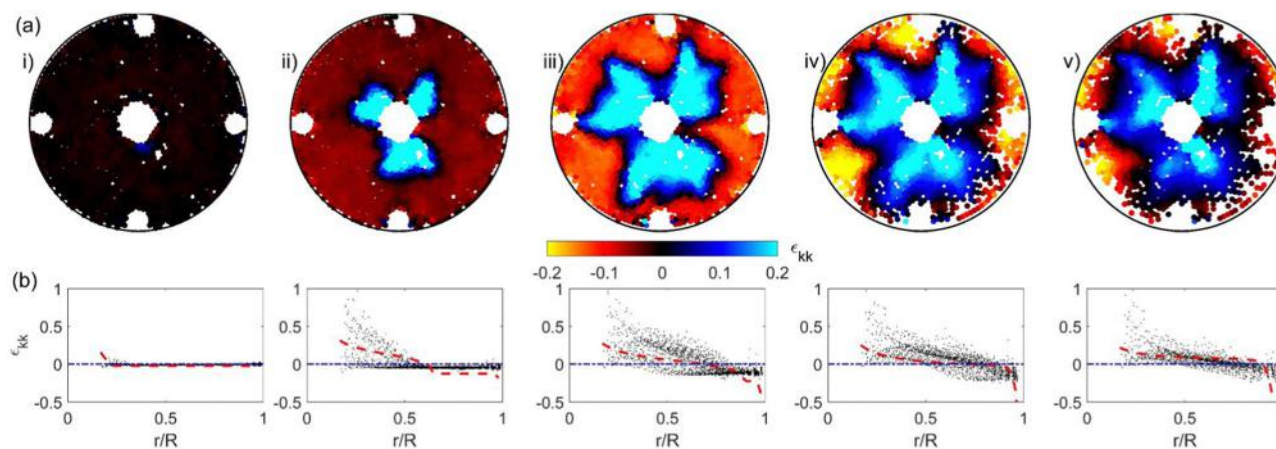

Fig. 7 For the fracturing experiment with Q = 100 mL min^{-1}, η = 300 kcSt and C = 1.2%, we analyze the sequence of snapshots shown in Fig. 4(i)–(v) corresponding to t = 0.2 s, 1.2 s, 2.2 s, 3.2 s, 4.2 s, respectively. The sequence of snapshots shows the time evolution of (a) experimental volumetric strain field, and (b) volumetric strain of the particles (black dots) compared with the continuum model prediction (dashed line).
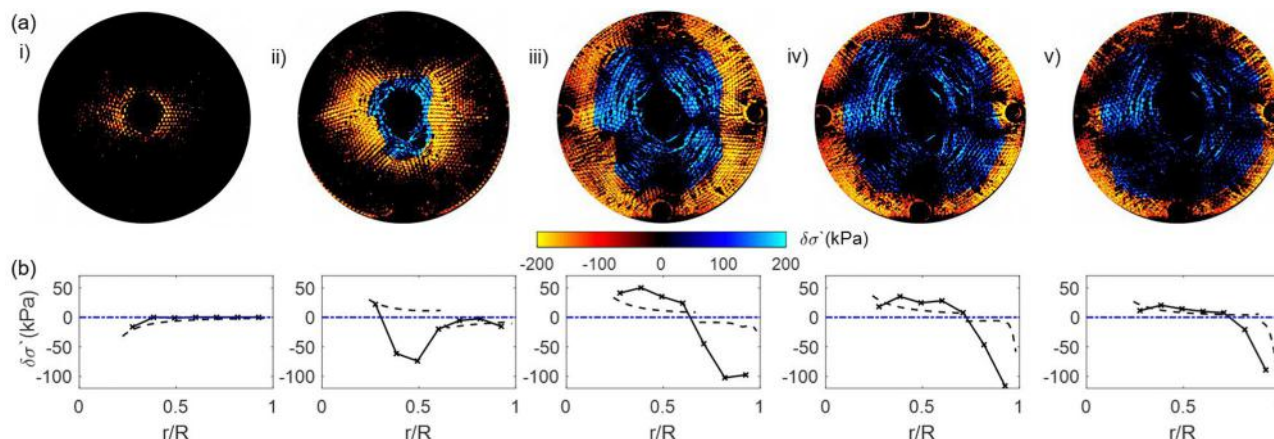
Fig. 8 For the fracturing experiment with Q = 100 mL min^{-1}, η = 300 kcSt and C = 1.2%, we analyze the sequence of snapshots shown in Fig. 4(i)–(v) corresponding to t = 0.2 s, 1.2 s, 2.2 s, 3.2 s, 4.2 s, respectively. The sequence of snapshots shows the time evolution of (a) experimental effective stress field, and (b) the radial distribution of the averaged effective stress (solid line) compared with the continuum model prediction (dashed line). To differentiate the direction of force chains, we set a sign convention manually to the principal effective stress difference $\delta\sigma'$, which should otherwise always be positive, as follows: $\delta\sigma'$ is positive for tensile force chains in circumferential/hoop direction, and negative for compressive force chains in radial direction.

principal effective stress difference with a constant coefficient: $I = F(\sigma'_1 - \sigma'_2)$, where σ'_1 and σ'_2 are the maximum and minimum principal effective stresses, respectively.

To quantify the photoelastic response into the principal effective stress difference, we conduct a separate calibration experiment to obtain the coefficient, F = 0.29 from the blue channel light intensity (see Appendix). To differentiate the direction of force chains, we set an *ad hoc* sign convention for the principal effective stress difference $\delta\sigma'$, which should otherwise always be positive, as follows: $\delta\sigma'$ is positive for tensile force chains in circumferential/hoop direction, and negative for compressive force chains in radial direction. After converting I into $\delta\sigma'$, and assigning its sign from the force chain direction, we present a sequence of snapshots of the effective stress field (Fig. 8(a)). Behind the water invasion front, a hoop effective stress region, where we observe tensile force

chains in the circumferential direction, emerges and evolves as the invasion front propagates. Ahead of the invasion front, we observe radial compaction of the granular pack.

In the model, we found that $\sigma'_t > \sigma'_r$ always holds, where σ'_t and σ'_r are the hoop and radial components of the effective stress, respectively. As the force chain direction aligns with the effective stress direction with larger absolute magnitude, we calculate $\delta\sigma'$ numerically with the aforementioned sign convention as follows:

$$\delta\sigma' = \begin{cases} \sigma'_t - \sigma'_r > 0, & \text{if } |\sigma'_t| > |\sigma'_r|, \\ \sigma'_r - \sigma'_t < 0, & \text{if } |\sigma'_r| > |\sigma'_t|. \end{cases} \tag{31}$$

We compare the experimental and numerical radial distribution of $\delta\sigma'$ in Fig. 8(b). The model captures the hoop effective stress region and radial compaction delineated by the invasion front. As mentioned in our previous discussion on the
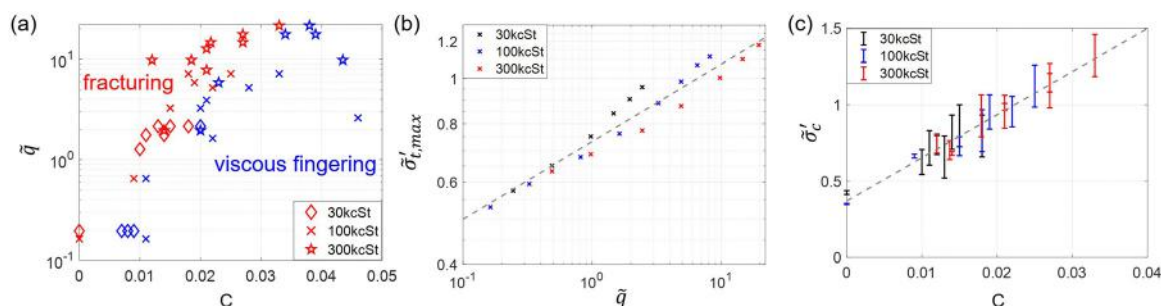

Fig. 9 Phase diagrams of fluid–fluid displacement patterns in the experiments. Diagram (a) shows the invasion patterns for all experiments, ranging in oil viscosity η from 30 kcSt, 100 kcSt, to 300 kcSt, water injection rate Q from 5 mL min^{-1} to 220 mL min^{-1}, and polymer content C from 0 to 4.6%. Diagram (b) shows the modeling prediction of the dimensionless maximum effective hoop stress at the injection port, $\tilde{\sigma}'_{t,\max} = \dfrac{\sigma'_{t,\max}}{K}$, as a function of the dimensionless flow rate, $\tilde{q} = \dfrac{\eta Q}{2\pi k_0 M R}$. The dashed line shows the fitted power law, $\tilde{\sigma}'_{t,\max} \approx 0.73\tilde{q}^{0.17}$. Diagram (c) shows the dimensionless tensile strength of the granular pack against fracturing, $\tilde{\sigma}'_c = \dfrac{P^{\text{frac}}_{\text{inj}}}{K}$, increases with polymer content C. The dashed line shows the fitted linear relationship, $\tilde{\sigma}'_c = 28.23C + 0.37$.

Paper

Soft Matter

displacement field, the model cannot capture the plasticity-induced compaction front, resulting in an underestimation of compressive effective stress between times (iii) and (iv).

5.4 Phase diagram of fluid invasion patterns in cohesive granular media

We observe two invasion patterns when varying the experimental parameters η, Q, and C: (I) pore invasion in the form of immiscible viscous fingering, and (II) fracturing with leak-off of the injection fluid. In a granular medium, fractures open when forces exerted by the fluids exceed the mechanical forces that resist particle rearrangements. Here the competing forces are the viscous force that drives fractures, and intergranular cohesion and friction that resist fractures. For a fixed domain geometry and granular medium (particle size and packing fraction), the viscous force is expected to increase with the product of the fluid viscosity η and the injection rate Q. We use a dimensionless flow rate $\tilde{q} = \dfrac{\eta Q}{2\pi k_0 M R}$ to characterize the viscous force. The resisting force is expected to have a friction-dependent component that will be constant across our experiments, and a cohesion-dependent component that will increase with the polymer content C. We use a dimensionless tensile strength $\tilde{\sigma}'_c = \dfrac{\sigma'_c}{K}$ to characterize the resisting force. Thus, we plot an empirical phase diagram of all our experiments, indicating whether they are either "fracturing" or "viscous fingering" (not fracturing) on the axes $\tilde{q}$ vs. C (Fig. 9(a)). This empirical plot shows a transition from viscous fingering at low ηQ and high C to fracturing at high ηQ and low C.

In the fracturing experiment (Section 3.2), the photoelastic response reveals that fractures initiate as tensile cracks near the injection port, where intergranular bonds break under tensile stress in the circumferential direction. Shear failure also occurs during fracture propagation, as evidenced by the classic slip line fracture pattern. To rationalize the crossover from viscous fingering to fracturing regimes quantitatively, we focus on the fracture initiation and assume the tensile failure mode. We adopt a fracturing criterion for cohesive granular media: the maximum hoop effective stress $\left(\sigma'_{t,\max}\right)$ should exceed the tensile strength between particles $\left(\sigma'_c\right)$ to break interparticle bonds and generate fractures. To theoretically predict $\sigma'_{t,\max}$, we run the model with different flow conditions, and obtain $\sigma'_{t,\max}$ at the injection port. We then obtain the dimensionless maximum hoop effective stress by $\tilde{\sigma}'_{t,\max} = \dfrac{\sigma'_{t,\max}}{K}$. Fig. 9(b) shows that $\tilde{\sigma}'_{t,\max}$ increases with $\tilde{q}$ approximately as a power law, $\tilde{\sigma}'_{t,\max} \approx 0.73\tilde{q}^{0.17}$.

To construct the relationship between $\tilde{\sigma}'_c$ and C, we record the injection pressure at the onset of fracturing when interparticle bonds break as $P^{\text{frac}}_{\text{inj}}$. We obtain the dimensionless tensile strength $\tilde{\sigma}'_c = \dfrac{P^{\text{frac}}_{\text{inj}}}{K}$, and find a linear relationship,
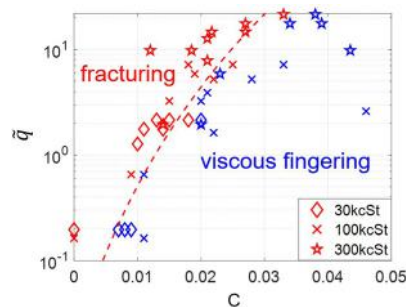

Fig. 10 Phase diagram of fluid–fluid displacement patterns in the experiments. The dashed line is the theoretical prediction on the crossover from viscous fingering to fracturing regime, $\tilde{q} = (38.67C + 0.51)^{6.0}$.

$\tilde{\sigma}'_c = 28.23C + 0.37$ (Fig. 9(c)). It does not pass through the origin because of the frictional resistance against fracturing for a cohesionless granular pack. After entering these relationships into the fracturing criterion, we obtain a condition involving $\tilde{q}$ and C for the transition into the fracturing regime, $\tilde{q} \geq (38.67C + 0.51)^{6.0}$. The theoretical prediction on the crossover from viscous fingering to fracturing regime agrees well with the experimental results (Fig. 10).

6. Conclusions

In summary, we have studied the morphology and rheology of injection-induced fracturing in cohesive wet granular packs *via* a recently developed experimental technique, photoporomechanics, which extends photoelasticity to granular systems with a fluid-filled connected pore space.[32] Experiments of water injection into cohesive photoelastic granular packs with different tensile strength, injection flow rate, and defending fluid viscosity have led us to uncover two invasion regimes: viscous fingering, and fracturing with leak-off of the injection fluid. Contrary to the observed effective stress shadow for cohesionless granular packs,[31] here we discover a hoop effective stress region behind the water invasion front. We developed a two-phase poroelastic continuum model that captures the transient pressure response arising from the granular pack compressibility. Behind the water invasion front, the granular pack is dilated with tensile force chains in the circumferential direction. Ahead of the water invasion front, the granular pack is compacted with compressive force chains in the radial direction. Finally, we rationalize the crossover from viscous fingering to fracturing across our suite of experiments by comparing the competing forces behind the process: viscous force from fluid injection that drives fractures, and intergranular cohesion and friction that resist fractures.

The developed two-phase continuum model assumes linear elasticity, which is insufficient to capture bond breakage and particle rearrangements. In spite of its limitations, our minimal-ingredients model still sheds insight and explains some of the key features observed in the experiments. The model reveals that the transient pressure response comes from the compressibility of the granular pack. It also captures granular pack dilation and compaction with the boundary

delineated by the invasion front, which explains the observed distinct alignments of the force chains. Furthermore, the model predicts the injection-induced hoop stress at the injection port where tensile cracks emerge, which is the key to rationalizing the crossover from viscous fingering to fracturing regimes quantitatively.

An interesting next step would be to account for these irreversible processes by means of a poroelastoplastic or poroviscoplastic model, possibly in large deformations to reflect the substantial variations in porosity during the fluid injection. Then the poroelastic constants could be taken to be porosity-dependent. One could start with extending previous work from Auton and MacMinn[56] to two-phase flow. To gain more insights on the fluid-induced fracturing, the radially symmetric model could be extended to a two-dimensional model that takes fracture morphology into account. Motivated by our experiments, Guevel *et al.*[73] develop a Darcy–Cahn–Hilliard model coupled with damage to describe multiphase-flow and fluid-driven fracturing in porous media. The model adopts a double phase-field approach, regularizing both cracks and fluid–fluid interfaces. The damage model allows for control over both nucleation and crack growth, and successfully recovers the flow regime transition from fingering to fracturing with leak-off observed in our experiments. Lastly, by adding capillarity in the fluid flow equations, the model would be able to explore a wider range in η and Q, and possibly explains more invasion regimes, such as capillary fingering and fracturing.

Our study paves the way for understanding the mechanical and fracture properties of cohesive porous materials that are of interest for applications in various fields of research and industry, such as rock mechanics,[46,74,75] the fracture of concrete and biomaterials,[76,77] and geoengineering.[78]

Conflicts of interest

There are no conflicts to declare.

Appendix: Calibration experiment for photoelastic response

The stress-optic law states that in the first order, the photoelastic response is approximated to be linearly proportional to the principal effective stress difference with a constant coefficient: $I = F\delta\sigma'$, where $\delta\sigma'$ is the principal effective stresses difference.[72] To obtain the coefficient F, we conduct a calibration experiment in the same Hele–Shaw cell where we conduct the fracturing experiments.

We prepare a monolayer of photoelastic particles at a polymer content $C = 3\%$. The particle diameter and initial packing density are the same as in the fracturing experiments. We saturate the granular pack with silicone oil of viscosity 5 cSt, which lubricates the particle–particle and particle-wall contacts. After saturation, we slowly inject water at $Q = 2$ mL min^{-1} into a sealed, elastic membrane that is connected to the injection port, and we monitor the injection pressure during injection. As injection proceeds, P_{inj} increases and drives the outward compaction of the granular pack quasi-statically. The membrane expands in size without any water leakage. We present a sequence of snapshots of the blue-channel light intensity field from darkfield images (Fig. 11(a)). The injection takes place under drained conditions, where the pressure in the defending fluid has time to fully dissipate, and the solid skeleton takes all the load from the water pressure at the inner boundary. The process is the same as a classical linear elastostatic example: a cylindrical vessel subject to an internal
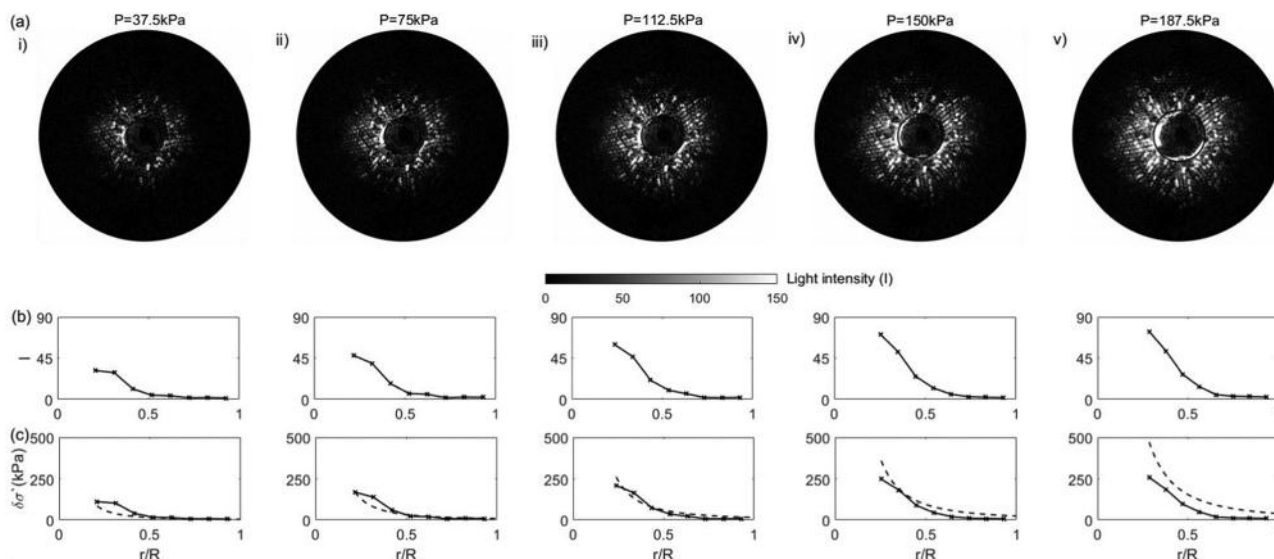

Fig. 11 For the calibration experiment with increasing water injection pressure, a sequence of snapshots shows the time evolution of (a) experimental light intensity field from the blue channel, (b) the radial distribution of the averaged light intensity $I(r, t)$, and (c) the radial distribution of the averaged effective stress difference (solid line) compared with the continuum model prediction (dashed line). The conversion factor between light intensity and effective stress difference is calibrated to be $F = \dfrac{I}{\delta\sigma'} = 0.29$.

pressure and fixed outer boundary.[79] For any specific P_{inj} and size of the inner boundary, we obtain the theoretical prediction on $\delta\sigma'$, which helps us to calibrate the conversion factor F between experimental light intensity (Fig. 11b)) and effective stress difference (Fig. 11(c)). The calibration shows that $F = 0.29$ under our experimental conditions.

Acknowledgements

Notes and references

1 D. E. Hill and J. Y. Parlange, *Soil Sci. Soc. Am. J.*, 1972, **36**, 697–702.
2 B. P. Scandella, L. Pillsbury, T. Weber, C. Ruppel, H. F. Hemond and R. Juanes, *Geophys. Res. Lett.*, 2016, **43**, 4374–4381.
3 J. Mataix-Solera, V. Arcenegui, N. Tessler, R. Zornoza, L. Wittenberg, C. Martnez, P. Caselles, A. Pérez-Bejarano, D. Malkinson and M. M. Jordán, *Catena*, 2013, **108**, 6–13.
4 G. T. Charras, J. C. Yarrow, M. A. Horton, L. Mahadevan and T. J. Mitchison, *Nature*, 2005, **435**, 365–369.
5 T. W. Patzek, F. Male and M. Marder, *Proc. Natl. Acad. Sci. U.S.A.*, 2013, **110**, 19731–19736.
6 M. L. Szulczewski, C. W. MacMinn, H. J. Herzog and R. Juanes, *Proc. Natl. Acad. Sci. U.S.A.*, 2012, **109**, 5185–5189.
7 R. Juanes, Y. Meng and B. K. Primkulov, *Phys. Rev. Fluids*, 2020, **5**, 110516.
8 A. Groisman and E. Kaplan, *Europhys. Lett.*, 1994, **25**, 415–420.
9 H. Shin and J. C. Santamarina, *Geotechnique*, 2011, **61**, 961–972.
10 B. Sandnes, H. Knudsen, K. J. Måløy and E. G. Flekkøy, *Phys. Rev. Lett.*, 2007, **99**, 038001.
11 X. Cheng, L. Xu, A. Patterson, H. M. Jaeger and S. R. Nagel, *Nat. Phys.*, 2008, **4**, 234.
12 H. Huang, F. Zhang, P. Callahan and J. Ayoub, *Phys. Rev. Lett.*, 2012, **108**, 258001.
13 F. Zhang, B. Damjanac and H. Huang, *J. Geophys. Res. Solid Earth*, 2013, **118**, 2703–2722.
14 B. Sandnes, E. Flekkøy, H. Knudsen, K. Måløy and H. See, *Nat. Commun.*, 2011, **2**, 288.
15 C. Peco, W. Chen, Y. Liu, M. M. Bandi, J. E. Dolbow and E. Fried, *Soft Matter*, 2017, **13**, 5832–5841.
16 D. Vella, P. Aussillous and L. Mahadevan, *Europhys. Lett.*, 2004, **68**, 212.
17 E. R. Dufresne, E. I. Corwin, N. A. Greenblatt, J. Ashmore, D. Y. Wang, A. D. Dinsmore, J. X. Cheng, X. S. Xie, J. W. Hutchinson and D. A. Weitz, *Phys. Rev. Lett.*, 2003, **91**, 224501.

18 L. Goehring, W. J. Clegg and A. F. Routh, *Phys. Rev. Lett.*, 2013, **110**, 024301.
19 H. Shin and J. C. Santamarina, *Earth Planet. Sci. Lett.*, 2010, **299**, 180–189.
20 R. Holtzman, M. L. Szulczewski and R. Juanes, *Phys. Rev. Lett.*, 2012, **108**, 264504.
21 J. M. Campbell, D. Ozturk and B. Sandnes, *Phys. Rev. Appl.*, 2017, **8**, 064029.
22 Z. Sun and J. C. Santamarina, *J. Geophys. Res. Solid Earth*, 2019, **124**, 2274–2285.
23 A. K. Jain and R. Juanes, *J. Geophys. Res. Solid Earth*, 2009, **114**, B08101.
24 R. Holtzman and R. Juanes, *Phys. Rev. E*, 2010, **82**, 046305.
25 B. Carrier and S. Granet, *Eng. Fract. Mech.*, 2012, **79**, 312–328.
26 B. Lecampion and J. Desroches, *J. Mech. Phys. Solids*, 2015, **82**, 235–258.
27 A. Mikelic, M. F. Wheeler and T. Wick, *Multiscale Model. Simul.*, 2015, **13**, 367–398.
28 D. Santillán, R. Juanes and L. Cueto-Felgueroso, *J. Geophys. Res. Solid Earth*, 2018, **123**, 2127–2155.
29 Y. Meng, B. K. Primkulov, Z. Yang, C. Y. Kwok and R. Juanes, *Phys. Rev. Res.*, 2020, **2**, 022012.
30 F. J. Carrillo and I. C. Bourg, *Phys. Rev. E*, 2021, **103**, 063106.
31 Y. Meng, W. Li and R. Juanes, *Phys. Rev. Appl.*, 2022, **18**, 064081.
32 W. Li, Y. Meng, B. K. Primkulov and R. Juanes, *Phys. Rev. Appl.*, 2021, **16**, 024043.
33 W. Pietsch, E. Hoffman and H. Rumpf, *Ind. Eng. Chem. Prod. Res. Dev.*, 1969, **8**, 58–62.
34 K. Kendall and C. Stainton, *Powder Technol.*, 2001, **121**, 223–229.
35 M. J. Economides, K. G. Nolte *et al.*, *Reservoir Stimulation*, Prentice Hall Englewood Cliffs, NJ, 1989, vol. 2.
36 A. van As and R. G. Jeffrey, Proceedings of the 5th North American Rock Mech. Symposium and the 17th Tunneling Association of Canada Conference (NARMSTAC conference), 2002, pp. 7–10.
37 R. G. Jeffrey, Z. Chen, K. W. Mills and S. Pegg, ISRM International Conference for Effective and Sustainable Hydraulic Fracturing, 2013.
38 L. C. Murdoch, *J. Geotech. Geoenviron. Eng.*, 2002, **128**, 488–495.
39 D. A. Spence, P. W. Sharp and D. L. Turcotte, *J. Fluid Mech.*, 1987, **174**, 135–153.
40 J. R. Lister and R. C. Kerr, *J. Geophys. Res. Solid Earth*, 1991, **96**, 10049–10077.
41 A. M. Rubin, *Annu. Rev. Earth Planet. Sci.*, 1995, **23**, 287–336.
42 S. M. Roper and J. R. Lister, *J. Fluid Mech.*, 2005, **536**, 79–98.
43 S. M. Roper and J. R. Lister, *J. Fluid Mech.*, 2007, **580**, 359–380.
44 V. C. Tsai and J. R. Rice, *J. Geophys. Res.*, 2010, **115**, F03007.
45 C. Y. Lai, J. Kingslake, M. G. Wearing, P. C. Chen, P. Gentine, H. Li, J. J. Spergel and J. M. van Wessem, *Nature*, 2020, **584**, 574–578.
46 J. Dvorkin, G. Mavko and A. Nur, *Mech. Mater.*, 1991, **12**, 207–217.

47 J. Dvorkin, A. Nur and H. Yin, *Mech. Mater.*, 1994, **18**, 351–366.

48 J. Dvorkin, J. Berryman and A. Nur, *Mech. Mater.*, 1999, **31**, 461–469.

49 A. Hemmerle, M. Schröter and L. Goehring, *Sci. Rep.*, 2016, **6**, 35650.

50 A. Schmeink, L. Goehring and A. Hemmerle, *Soft Matter*, 2017, **13**, 1040–1047.

51 A. Hemmerle, Y. Yamaguchi, M. Makowski, O. Bäumchen and L. Goehring, *Soft Matter*, 2021, **17**, 5806–5814.

52 R. Affes, J. Y. Delenne, Y. Monerie, F. Radjai and V. Topin, *Eur. Phys. J. E*, 2012, **35**, 117.

53 K. E. Daniels, J. E. Kollmer and J. G. Puckett, *Rev. Sci. Instrum.*, 2017, **88**, 051808.

54 See supplementary videos (ESI†).

55 L. C. Auton and C. W. MacMinn, *Proc. R. Soc. A: Math. Phys. Eng. Sci.*, 2018, **474**, 20180284.

56 L. C. Auton and C. W. MacMinn, *J. Mech. Phys. Solids*, 2019, **132**, 103690.

57 E. Detournay, *Annu. Rev. Fluid Mech.*, 2016, **48**, 311–339.

58 M. A. Biot, *J. Appl. Phys.*, 1941, **12**, 155–164.

59 B. Jha and R. Juanes, *Water Resour. Res.*, 2014, **50**, 3776–3808.

60 T. I. Bjørnarå, J. M. Nordbotten and J. Park, *Water Resour. Res.*, 2016, **52**, 1398–1417.

61 R. H. Brooks, *Hydraulic properties of porous media*, Colorado State University, 1965.

62 R. W. Lewis and B. A. Schrefler, *The finite element method in the static and dynamic deformation and consolidation of porous media*, John Wiley & Sons, 1998.

63 O. Coussy, *Mechanics of porous continua*, Wiley, 1995.

64 H. F. Wang, *Theory of linear poroelasticity with applications to geomechanics and hydrogeology*, Princeton University Press, 2000, vol. 2.

65 *ITASCA, PFC2D, v3.1-Theory and Background*, Itasca Consulting Group, Inc., Minneapolis, MN, 2004.

66 S. E. Buckley and M. C. Leverett, *Trans. AIME*, 1942, **146**, 107–116.

67 M. J. Blunt, *Multiphase flow in permeable media: A pore-scale perspective*, Cambridge University Press, 2017.

68 C. W. MacMinn, E. R. Dufresne and J. S. Wettlaufer, *Phys. Rev. X*, 2015, **5**, 011020.

69 F. Zhang and H. Huang, 45th US Rock Mechanics/Geomechanics Symposium, 2011.

70 M. L. Falk and J. S. Langer, *Phys. Rev. E*, 1998, **57**, 7192.

71 L. C. Auton and C. W. MacMinn, *Proc. R. Soc. A: Math. Phys. Eng. Sci.*, 2017, **473**, 20160753.

72 M. Frocht, *Photoelasticity*, John Wiley & Sons, 1941.

73 A. Guével, Y. Meng, C. Peco, R. Juanes and J. E. Dolbow, 2023, *arXiv*, preprint, arXiv:2306.16930, DOI: **10.48550/arXiv.2306.16930**.

74 J. C. Jaeger, N. G. W. Cook and R. Zimmerman, *Fundamentals of Rock Mechanics*, John Wiley & Sons, 2009.

75 R. Holtzman, *Int. J. Numer. Anal. Methods Geomech.*, 2012, **36**, 944–958.

76 O. Buyukozturk and B. Hearing, *Int. J. Solids Struct.*, 1998, **35**, 4055–4066.

77 V. Topin, F. Radjai, J. Y. Delenne, A. Sadoudi and F. Mabille, *J. Cereal Sci.*, 2008, **47**, 347–356.

78 D. L. Turcotte, E. M. Moores and J. B. Rundle, *Phys. Today*, 2014, **67**, 34.

79 L. Anand and S. Govindjee, *Continuum mechanics of solids*, Oxford University Press, 2020.

As a female Chinese student from engineering background, a complex set of personal experiences inform my vision for a more diverse, inclusive, and equitable academy. When I was an undergraduate student in civil and environmental engineering from the University of Hong Kong, I realized that there existed gender inequality in the department. There were only 20 female students among the 140 students in total, and two female professors among the 25 faculty members. My undergraduate research supervisor was one of the two female professors, who disclosed many challenges and dilemmas faced by female scientists to me: conflicts between family and career, and implicit gender bias and structural barriers in academia. I feel very fortunate and privileged to have been working with supportive and empathetic supervisors throughout my career - from an undergraduate/graduate student in civil and environmental engineering, to a postdoc in geoscience - all of whom encourage me to keep working hard for my dreams, with the belief that everyone deserves access to the academy and that we produce better science when that vision is realized.

As an international student, I also deeply understand the importance of an inclusive environment to ensure student's well-being. When the Umbrella Movement - a democracy protest in Hong Kong - emerged in 2014, I was a first-year undergraduate student from mainland China and got involved into the political conflicts inevitably. The professor in a course on critical thinking in contemporary society noticed the tension in the class, and scheduled group discussions for us to share different perspectives in an empathetic and constructive manner. From the experience, I have learned the importance of creating an inclusive community where everyone has a voice that is respected, and educators play a significant role during the process.

As a faculty member, I believe that opportunities for promoting diversity span the classroom, research group, department, and broader research community. I strive to adopt an inclusive and interdisciplinary approach in my classroom, such as developing introductory geophysics or engineering curricula that attract students from other departments. I will organize field trips so that students have a chance to be close to nature which develops their interests in geomechanics. For my research group, I'm happy to mentor female students and students of color. I will create an empathetic, supportive, and inclusive lab environment where everyone feels comfortable to reach out when encountering incidents violating diversity, equity and inclusion.

I work to put this knowledge forward through my own mentorship and outreach. I participated in a voluntary teaching program in 2015, when we gave physics lectures to high school students in a post-earthquake disaster zone. I have also been an academic mentor for an HKU female student since 2017, who is now a PhD student in geotechnical engineering. In the future, I would be interested in organizing workshops for underrepresented students to pursue their career in engineering or science. For instance, during my PhD, there was a civil and environmental engineering rising stars workshop in 2019, which brought together distinguished early-career women in academia. I believe my background and experience would help me contribute to the university's commitment to advancing diversity, equity, and inclusion.

Modern civil engineering draws on a variety of mathematical, experimental, computational, and engineering methods. Professors play an important role in guiding students synthesizing these approaches to solve real-life problems and interdisciplinary challenges. My educational experiences span departments of civil and environmental engineering, geoscience, mechanical engineering, computer science, and mathematics. I have mentored graduate students on the topic of geologic carbon sequestration from civil and environmental engineering background, and undergraduate students on discrete element modeling with geoscience background. I have also given lectures on multiphase flow in porous media in my current research group. My fundamental teaching philosophy in this field is molded by these experiences, emphasizing the development of students' instinctive understanding, reinforcing essential ideas through hands-on applications, and introducing students to interdisciplinary exploration.

Instinctive Understanding and Hands-on Applications: Developing physical intuition is crucial for guiding students beyond mere memorization of calculations and becoming more perceptive on experimental or modeling data. When I mentored a graduate student on conducting fluid injection test in a Hele-Shaw cell, I asked him to hypothesize a scaling law between the injection pressure and experimental parameters (injection flow rate, cell size, fluid viscosity, etc) for preliminary data interpretation. Through my studying experience, I have found that hands-on applications are crucial to consolidating key concepts in the discipline. Project-based assessments, such as modeling gravity-driven flow in porous media, conducting oedometer experiments, and numerical implementation on pressure diffusion equation, foster students' independent problem-solving skills and enrich the depth of their study.

Interdisciplinary Exploration: In a geomorphology class, I encountered a reading group assignment where I had to present a self-selected research paper in relevant fields. I presented a paper on the iceshelf hydrofracture in Antarctica that combined fracture mechanics, machine learning and remote sensing. Enlightening students with interdisciplinary research not only arouses their curiosity, but also connects them to a broader scientific community. Knowing the first-principles in the discipline, such as conservation of mass and momentum, students are well equipped to explore advanced numerical methods, including discrete element modeling, Lattice Boltzmann method, computational fluid dynamics, and phase-field modeling. Students can then connect the basic knowledge they are acquiring to a wide variety of application areas, scientific communities, and career paths. To reflect this philosophy, my courses will involve field trips, guest speakers in interdisciplinary fields, and reading group assignments.

Teaching Interests: With my diverse background in civil and environmental engineering and expertise in interdisciplinary research of geomechanics, fluid mechanics, and granular physics, I would be interested in teaching undergraduate or graduate level courses such as **Environmental Geotechnology, Environmental Fluid Mechanics, Soil Dynamics, etc.** I would also be interested in developing new graduate level courses emphasizing specialized areas of research, such as **Soft Matter Physics with Applications to Energy and Climate, and Theory of Poromechanics with Applications to Glaciology, Modeling Complex Physics with Graph Neural Network, and Granular Mechanics in Engineering.**